Dissertations, Theses, and Masters Projects   Theses, Dissertations, & Master Projects

Summer 2021

Evaluating Epoxy Cure And Adhesion Strength Through Single-Sided Nmr Measurements Of Molecular Mobility

Kayla Copeman
William & Mary - Arts & Sciences, kacopeman@email.wm.edu

Follow this and additional works at: https://scholarworks.wm.edu/etd

Part of the Chemistry Commons

Evaluating epoxy cure and adhesion strength through single-sided NMR measurements
of molecular mobility

Kayla Ann Copeman

Williamsburg, Virginia

B.S. Chemistry, University of Lynchburg, 2019

A Thesis presented to the Graduate Faculty of The College of William & Mary in
Candidacy for the Degree of
Master of Science

Department of Chemistry

College of William & Mary
May 2021

APPROVAL PAGE

This Thesis is submitted in partial fulfillment of
the requirements for the degree of

Master of Science

Kayla Copeman

Kayla Ann Copeman

Approved by the Committee April 2021

Committee Chair
Tyler K. Meldrum, Associate Professor, Chemistry
College of William & Mary

John C. Poutsma, Professor, Chemistry
College of William & Mary
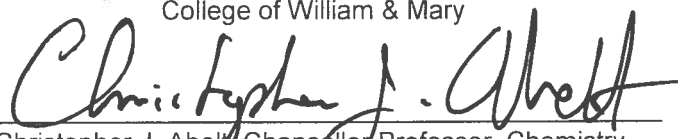
Christopher J. Abelt, Chancellor Professor, Chemistry
College of William & Mary

ABSTRACT

Commonly used in aerospace, automotive, marine, defense, electronic, and manufacturing industries, epoxy adhesives offer advantages over mechanical joints by providing stronger and/or more flexible bonds, more uniform stress distribution, low shrinkage, and lightweight connections between materials. Determination of curing kinetics and properties of interfaces between epoxy and inorganic substrates provides insight that is useful for quality control and defect detection for such applications. Single-sided NMR provides a nondestructive and inexpensive method for probing epoxy materials and spatially resolving the decay of spin-lattice and spin-spin relaxation times (T_1 and T_2) during and after curing of epoxy resins onto substrates. In this thesis, we report the use of single-sided NMR for both characterizing the strength of adhesion between epoxy and inorganic substrates and monitoring the cure of epoxy at various temperatures. Multi-dimensional $T_1 - T_2$ measurements were performed to correlate with changes in surface energies that provide insight on the chemical adhesion of various epoxy samples. Furthermore, we used NMR measurements to monitor *in-situ* room-temperature and heat curing of epoxy to probe reductions in molecular mobility throughout the curing process. NMR relaxation properties were correlated with DSC data for comparison of the cure extent and cure rates. Our results show the efficacy of single-sided NMR measurements for studying curing, the extent of cure, adhesion strength of epoxies, and interphase phenomena.

TABLE OF CONTENTS

ACKNOWLEDGEMENTS

This thesis is dedicated to my beloved Baba who passed away in the middle of completing my degree and never got to see this through. Your love and belief in me have made this journey possible.

LIST OF TABLES

LIST OF FIGURES

Chapter 1: Introduction

Developments throughout the manufacturing industry have created a demand for bonding materials with better properties in terms of strength, stiffness, durability, and flexibilty.[1] Adhesives offer alternatives to and advantages over mechanical joints including lower manufacturing costs, stress tolerance, higher structural integrity, and failure resistance.[2–4] Specifically in aerospace and defense engineering, epoxy resins have become an attractive asset for their use as composite matrixes.[5–7] Epoxy resins are lightweight materials[8] that have low shrinkage, strong adhesion to substrates, high chemical, thermal, and electrical resistance, moisture resistance, and overall toughness.[9–12] Depending on the type of resin, hardener, or filler used, epoxies can have varying degrees of flexibility, as well as conductivity and adherence.[13–15] Therefore, epoxy resins become multifunctional due to their versatile nature.

It is well understood that the physical properties of the cured epoxy resins rely on curing kinetics, molecular crosslinking structure, and curing temperature.[16–18] The molecular structure of the crosslinked epoxy resin determines the mobility of the polymer network which in turn determines properties like its stiffness or flexibility. However, curing conditions affect the overall crosslinking of the polymer chains, thus determining the final crosslinked structure. Therefore, measuring specific kinetic parameters of epoxies help to understand the network formation and final physical properties of the cured epoxy resin. Previous studies have used differential scanning calorimetry (DSC)[19,20] and Fourier transform infrared spectroscopy (FTIR)[21] for the kinetic analysis of epoxy curing.[22] DSC is useful for quantifying thermodynamic parameters relative to the formation of chemical bonds in curing epoxy systems.[23] Moreover, DSC measures the

heat flow from a reacting epoxy network allowing to characterize the extent of cure

(**Figure 1**).[24] FTIR, on the other hand, monitors the curing reaction based on the presence

of an epoxide functional group peak (~915 cm^{-1}).[25] The peak decreases after curing due

to the epoxide rings' opening and reacting with the curing agent, thus forming a

crosslinked network (**Figure 2**). Although both DSC and FTIR offer effective ways to

characterize epoxy cure, they cannot be used *in-situ*. Meanwhile DSC itself is otherwise

destructive to the sample. Overall, both DSC and FTIR are beneficial for monitoring

chemical changes in epoxy systems, however they fail to successfully monitor physical

changes that occur during and after cure.
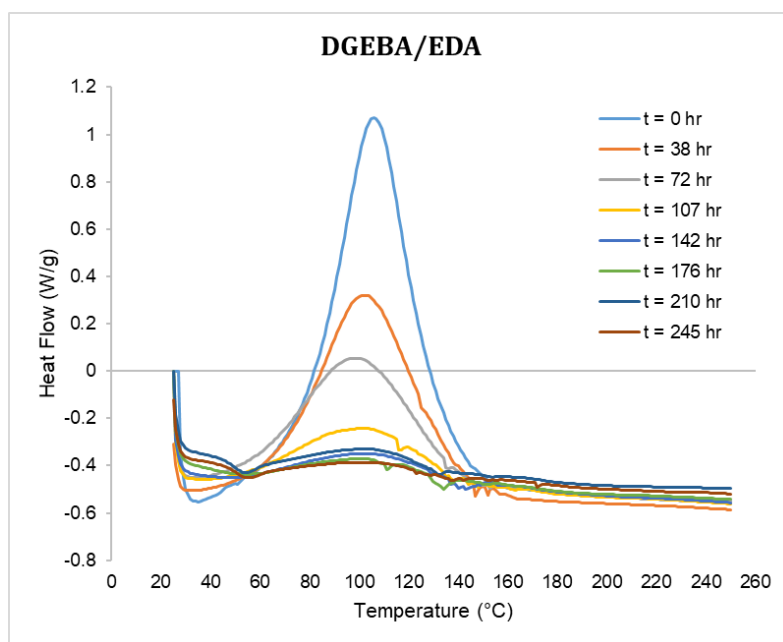
Figure 1. Thermograms showing the heat flow during different sequential periods of room-temperature curing of an DGEBA/EDA sample. The area under each curve is integrated to extract the total heat of reaction (*ΔH*).
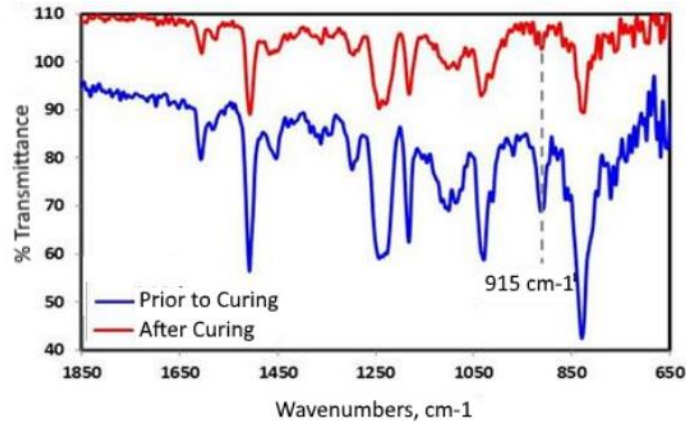
Figure 2: FTIR Spectra of epoxy-amine prior to and after heat curing. The peak at 915 cm^{-1} represents the epoxide functional group that is lost as the density of the crosslinked network increases and the material becomes more rigid. (Figure Credit: Metna Co.)

Consequently, it is necessary for a non-invasive and non-destructive analysis to characterize epoxy samples, before, during and after vitrification. The overall importance of determining various properties of bulk epoxy or epoxy-substrate interfaces relies on their influences on performance of various products that include fiber reinforced plastics (FRPs), adhesively bonded joints and composite encapsulated electronics.[26] Qualities of epoxy-substrate interfaces overtime undergo changes under hygrothermal and mechanical stress in service which lead to property degradation of the epoxy materials.[27] The formation of defects from the degradation of epoxy resins inevitably leads to premature failure in service. The desired use of epoxy materials for aerospace and defense technologies demand a need for effective and inexpensive defect detection to ensure quality control. Therefore, it is ideal to find a technique that can not only monitor the curing of an epoxy to a substrate, but also selectively probe samples at different positions throughout the material to measure molecular mobility and strength of adhesion, ultimately leading to proper defect prevention and analysis.

3

Nuclear magnetic resonance (NMR) relaxometry is an effective method to measure the mobility of polymer macromolecules for quantitative evaluation of local defects and degradation phenomena, and for assessment of the mechanical quality of bonded interfaces.[28] Relaxometry refers to the measurement of signal attenuation following a perturbation through sequences of electromagnetic radiation in nuclear magnetic resonance such as spin-lattice relaxation (T_1), spin-spin relaxation (T_2), and diffusion coefficients (D). NMR probes the chemical environment of atomic nuclei (primarily hydrogen atoms), through their interactions with magnetic fields, to investigate local magnetic effects inside a molecular system. These interactions provide information on inter- and intramolecular structure that reflects physical properties, such as crosslinking, mobility, and rigidity of a sample.[29] Conventional NMR instruments use large superconducting magnets to produce a homogenous magnetic field that can analyze a wide range of compositions of polymeric materials.[30] Magnet homogeneity is directly related to resolution and sensitivity of analysis. Thus, strong, homogenous magnetic fields can measure rigid polymeric materials with relatively small relaxation dynamics. However, these traditional NMR instruments suffer several limitations: they are large, immobile, expensive, and typically can only measure samples that are 5-mm diameter in small glass tubes.

Unlike traditional NMR, single-sided NMR devices, developed in the 1990's, are inexpensive, portable, and easy to use.[31,32] Furthermore, they provide few limitations on the size or shape of the sample that otherwise cannot be measured using conventional NMR instruments. Single-sided NMR devices utilize small, permanent magnets to produce their magnetic fields, thus eliminating engineering intricacy and complications

accompanied with superconducting materials. However, the smaller permanent magnets and open geometry of the instrument can only produce weaker, inhomogeneous magnetic fields, eliminating the ability to collect chemical shift data of molecules. Therefore, single-sided NMR instrumentation focuses on relaxometry measurements of NMR relaxation times (T_1 and T_2) and diffusion coefficients (D) with high accuracy. These measurements allow for the ability to analyze stress and strain of polymers, molecular diffusion, hydration, pore size distributions, and dynamics of solvents.[33] Single-sided NMR has been used to non-invasively characterize physical properties of various samples, including food,[34–38] paintings,[39–42] paper,[43,44] ceramics,[45,46] building materials,[47–49] and even humans.[50–52] Single-sided NMR has also successfully been used to monitor the real-time curing of epoxy resins.[53]

In this thesis, single-sided NMR was used to measure the strength of an adhesive bond to various substrates and surface treatments. T_1 and T_2 relaxation times were measured simultaneously, using a two-dimensional single-sided NMR experiment, to characterize the mechanical strength of an adhesive bond between an epoxy resin and a substrate by correlating the relaxation parameters with surface free energy. These measurements were also used to evaluate local defects and degradation phenomena at bonded interfaces. Both single-sided NMR and DSC were also used to monitor real time epoxy curing with different diamine curing agents at various temperatures. Using the two methods simultaneously allowed for the comparison of the measured extent of cure, chemical cure, and molecular mobility throughout the cure process. T_2 relaxation times of epoxy samples during and after cure were measured to model the cure kinetics of various epoxy resins. Overall, these measurements aim to establish non-destructive techniques

that can both characterize the curing processes of epoxy, measure the strength of

adhesion between two materials, and evaluate the properties of polymer-inorganic

interfaces.

Chapter 2: Epoxy Resins

Epoxy resins were first discovered in 1936 by Pierre Castan of De Trey Freres in Switzerland and Sylvan Greenlee of DeVoe and Raynolds (now known as Celanese Chemical Company) in the United States.[54] They both shared credit for developing Bisphenol A diglycidyl ether from the reaction of Bisphenol A with epichlorohydrin and were licensed a patent for their work.[54,55] Bisphenol A diglycidyl ether, also known as DGEBA (**dig**lycidyl **e**ther of **B**isphenol-**A**) or BADGE , is now one of the most widely used epoxy resins in the industry and is often referred to as a model epoxy system. This epoxy resin was first marketed for dental products but initial attempts to commercialize the resins were unsuccessful. However, in 1946, a company in Switzerland, known as Ciba, was licensed Dr. Castan's work and became the first company to commercialize the production of epoxy resins.[54,55] From that moment on, companies like Ciba, Celanese Chemical Company, Shell Chemical Company, and many more entered in the field of epoxy resins creating patents for composites used for various casting, laminating, and adhesive applications.[5,56] Commercialization of epoxies and expansion of resin varieties proliferated for applications in various industries, most notably in aerospace engineering.

Epoxy resins, also known as thermosetting resins, are a class of adhesive and coating polymers that, once mixed with a curing agent, change irreversibly from a fusible and soluble liquid material into one which is infusible, insoluble, and hardened.[57,58] The curing of these materials is initiated by a chemical means in which chemical reactions form a three-dimensional covalently crosslinked and thermally stable network. The wide variety of epoxy resin applications emanate from the varying properties these materials can have. The final chemical and physical properties of epoxy systems depend on the

molecular structure of the main epoxy chain, structure of the crosslinked network, and density of crosslinks.[58,59] Because of their intractability after cure, it is important to ensure that the epoxy resin being produced is of the correct dimensions and stoichiometry prior to commercial production.

The degree of crosslinking has previously been studied to determine the different effects on curing kinetics and physical properties of cured epoxy resins.[60] It was found that as the density of crosslinking decreases, the coefficient of linear thermal expansion, water absorption, diffusion coefficient, permeability, and flexibility increase due to the looser molecular chain packing[61–63] More specifically, the amount of free volume and crosslinking can affect the polymer chain mobility of the cured epoxy resins. The amount of free volume is the amount of available space between the polymer chains on a microscopic level. By increasing the curing temperature of epoxy resins, the amount of crosslinking is increased as a result of the added thermal energy. Thus, free volume in the polymer chain network on a microscopic level decreases.

Epoxy resins are fully cured when no additional crosslinking can occur and at that point the epoxy reaches its full mechanical properties. The crosslinked network formation from the reaction of a generic epoxy resin backbone with an aliphatic diamine, is illustrated in **Figure 3.** (Aliphatic diamine curing agents are the main curing agents used in this thesis). A nitrogen on an amine group of the diamine curing agent will act as a nucleophile and attack an electrophilic carbon on an epoxide ring of the epoxy resin. This initiates the breaking of a C—O bond causing the opening of the epoxide ring, forming a hydroxyl group with a hydrogen from the amine, and creating a chain extension (**Figure 3a**). As more amines and epoxide groups react, the crosslinking between chains begins.

Each diamine molecule can react with four epoxide rings, as shown in **Figure 3b**. On the larger scale, as a multitude of the monomers react and form bonds with one another, a crosslinked network is formed (**Figure 3c**). Although **Figure 3c** is helpful in visualizing crosslinked networks of epoxy, it is important to note that the final 3D network is not as systematic as illustrated here, but rather is amorphous.

Often, curing of an epoxy resin from a liquid to a solid state is characterized by gelation and vitrification. As the linear epoxy resins are cured into three dimensional cross-linked networks, an infinite network of polymer chains is produced, and the system undergoes gelation. At this point, the total number of molecules is decreased, and a viscous, rubber-like network of infinite molecular weight is produced. Vitrification occurs when the molecular mobility of the final cured epoxy system is reduced, and the epoxy hardens into a more rigid or glassy material. Depending on the composition of resin and hardener used, some epoxy systems may be more flexible than others.

After the epoxy resin is completely cured, it cannot be liquified or "reflow" when heated, but only undergoes a slight softening into a rubbery consistency when heated above its specific glass transition temperature (T_g).[64] The glass transition is not considered a phase change but rather a property of amorphous polymers where the crosslinked network becomes more mobile and flexible over a specific temperature range. The value of T_g is dependent on the mobility of the crosslinked network.[65] In other words, epoxy materials that have a lower crosslink density also have a higher polymer chain mobility because of the amount of free volume in the polymer chain network. Epoxy resins with a higher polymer chain mobility have a lower T_g because less thermal energy is required to transition the molecular structure from a glassy state to a rubbery state. On

the other hand, an epoxy material with a higher crosslink density has a more restrained polymer chain network, making the material less mobile, thus exhibiting a higher T_g. Once the T_g for a specific epoxy material is exceeded, the covalent bonds of the polymer material remain intact while their mobility increases. Therefore, some of the epoxy's physical properties, like stiffness and strength, are altered while above the T_g. The choice of epoxy, curing agent, filler, as well as curing conditions can affect the final T_g of the material. As discussed above, a higher curing temperature increases the amount of added thermal energy initiating more crosslinking of the polymer network, which will in turn increase the T_g. Hence, it is important to understand various curing kinetics and physical properties of epoxy systems to achieve optimal performance for specific applications.

While a basic knowledge of epoxy chemistry is useful for understanding this thesis, a thorough investigation of polymer chemistry is beyond the scope of this thesis. Importantly, the crosslink densities of epoxies affect NMR relaxation parameters, T_1 and T_2, because of the molecular chain packing and (mostly dipolar) coupling between protons. This thesis explores the use of single-sided NMR for measuring relaxation times, T_1 and T_2, to non-destructively probe physical properties and processes of epoxy systems. More specifically, comparing the kinetics and crosslink densities of epoxy resins cured with different curing agents provide insight on their molecular mobility during and after curing. Monitoring changes in T_1 and T_2 relaxation times at polymer-inorganic interfaces determines the mobility of the polymer chain network near and interaction between two materials.
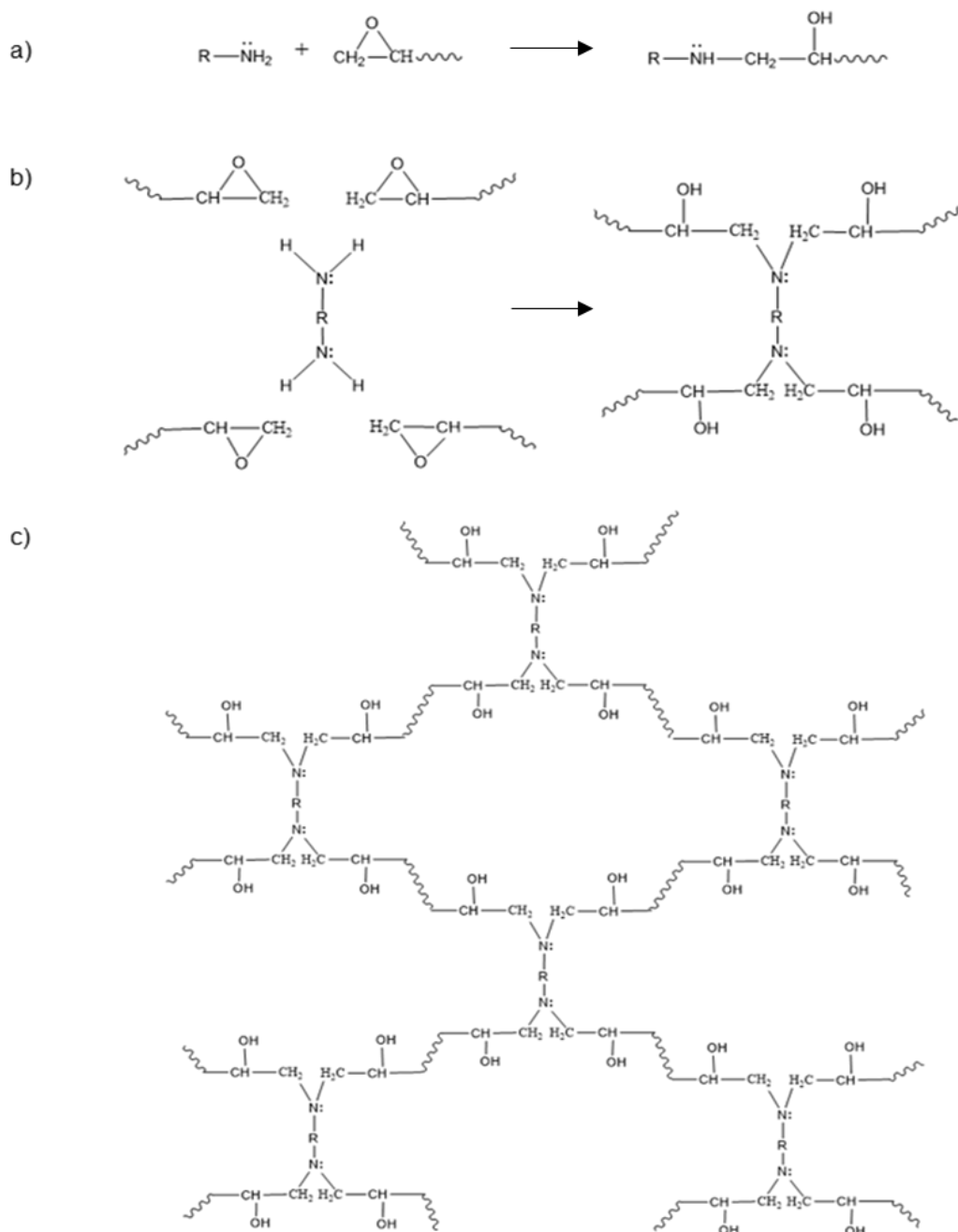
Figure 3: A depiction of the curing process of epoxy resins with an aliphatic diamine curing agent (the main curing agent used in this thesis). Depending on the resin and curing agent used, the R group on the amine curing agent and the "squiggle" on the epoxy molecule shown in this figure can vary. a) Illustration of a nitrogen on the amine functional group acting as a nucleophile and reacting with the electrophilic carbon on an epoxide functional group, thus initiating a ring-opening and chain extension. b) For a single diamine molecule, it can react with four epoxide groups of the epoxy resin. c) As amines and epoxides continue to react, crosslinking between chains continue, thus forming a final three-dimensional crosslinked network. The final crosslinked network is more amorphous than illustrated here.

Chapter 3: NMR Theory

Nuclear magnetic resonance utilizes the physical phenomenon that some atomic nuclei possess magnetic moments causing them to exhibit nuclear spin. Because atomic nuclei are charged, their nuclear spin creates magnetic moments (μ), similar to magnetic fields generated by small bar magnets. Therefore, nuclei are often classified in terms of their intrinsic angular momenta and spin. General principles of quantum mechanics denote that the maximum measurable angular momentum of an atomic nucleus must be an integral or half integral multiple of the reduced Planck's constant ($\hbar$).[66] The total angular momentum of a nucleus is represented by the symbol I and is dependent on the number of protons and neutrons in the nucleus. A nucleus of spin I will have $2I + 1$ total available spin states. If $I = 0$ for an atomic nucleus, then energy transitions are not possible and the magnetic moment (μ) of that nucleus is zero. Moreover, nuclei that have nuclear spins of $I = 0$ are not NMR active. However, if $I \neq 0$ for an atomic nucleus, then energy transitions are possible, thus allowing that nucleus to have more than one energy state in a magnetic field. Overall, for an atomic nucleus that has multiple energy levels, NMR is feasible because of the ability for transitions to occur between those levels. This research focuses on ^{1}H NMR, which has a spin of $I = \frac{1}{2}$ and two possible energy states.

When no external magnetic field is applied, nuclei can orientate their spins freely around their own axes of rotation. Their energy levels are degenerate and therefore, in the absence of external magnetic fields, nuclear spins are disordered but have the same energy. When an external magnetic field (B_0) is applied to nuclei that possess spin, they will interact with the field and align their spins according to their energy states, thus possessing intrinsic magnetic moments (μ). Because the magnetic moment and angular

momentum of an atomic nucleus behave as parallel vectors, magnetic properties of nuclei are often specified by the gyromagnetic ratio (γ) defined by the following equation:

$$\gamma = \frac{\mu}{(I\hbar)} \tag{3.1}$$

where γ is in rad s^{-1} T^{-1} ($\gamma_{1H} = 2.675 \times 10^8$ rad s^{-1} T^{-1}).[67] The gyromagnetic ratio is unique to each atomic nucleus and its sign depends on the direction of the magnetic moment and angular momentum vectors of those nuclei. When no external magnetic field is applied, the bulk magnetization of nuclei in a sample is zero because the vectors are randomly oriented and cancel each other out. However, when an external magnetic field (B_0) is applied, the interaction of the field with the nuclei cause the nuclei to precess (**Figure 4**). The precession of a nucleus is caused by it being "tipped" out of alignment with the external magnetic field (B_0); the resulting torque holds the tip angle constant, hence the conical shape of precession. For example, the precession of a nucleus can be visualized as a spinning toy top that is spinning slightly off its axis of rotation as it precesses around that axis. The angular frequency of precession, defined as the Larmor frequency (ω_0), is given by

$$\omega_0 = \gamma B_0 \tag{3.2}$$

where γ is the gyromagnetic ratio and B_0 is the applied external magnetic field.
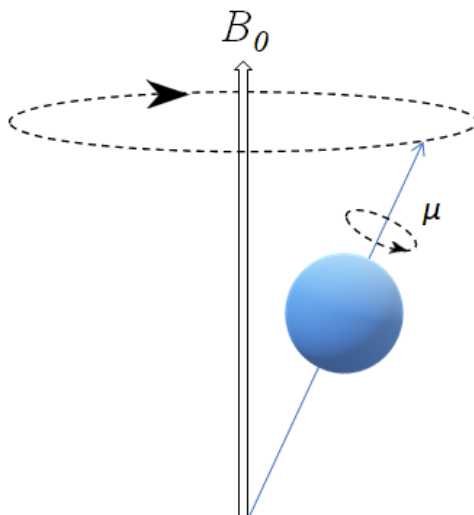
Figure 4: Precession of a nucleus (blue circle) with a magnetic moment (μ) in an applied external magnetic field (B_0) and its magnetization vector. The sign of the gyromagnetic ratio for an individual nucleus determines the direction of precession. This figure represents a negative precession of an ^1H nucleus, which has a gyromagnetic ratio of 42.58 MHz/T.

As previously mentioned, in the presence of an external magnetic field (B_0), spinning nuclei will interact with the field and align their spins according to their energy states. These nuclei can either align their spins with the field, in a low energy state, or against the field, in a high energy state. This is because more energy is required for nuclei to align against the field than with it. In other words, the ground states of atomic nuclei will split into different energy levels that are proportional to the applied magnetic field (B_0). This is known as the nuclear Zeeman splitting (**Figure 5**).[68] The population of nuclei in either energy state is determined by the Boltzmann equation

$$\frac{N_\uparrow}{N_\downarrow} = e^{-\Delta E/kT} \tag{3.3}$$

here $N_\uparrow$ and $N_\downarrow$ are the populations of nuclei in high and low energy states respectively, $\mathit{\Delta E}$ is the energy difference between those two states, k_B is the Boltzmann constant, and T is the absolute or thermodynamic temperature. The difference in energy between the two populations of nuclei is proportional to the applied external magnetic field, considering that reduced Planck's constant and the gyromagnetic ratio are constants, defined as:

$$\Delta E = \hbar\gamma B_0 \qquad (3.4)$$

As determined by nuclear Zeeman splitting, the nuclear spins in either energy state, $N_\uparrow$ and $N_\downarrow$, are equal and opposite in sign. As seen in **Figure 5**, a nucleus like ^{1}H that has a spin of $I = \frac{1}{2}$ has two possible spin states: $+\frac{1}{2}$ and $-\frac{1}{2}$. These spin states are also referred to as parallel and anti-parallel states, respectively. More nuclei exist in the parallel spin state since it is more energetically favorable. Though, the difference in population of spin states is very small, it is key to the theory behind NMR spectroscopy.[69] For example, the difference in the population of spin states is about 10 out of 1 million protons for a 300 MHz NMR instrument. This population difference is directly related to the magnetic field strength and inversely related to temperature. Therefore, the higher the magnetic field strength and the lower the temperature, the higher the difference in population of spin states. Because the difference of nuclei that populate the parallel and anti-parallel spin states is relatively small, majority of the nuclear spins cancel one another out leaving only a small excess in the lower energy state ($N_\downarrow$). Thus, the magnitude and direction of the net bulk magnetization vector (M) is a result of the slight excess of the lower energy projections of nuclei, which are parallel to the external magnetic field (B_0). This cancellation of nuclear spins is called polarization (p) and represents the fraction of

nuclear spins that construct the measured NMR signal. The polarization can be calculated by the following equation:

$$p = \frac{N_\uparrow - N_\downarrow}{N_{total}} \qquad (3.5)$$

where $N_\uparrow$ and $N_\downarrow$ are the populations of nuclei in high (−½ spin) and low (+½ spin) energy states respectively.
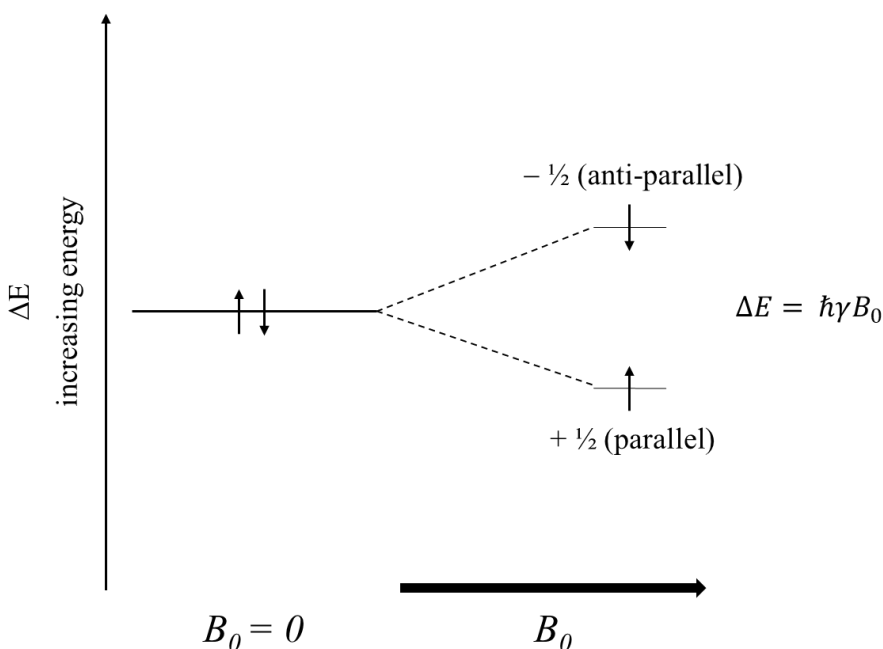
Figure 5: A visual representation of nuclear Zeeman splitting of a nucleus with $I = ½$ and its two spin states in a magnetic field, B_0. Nuclear spins of -½ are denoted as anti-parallel and are in a higher energy level ($N_\uparrow$) than nuclear spins of +½ which are as denoted parallel and are in a lower energy level ($N_\downarrow$). The direction of the magnetic field is up, parallel to the ordinate, and it increases from left to right. Thus, larger magnetic fields increase the difference in energy, ΔE, between the two spin states.

For visual interpretation, when modeling multiple nuclei in an applied magnetic field, magnetic moment vectors can be used to depict nuclear precession (**Figure 6**). The individual magnetic moments of nuclei in a sample are graphed on a 3D coordinate plane where the net bulk magnetization vector M is parallel to the magnetic field B_0. When the sample is at equilibrium, the magnetic moments of nuclei will remain precessing about the z-axis at a frequency equal to the Larmor frequency (ω_0).
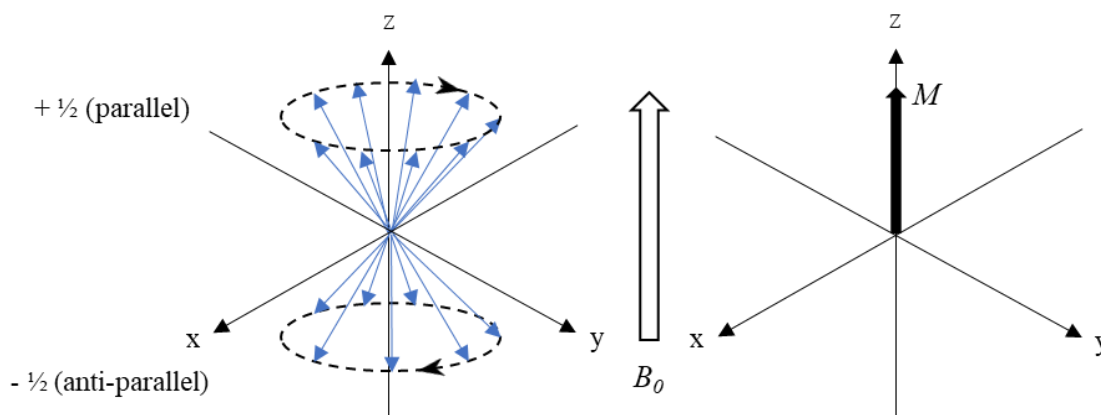
Figure 6: Precession of $I = \frac{1}{2}$ magnetic moment vectors, at the Larmor frequency (ω_0), in an applied magnetic field B_0 with a bulk magnetization vector M. More nuclei align with the magnetic field in the $+\frac{1}{2}$ spin state as it is more energetically favorable.

In order to tip the net bulk magnetization vector away from the z-axis, a radiofrequency (rf) pulse is applied to form an oscillating magnetic field, denoted B_1. When a nucleus of an atom is placed in a magnetic field and exposed to rf radiation, it will absorb that energy and resonate at a specific frequency of that radiation. Because the Larmor frequency correlates the frequency in MHz that a specific nucleus with a gyromagnetic ratio, γ, in a magnetic field, B_0, precesses at, then a rf pulse tuned to that same frequency will cause the nucleus to interact with B_1. The nuclei will begin precessing around B_1, thus aligning their spins with the new magnetic field and tipping

the net bulk magnetization vector away from the z-axis. This is a basic understanding of resonance. The magnitude of B_1 is much smaller than and perpendicular to B_0. The power of the rf pulse and the time allotted can change the angle at which the net bulk magnetization vector is tipped from the z-axis. Because the magnitude of B_0 is much larger than B_1, the z-component of the net bulk magnetization vector cannot be measured, therefore a 90° tip angle will result in the largest amount of measured signal from B_1. Once a 90° tip angle of the net bulk magnetization vector is produced, it begins to precess about the x-y plane. This precession in the x-y plane creates a changing magnetic field which in turn creates an oscillating electric field— just like that of an oscillating electric field in a coil of wire creating an oscillating magnetic field in the coil. This electrical current can be detected by the NMR spectrometer and resolved to produce the measured signal. Over time, the net bulk magnetization vector will continue to reach equilibrium, aligning back with B_0. This causes a decay of measurable signal, which is a phenomenon behind the basis of NMR experiments and will be discussed in the following sections.

3.1 Single-Sided NMR Theory

Traditional NMR is traditionally used to measure chemical properties of samples via chemical shifts and *J*-couplings by measuring their response to an rf pulse.[70–72] The fundamental NMR equation (Eq. 3.2) denotes that each proton in a given magnetic field will have a single resonance frequency (Larmor frequency). Hydrogen atoms that are covalently bonded in a molecule are shielded by some degree from the surrounding electrons. The chemical environment around each hydrogen atom effects the amount of shielding they experience. This shielding inevitably leads to a different effective magnetic field that is felt by each hydrogen atom; because their surrounding chemical

environments are not always the same, the effective magnetic field they experience is also not the same. This results in differences in the resonance frequencies of the hydrogen atoms known as chemical shifts. In order to resolve chemical shifts, a homogenous magnetic field is needed. Traditionally, a 300 MHz (7.05 T) NMR spectrometer, or stronger, is used to produce these homogenous magnetic fields. However, due to cost, engineering and sample limitations, an NMR of this sort is not ideal for the study of epoxy resins.

In contrast, the NMR-MOUSE (Magitrek; Wellington, New Zealand),[73] the single-sided instrument used in this thesis, consists of four permanent magnet blocks with anti-parallel magnetization that can produce a relatively homogenous magnetic field, B_0 (**Figure 7**).[32] A surface rf coil is positioned in the center of the magnets to produce a perpendicular rf field (B_1) that creates a sensitive volume located approximately 5 mm above the face of the magnet. Because of this, samples can simply be placed directly on top of the magnet for non-destructive measurement. Thus, a single-sided NMR device is advantageous for *in-situ* measuring of a variety of sizes and shapes of samples. Due to the open-faced geometry, single-sided NMR devices have an intrinsic magnetic field gradient that is permanent and strong, with varying strengths in T m^{-1} dependent on the specific magnet.[32] Therefore, nuclei farther away from the magnet experience a lower field strength than those closer to the magnet. Because of the strong magnetic field gradient and field inhomogeneities, the analysis of chemical shifts using typical spectroscopy from traditional NMR is impossible due to the overlap of spectral peaks on the ppm scale and decreased signal-to-noise ratio (SNR). In other words, the individual permanent magnets of a single-sided NMR device have field inhomogeneities themselves that are bigger than

19

the resolution needed to acquire chemical shift data. However, despite the magnetic field

inhomogeneities, NMR relaxometry can still be acquired using spin echo techniques.

Depending on the SNR and the spatial arrangement of the sample, spatial resolution can

provide profiles of samples that approach as close as 1–10 microns to surface of many

substrates.[73,74] Thus, for an epoxy resin bonded onto a substrate, spatially resolved signal

of various relaxation parameters can be acquired to characterize the material using single-

sided NMR.
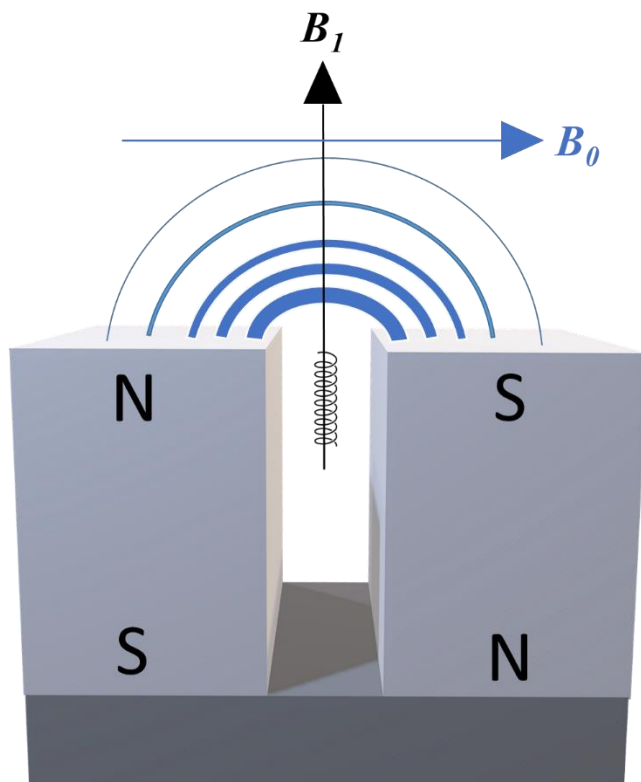
Figure 7: An illustration of the single-sided NMR device used in this thesis. The four
permanent, antiparallel block magnets produce the applied inhomogeneous magnetic
field, B_0, in blue. The intensity of the magnetic field gradient, B_0, decreases farther away
from the surface of the magnets. Positioned between the two block magnets is the
radiofrequency coil in black and the rf magnetic field in black. The rf magnetic field is
responsible for exciting the bulk magnetization vector that allows for the precession of
nuclei in the x-y plane. Thus, permitting the measurement of various relaxometric
information from a sample.

3.1.1 Spin-Spin Relaxation

One type of NMR relaxation that occurs is spin-spin or transverse (T_2) relaxation. T_2 relaxation corresponds to the decoherence or decay of the bulk magnetization in the x–y plane. Immediately after the bulk magnetization is tipped to the x–y plane by a 90° rf pulse, the aligned, precessing spins are in-phase with one another. However, due to inhomogeneities of the magnetic field, variations in the nuclear precession frequencies cause some to fall behind the bulk magnetization vector while others are ahead of it. This leads to a "fanning out" effect of the bulk magnetization vector, also known as de-phasing of nuclear spins, resulting in no detectable signal.[75] Thus, T_2 corresponds to the amount of time it takes for precessing spins to lose phase coherence. T_2 relaxation is subject to rotations and translations of nuclei interacting with local magnetic fields of neighboring nuclei causing phase decoherence of spins. More specifically, T_2 relaxation characterizes dipolar coupling of protons that are translating throughout a sample with respect to one another. Small T_2 values are characteristic of rigid materials, like a highly crosslinked epoxy system, because it has stronger intermolecular couplings and its molecular rotation and translation is limited. Whereas large T_2 values characterize materials that allow relatively free molecular motion, like water or other low-viscosity liquids, preserving the nuclear phase coherence.

The intensities of T_2 signals can be measured using the Carr-Purcell-Meiboom-Gill (CPMG) sequence.[76,77] A CPMG sequence is utilized to reduce accumulative distortions introduced by imperfections of the rf pulse and resonance offset. However, the traditional pulse sequence used with conventional NMR cannot be performed. Due to the magnetic field gradient of a single-sided NMR device, nuclear spins precess at various

frequencies proportional to the effective field strength at each nucleus. When a rf pulse is applied, the nuclear spins are not tipped all at the same angle as they would be using a traditional NMR instrument with a homogenous magnetic field. Immediately following the rf pulse, the spins are not perfectly in-phase to begin with, except at time zero where there are no in or out of phase nuclear spins. Therefore, the remaining de-phasing of spins occurs relatively quickly. After the rf pulse is transmitted, the current in the coil must decay to zero to rid of the residual energy from generating the excitation pulse. This is known as the coil dead time. The dead time is utilized to limit damage to the rf coil itself so that the receiver coil won't become overloaded by both the residual energy from the excitation pulse and the signal decay from dephasing nuclei. However, after the dead time is allotted, the T_2 relaxation of a sample would decay too fast by the time it is safe for the receiver coil to be switched on for signal acquisition.

To bypass this using a single-sided NMR device, echoes, developed by Erwin Hahn,[78] are utilized in a CPMG sequence. The CPMG sequence, illustrated in **Figure 8**, comprises a 90° excitation pulse, followed by a series of 180° refocusing pulses. Due to the magnetic field gradient, some nuclei are precessing faster than others. When the refocusing pulse is applied, the nuclei continue to precess at the same speed and direction, but their phase has been inverted. Thus, the refocusing pulses allow the faster spins to catch up to the slower spins causing the broadened signal to constructively converge, creating an echo. Each echo can be measured during the acquisition periods. Eventually the measured signal will decay to zero due to the relaxation of the hydrogen spins and loss of phase coherence, often known as homogeneous and inhomogeneous broadening, despite the refocusing pulses of the CPMG sequence. The loss of phase

coherence is greatly affected by dipolar interactions between nearby spins that interrupt their individual precessional frequencies. As interruptions of precessional frequencies occur, the nuclei no longer constructively converge to form an echo, resulting in a decay of signal over time. This decay of signal can be quantified as the spin-spin relaxation time constant (T_2). The T_2 relaxation decay can be modeled using a simple first order kinetics exponential decay:

$$f(t) = Ae^{-t/T_2} + c \qquad (3.1.1)$$

where t is time, A is the amplitude of the decay curve, T_2 is the relaxation constant, and C is the y-offset. The y-offset, in this case, reflects the presence of instrumental and/or acquisition imperfections that result in a non-zero noise baseline.

In addition to T_2 relaxation rates, single-sided NMR can probe molecular mobility due to its effect on changes in signal intensity.[77] For example, by analyzing the T_2 values within an epoxy sample throughout the cure time, information about how spin-spin relaxation changes throughout different stages of the curing process can be obtained. If hydrogen atoms were to remain stationary during an experiment, then the relative spins would produce a perfect refocusing. This occurrence would create echoes that are measured at the maximum possible signal intensity. However, if hydrogen atoms move throughout a sample, moving across the field gradient during an experiment, then the magnetization will become imperfectly refocused causing signal attenuation over time. Information about molecules' abilities to rotate within, as well as translate through, a sample can be evaluated from the T_2 data. Smaller T_2 values indicate that molecules are more constrained. Therefore, the chemical kinetics at different positions within a sample,

like in the bulk versus at the interface of a substrate, can be observed throughout the

curing process as T_2 data changes.
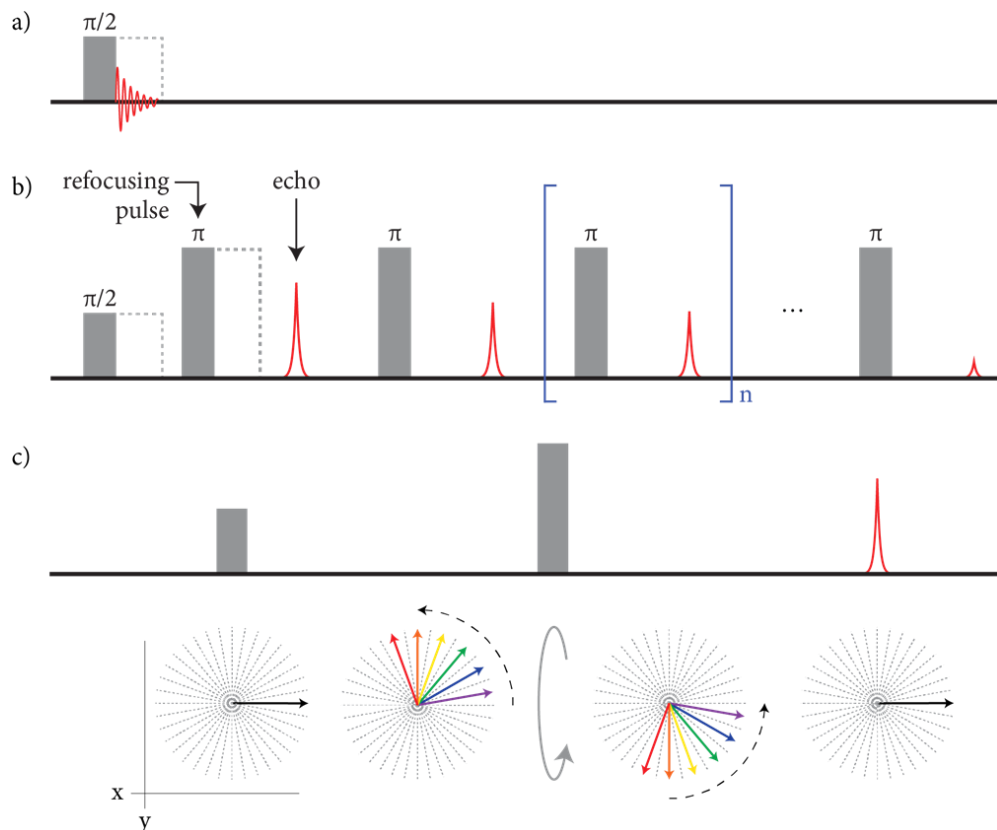
Figure 8: The Carr-Purcell-Meiboom-Gill (CPMG) pulse sequence utilized in this thesis. a) Representation of a traditional free induction decay signal measured by traditional NMR for comparison. b) Transverse magnetization of the hydrogen atoms is excited by the 90° pulse, followed by 180° refocusing pulses and the constructive convergence of signal from the in-phase hydrogen spins that form an echo, which is measured between each acquisition. c) A zoomed-in illustration on the occurrence of a single echo. The 90° pulse aligns the hydrogen spins along the x-y plane. Due to the inhomogeneity of the magnetic field, the hydrogen atoms that are farther away from the magnet will precess at a slower frequency (purple arrow) than those that are closer to the magnet (red arrow). Thus, resulting in a dephased magnetization (colored arrows). The 180° refoucusing pulse inverts the phase of the nuclear spins. The spins then reconverge and constructively form an echo. After many refocusing pulses, an echo train can be collected and the signal will continue to decay due to the relaxation of the spins, allowing for the characterization of T_2. (Figure credit: Dr. Tyler Meldrum).

3.1.2 Spin-Lattice Relaxation

Another relaxation parameter that can be measured using a single-sided NMR device is spin-lattice or longitudinal (T_1) relaxation. T_1 relaxation of nuclei refers to the re-establishment of proton spins to their equilibrium state according to the Boltzmann distribution (Eq. 3.3) After an external magnetic field is applied to a sample and a 90° rf pulse has tipped the net bulk magnetization vector to the x-y plane, it takes time for the nuclear spins to return to equilibrium and reestablish the z component of the bulk magnetization. The time it takes for the bulk magnetization vector to return to the z-axis can be measured as T_1. Because signal detection in NMR occurs in the x-y plane, the intensity of that signal will decay over time, therefore T_1 is measured as an exponential growth of the restored z component of magnetization. For nuclei with spin $I = \frac{1}{2}$, the restoration of the z component of the bulk magnetization vector measured using a saturation recovery experiment follows an exponential recovery:

$$f(t) = A\left(1 - e^{-\frac{\tau}{T_1}}\right) + c \qquad (3.1.2)$$

where τ is time allotted for the relaxation of the z component of magnetization and T_1 is the rate at which the spin-lattice relaxes. T_1 can be measured using either an inversion or saturation recovery pulse sequence. This thesis focuses on the measurement of T_1 relaxation times using only a saturation recovery pulse sequence because it is more suitable for single-sided NMR instruments. The saturation recovery sequence, illustrated in **Figure 9**, comprises a train of 90° saturation pulses, followed by a 90° excitation pulse and a series of 180° refocusing pulses. Five 90° rf pulses, called the saturation block, are used initially to saturate the bulk magnetization along the x-y axis. This is also referred to

as a preparation period used to move the bulk magnetization away from equilibrium. An evolution period τ follows the saturation block in which the nuclear spins are free to relax to equilibrium, ranging from a τ of (almost) zero to a maximum recovery value. Another 90° rf pulse is used to tip the net magnetization back to the x-y plan and a series of 180° pulses are then used to generate echoes (like seen in the CPMG sequence in section 3.1.1) for signal acquisition.
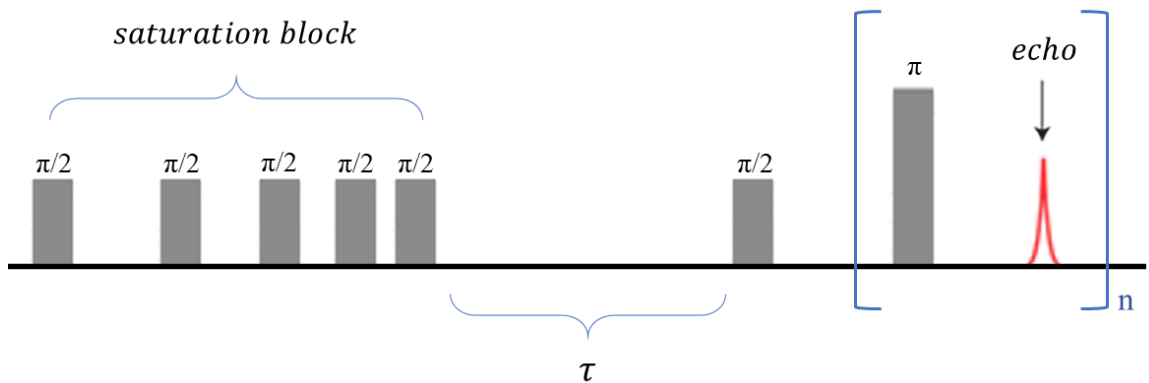
Figure 9: The saturation recovery pulse sequence utilized in this thesis. The saturation block consists of a train of 90° rf pulses to saturate the transverse magnetization. A free evolution period of time τ follows the saturation block where the nuclear spins relax to equilibrium, restoring the bulk magnetization along the z-axis. Thus, the longitudinal magnetization grows from zero to its maximum value (governed by Eq. 3.1.2). Another 90° rf pulse is used to tip the bulk magnetization back to the x-y axis with a CPMG sequence used to detect the signal generated by the formation of echoes.

Overall, T_1 is the time it takes for rotations of both intramolecular functional groups and whole molecules to relax to thermodynamic equilibrium. The T_1 relaxation occurs through interactions of nuclear spins with the surrounding lattice. In other words, T_1 relaxation is affected by molecular rotations and the gyromagnetic ratio of nuclei in a sample and determines how effectively energy transfers can occur between individual nuclei and the surrounding lattice. T_1 is the shortest when the Larmor frequency matches the natural frequency of rotational motion often known as the molecular tumbling rate.[79] Moreover, molecules that are rotating and tumbling faster or slower than the Larmor frequency exhibit less efficient energy exchanges with the surrounding lattice and thus have longer T_1 relaxation times. For example, a sample of liquid water has a relatively long T_1 relaxation time because its molecules have a relatively high molecular mobility with a wide range of tumbling rates and is inefficient at longitudinal relaxation. However, water molecules that have ingressed a cured epoxy sample and are trapped in between the crosslinked chains (small pore size) are more restricted, thus rotating at a slower rate that is closer to the Larmor frequency with a relatively shorter T_1 relaxation time.

The relationship between T_1 and T_2 relaxation times is illustrated in **Figure 10**. The minimum point on the T_1 relaxation curve is indicative of molecular tumbling rates of a material matching the Larmor frequency. Molecular tumbling rates that are slower or faster than the Larmor frequency fall to the left and right of that minimum, respectively, with larger T_1 relaxation times. However, T_2 relaxation times increase as molecular tumbling rates increase, with a plateau seen near the Larmor frequency. Thus, T_1 and T_2 relaxation times are more similar for water-like materials that have large molecular

27

tumbling rates as opposed to the divergence of T_1 and T_2 relaxation times seen in solids or

highly crosslinked epoxy materials with smaller molecular tumbling rates.
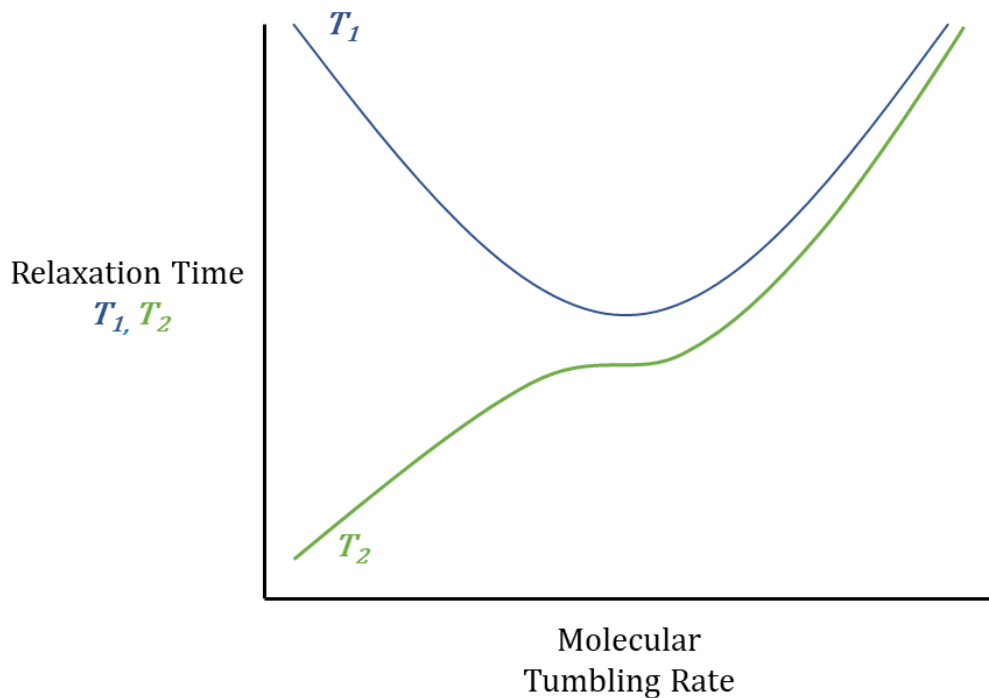
Figure 10: Behavior of T_1 and T_2 relaxation times as a function of molecular tumbling rates.

It is important to understand the T_1 of a material when designing NMR

relaxometry experiments because T_1 represents the amount of time it takes for spins in a

sample to return to equilibrium. Because of this, $T_1 \geq T_2$. If rf pulses for consecutive scans

are applied too soon after one another, then the magnetization does not have enough time

to recover and no population difference occurs resulting in no detectable signal. A time of

$5T_1$ between scans allows the bulk magnetization to recover by 99.93%. All in all, T_1

gives the minimum amount of time needed between pulse sequences to allow the bulk

magnetization vector to re-align with the z-axis.

3.1.3 Two-Dimensional T_1–T_2 Measurements

An alternative to performing T_1 saturation recovery and CPMG experiments separately is to do a multi-dimensional approach.[80] The two-dimensional T_1 saturation recovery and CPMG experiments are particularly useful to show how spins with different relaxation parameters are related to one another. More specifically, 2D T_1–T_2 measurements can show the relationship between T_1 and T_2 relaxation times that can provide more information on the molecular motion of the polymer network than a saturation recovery or CPMG experiment can determine alone, like the correlation between pools of T_1 and T_2 relaxation in a material. In addition, T_1–T_2 measurements allows for the extraction of T_1/T_2 ratios throughout a sample.

Two-dimensional T_1–T_2 measurements can be performed by using simultaneous saturation recovery (**Figure 9)** and CPMG (**Figure 8**) experiments to analyze T_1 and T_2 relaxation times respectively at each spatial position. The T_1–T_2 pulse sequence is very similar to the one-dimensional saturation recovery experiment, however measurements are collected in the direct and indirect dimensions. The direct dimension measures the echoes from the CPMG experiment, which derives the T_2 relaxation time. The indirect dimension measures the saturation recovery with varying τ between each CPMG measurement to build up a T_1 relaxation with a designated number of T_1 points. For each different value of τ, the entire measurement is repeated. Essentially, the T_1–T_2 measurement is comprised of an initial T_1 point measured from a saturation recovery pulse sequence with time τ and an entire CPMG experiment to follow, which is then repeated all over again for another variant of time τ until the total number of designated T_1 points are collected. Because of this, the T_1–T_2 measurements inevitably require more

time to complete the entire two-dimensional measurement. Together, T_1–T_2

measurements reveal the nature of molecular motion of epoxy resins whether it's bonded

to a substrate, confined, or viscous.[81] Despite the time intensive property of the two-

dimensional T_1–T_2 experiments, they are more automated, and provide data with higher

SNR due to the increased amount of measurements, both of which offer significant value

to single-sided NMR when probing the bulk and interfacial regions of epoxy resins cured

to various substrates. This will be discussed in more detail in Chapter 5.

Chapter 4: Single-Sided NMR

The single-sided NMR experiments in this thesis were carried out using a PM5 NMR-MOUSE (Magitrek; Wellington, New Zealand) operating at 19.44 MHz ^{1}H frequency (0.46 T) with an intrinsic magnetic field gradient of 23.5 T m^{-1}. The PM5 is connected to a Kea2 spectrometer, also by Magitrek, operable at up to 400 MHz frequencies. The sensitive region of the rf coil is 25×25 mm in area, approximately 200–300 µm thick, and can obtain signal from a maximum depth of 5 mm into a sample. During measurements, zero, one, or two spacers (both 2 mm thick) can be used to position the transmit/receive rf coil closer to the sample ultimately reducing the maximum depth the sensitive region can probe but increasing the signal-to-noise (SNR) ratio. The PM5 magnet is mounted on a mechanical lift (Magitrek) that moves the magnet vertically in increments of 10 µm with respect to the sample, to probe various depths of the epoxy materials. The PM5 magnet, spectrometer, and lift are all accompanied by a PC laptop running the program Prospa (Magitrek) which is designed to generate the rf pulses, move the lift, and acquire data using various pulse sequences and experiments. The external design of the PM5 can be seen in **Figure 11**.

Figure 11: The PM5 NMR-MOUSE apparatus used in our lab. (A) The PM5 magnet (black) mounted onto the mechanical lift (blue) with aluminum housing and frame. (B) The sampling area for the magnet with a cured bulk epoxy sample sitting on top of the sensitive region. (C) The climate chamber that housed the PM5 NMR-MOUSE for temperature controlled real-time epoxy cure kinetic experiments (see Chapter 6). (D) The Kea2 spectrometer.

Epoxy samples were placed directly on top of the PM5 magnet for data acquisition (**Figure 12a**). For an epoxy resin bonded onto a substrate, the bulk epoxy and the interfacial regions can be probed to spatially resolve and characterize the material. In order to probe interfacial regions, the region itself must be spatially located within the sample. As seen in **Figure 12b**, the magnet can be moved using the mechanical lift, CPMG measurements are taken at incremental depths, or 'slices', to determine the region of greatest signal intensity within the sample. This allows for developing a profile of the sample. Because some substrates used in this thesis don't exhibit ^{1}H NMR signal (i.e., they are proton-free materials), the interface can easily be located as the region where the epoxy signal decays or diminishes (**Figure 12b**).
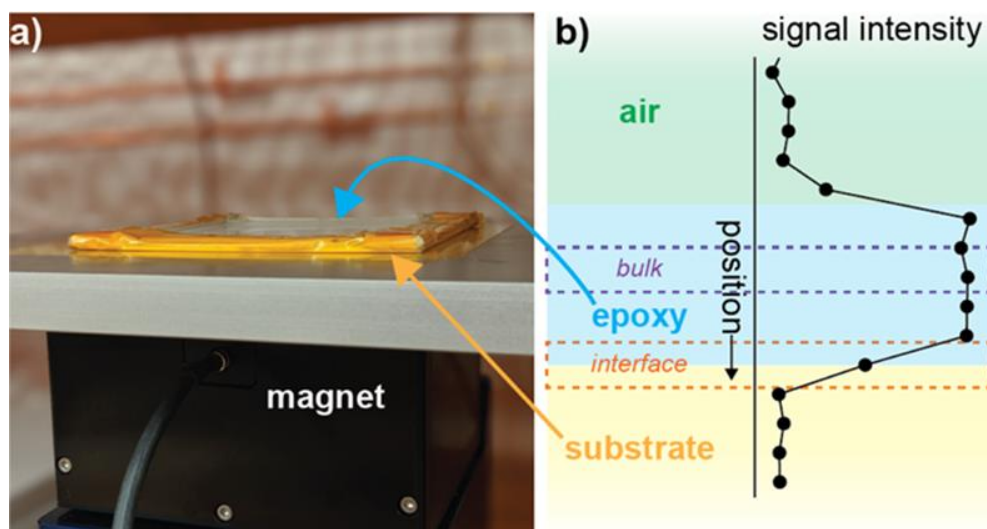
Figure 12: The spatial orientation of sample measurement using the NMR-MOUSE. a) Photograph of an epoxy resin cured onto a substrate and placed on the top of the magnet for sample analysis. The sample is composed of an epoxy resin (~1 mm thick) bonded onto an alumina substrate (~1 mm thick). The orange tape is used to contain the epoxy resin onto the substrate during the cure process. b) Illustration of the signal vs. intensity plot of the materials that the sample consists of in relation to their orientation on top of the magnet. The plot shows that the signal intensity is highest in the epoxy material. There is only noise seen relative to the air and the substrate due to the lack of protons in those regions. The position located at the interface of the epoxy and substrate is where the signal is sharply lost, allowing for the determination of where that interface is specifically located. (Figure credit: Dr. Tyler Meldrum).

Once the region of interest in the epoxy sample is localized, spatially resolved T_1, T_2, and T_1–T_2 measurements can be performed. The echoes measured from relaxation pulse sequences discussed in Chapter 3 are recorded as a series of complex points, each representing an average of signal over the spectrometer dwell (digitization) time, which in this case is 1 μs. The echoes can be Fourier transformed to connect acquisition parameters, like dwell time, with frequency parameters, like the bandwidth of the signal itself. In other words, Fourier transformation converts the signal from the amplitude versus time–domain into an amplitude versus frequency–domain. A simple representation

of a Fourier transformation of two different sine waves can be seen in **Figure 13**. More specifically, the Fourier transform is a mathematical approach to analyze different parts of the signal by displaying it in its conjugate frequency domain. The continuous one-dimensional Fourier Transform function is governed by

$$F(v) \propto \int_{-\infty}^{\infty} f(t)e^{-i2\pi vt}dt \qquad (4.1)$$

where $F(v)$ is the frequency spectrum, v is frequency, $f(t)$ is the signal, and t is time. The signal, $f(t)$, contains superimposed sine and cosine frequencies in which $F(v)$ breaks down all the individual peaks correspondent to each individual frequency that made up the signal. The Fourier transform of a real signal, $f(t)$, can be broken down into two separate integrals where the real components of the Fourier transform are the decomposition of cosine functions and the imaginary components are the decomposition of sine functions from a signal.[82] If $f(t)$ is a detected signal from an echo generated using an NMR pulse sequence experiment with t measured in seconds, then $F(v)$ is the is its frequency spectrum with v measured in Hertz (s^{-1}).
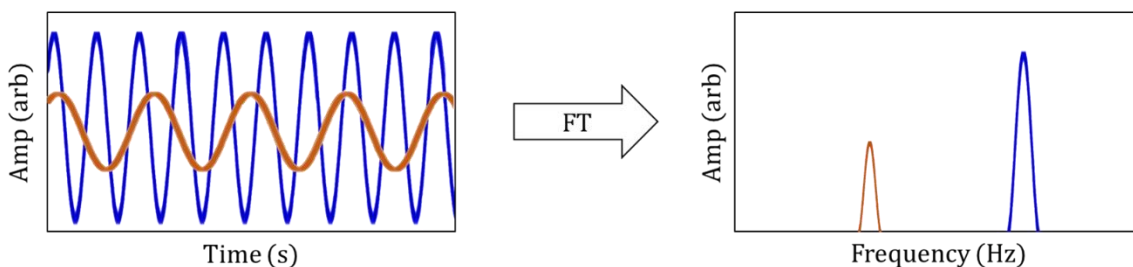
Figure 13: Fourier transform of two sine waves with different amplitudes and periods in the time domain resulting in their corresponding peaks in the frequency domain. The orange sine wave has a smaller amplitude and frequency than the blue, which can be easily seen in the frequency domain after Fourier transform on the right.

Because the precession frequency of the hydrogen spins is proportional to the magnetic field gradient of the PM5, the Fourier transformation of the echoes is itself proportional to the spatial position, providing a spatially resolved decay.[83] Therefore, in the presence of the magnetic field gradient, the distribution of frequencies can correlate to a spatial distribution. Fourier transform of signals can result in a one-dimensional profile of the signal by distinguishing the depths of nuclei in a sample, allowing for higher precision in locating interfacial regions. Once each echo produced from a pulse sequence experiment is individually transformed into the spatial domain, the signal amplitude at specific acquisition times can be graphed to determine the variance in signal at different positions within the sensitive region of the rf coil. Then, the NMR decay envelope from successive echoes can be subjected to an inverse Laplace transformation (ILT) from which spatially resolved T_1 and T_2 distributions can be generated.[83] The ILT converts the data into a relaxation time relative to positions within the material. This procedure, depicted in **Figure 14**, can be repeated consecutively to build a T_2 or T_1–T_2 distribution map with respect to cure time, dependent on the pulse sequence used. It is important to note that the ILT algorithm can generate unreliable results if the noise in the measurements are too is high.[84] Therefore, replicate measurements with a large number of scans ensure precision and repeatability in the final results.

Using the mechanical lift, T_1–T_2 distributions can be measured throughout the entire thickness of a sample by performing two-dimensional T_1–T_2 experiments at various positions within a sample. Monitoring T_1–T_2 distributions throughout a sample can provide information on the molecular mobility by showing how both T_1 and T_2 relaxation times vary with position. The ratio between T_1/T_2 at an epoxy/substrate interface can

35

further be correlated with the surface free energy to give a better understanding of the adhesion strength between two materials. These investigations will be discussed in detail in Chapter 5.

Conversely, by monitoring the real-time curing of an epoxy resin using consecutive CPMG experiments, the various T_2 values at their respective locations within the sample can be used to understand how the spin-spin relaxation at specific positions change throughout different stages of the curing process. Therefore, the chemical kinetics at different positions within a sample throughout the curing process can be observed. Comparing different cure rates and T_2 values amongst various curing agents and epoxy resins can help to better understand the physical properties of these systems during chemical cure. These investigations will be discussed in Chapter 6.
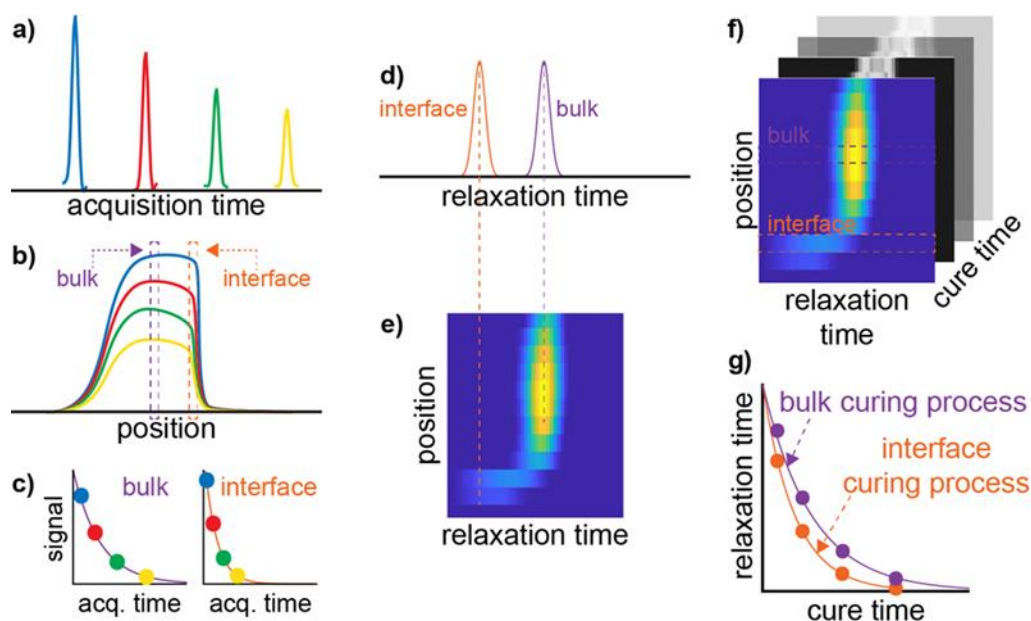
Figure 14: Diagram of data processing to quantify T_2 distributions at different cure times along with the determination of kinetic properties relative to the bulk and interface of the sample material. a) A series of CPMG echoes are collected over a period of time during the experiment. b) A Fourier transformation of each echo at a specific acquisition time results in a spatial profile of the signal, converting the time domain into a position domain. The sharp loss of signal on the right side of the bell curve indicates the position located at the interface c) By extracting the signal at specific acquisition times relative to the position in the sample, a graph can be used to depict the variance in signal at different positions. d) Using inverse Laplace transformation, the position domain can be converted to a relaxation time domain to create a relaxation spectrum to reveal how the rate of decay changes at different positions within the sample. e) Using MATLAB programming, a z-T_2 map can be illustrated. f) Repeating parts a-e throughout the duration of the cure process can generate a z-T_2 map over cure time to analyze how the relaxation decay at that position changes throughout time of cure. g) Using an appropriate model function to fit the T_2 relaxation vs cure time data can help determine the underlying chemical kinetic properties at different positions within a sample. (Figure credit: Dr. Tyler Meldrum).

4.1 Considerations of spatial resolution

The change in proton frequency throughout the magnetic field gradient limits the spatial extent over which a sample can be measured at one point because of a combination of various effects on the spatial resolution of data. The PM5 gradient of 23.5 $T\,m^{-1}$ corresponds to a change in proton frequency of 1000 Hz μm^{-1}. This change in the frequency of hydrogen spins only truly works in a perfectly linear range. Obviously, the magnetic field gradient of the PM5 is not perfectly linear (due to the nature of placing four permanent blocks next to one another with an open geometry), however when concerned with only the sensitive region of the rf coil, the gradient is relatively linear over that slice of spatial region.

Overall, the spatial resolution laterally is approximately 2.5-cm x 2.5-cm, defined by the diameter of the rf coil, and cannot be changed because signal is always acquired over the whole area of the sensitive region. The spatial resolution in the axial dimension, however, is quite complicated and can range from 5 to 300 μm because it is affected by a combination of factors including experimental parameters, the magnetic gradient causing broadening of signal, and the rf coil bandwidth not being big enough to receive all of the signal frequencies. Long acquisition times, when relating to Fourier transformation of signal, result in a more narrow or certain value in the frequency spectrum. Therefore, an epoxy resin with a very fast relaxation decay will need to be sampled quickly with a shorter acquisition time, resulting in a broader frequency domain spectrum, ultimately limiting the spatial resolution.

Another limitation of spatial resolution of the PM5 is caused by the bandwidth of the rf coil, which limits both the transmission and receiving equally. The rf coil is designed so that within a certain frequency range the signal resonates within the coil, however, outside of that frequency range the signal dissipates rapidly. So, the questions arise of how thick of a slice can be excited and how thick of a slice can be received within the bandwidth of the rf coil. Using short, high powered pulses on the PM5 allow for broad range excitation, therefore spatial resolution is typically unhindered. However, when receiving signal, only signal that is within the frequency of the rf coil can be acquired, so any other signal outside of that bandwidth is lost resulting in a limitation of spatial resolution.

The final limitation of spatial resolution stems from the tilt of the slices, with respect to the receiver, resulting in a loss of coplanarity. The sensitive region of the rf coil is 250 μm thick so, if a sample is tilted by even 10 percent, then the 10 μm region that was being probed becomes stretched over a much larger area with respect to the rf coil. Therefore, the signal becomes blurred out across the slice resulting in a lower spatial resolution. Samples can be tilted with respect to the rf coil by uneven layering of materials or bowed substrates inhibiting samples from lying flat against the face of the sensitive region. An illustration of data acquisition from a tilted epoxy sample in the sensitive region of the rf coil can be seen in **Figure 15.**
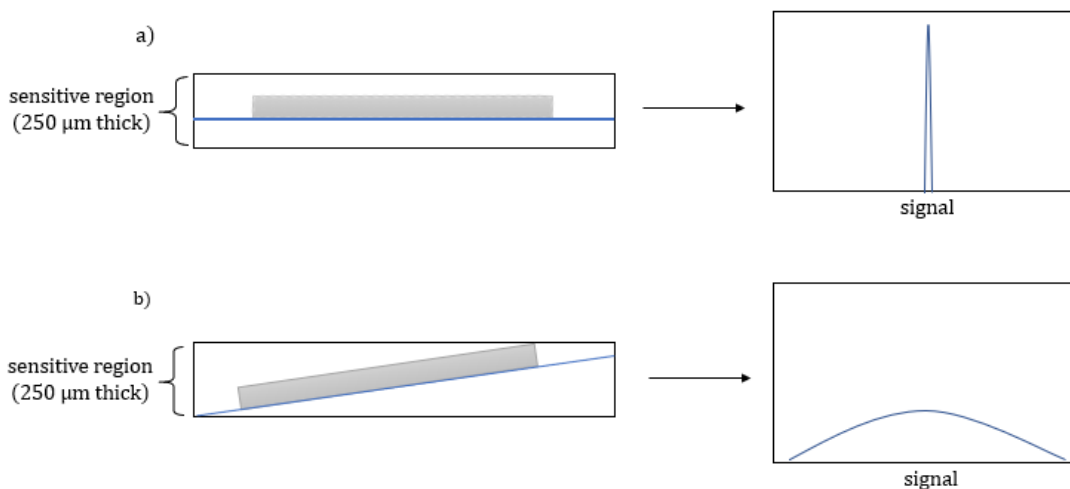
Figure 15: A diagram illustrating the effect of a tilted epoxy sample on signal acquisition. The left box in a) represents a coplanar epoxy sample (grey) cast onto a substrate (blue line) within the sensitive region of the rf coil that is 250 μm thick. The right box in a) represents the maximum signal obtained from probing that region of the sample, which has a very sharp peak. The left box in b) represents the same epoxy sample but tilted with respect to the sensitive region of the rf coil. The right box in b) represents the maximum signal obtained from probing that region of the tilted sample, which has a shorter and blurred out peak. This tilt in the sample reduces the spatial resolution.

All in all, for measurements using the PM5, an interplay of the various conditions discussed above influence the final spatial resolution for each individual experiment. The spatial resolution can be refined as low as sub-10 microns, with special consideration of experiment parameters, and as high as 200 microns without any consideration. Tilting of the samples aside (which needs to be addressed separately for each sample), we have optimized our experimental parameters for measurement of epoxies—in general, our spatial resolution is as good as 20 um unless otherwise stated.

Chapter 5: Surface Energy and Adhesion Strength

Using epoxy resins in adhesive bonding applications is notable in aerospace engineering for aircraft construction because of its numerous advantages over other joining methods.[85,86] Measuring the adhesion strength between a mechanical bond formed by an epoxy resin and a substrate is often done by performing various adhesion tests, including lap shear tests and pull off tests, which measure the amount of force required to pull the two materials apart.[87–89] However, these adhesion tests are thermodynamically irreversible, which means they are completely destructive to samples, and therefore inevitably expensive when performing such tests on aerospace applications, like aircraft wings. Using a non-destructive technique that can measure the strength of adhesion between an epoxy resin and a substrate will greatly reduce costs in aerospace manufacturing.

The interface and interphase regions have been widely studied when determining the strength of adhesion or quality of an adhesive bond between two materials.[90–92] The interface is the physical boundary between two different layers of microstructure or chemistry whereas the interphase describes the actual volume of material at the interfacial region that has chemical interactions and properties different from the surrounding bulk materials.[93] The molecular interactions, polymer chain mobility, and degree of crosslinking are different at the interface than in the bulk of the epoxy resin and therefore play an important role in determining the final properties of the bonded material, like its adhesion strength.[94] More specifically, the interface facilitates stress transfer between the resin and the substrate, which include stresses caused by differences in thermal expansion of the two materials, environmental degradation, water absorption, shear stress,

compression and tension.[95] Interfacial defects during bonding (curing of an epoxy resin to a substrate) or in service can also be a form of stress that leads to premature failure. Thus, it is important to be able to characterize the interface between two bonded materials in order to assess the mechanical strength and quality control.

Adhesive forces are related to the molecular interactions between two materials in an interphase. These interactions can be related to the surface free energy (γ), which is the measure of excess energy at the surface of a material, and is often used to describe adhesion between two materials.[96–99] The surface energy of a solid substrate helps predict how a liquid will behave when in contact with the surface of the substrate. The greater the strength of molecular interactions of the bulk material in a solid substrate, the higher the surface energy of that substrate. Moreover, the higher the surface energy of a substrate, the more the liquid will spread across the surface, thus possessing good adhesive behavior. The correlation between surface free energy and adhesion strength can be useful in assessing the quality of an adhesive bond, however it proves challenging to probe the surface energy of a substrate that has already been cast with an epoxy resin and cured.

Only recently has NMR relaxometry been correlated with surface energy.[100,101] Research performed by D'Agostino et.al.[101] included a theoretical analysis on the relationship between T_1/T_2 data and the strength of surface interaction of water with various oxide surfaces. The ratio of NMR relaxation times relaxation times, $-T_2/T_1$, was determined proportional to surface energy[101] therefore,

$$-\frac{1}{E} \propto \frac{T_1}{T_2}$$
(5.1)

where E is surface energy and T_1 and T_2 are the spin-lattice and spin-spin relaxation times, respectively. Because the proportionality between the surface energy and the T_1/T_2 ratio of liquid-solid interactions were based on qualitative results (no changes in surface energies were quantified; only correlations were seen),[101] it is expected that quantitative agreement of measurements may not be considerable. However, the correlation between surface energy and the T_1/T_2 ratios allows for the interpretation of NMR relaxation data in characterizing and assessing adhesion of materials to a substrate with relatively reliable trends.

Surface treatments of substrates can strongly influence the properties of the interphase as they form during curing and undergo changes under mechanical effects in service. Surface treatments can influence bond strength between an adhesive and substrate by altering the substrate surface in a number of ways including changing surface chemistry, surface abrasion, and chemical etching.[102] These treatments can strengthen the interactions between an epoxy resin and a substrate at the interface by reducing polymer mobility on a molecular level. In contrast, the presence of defects in the interfacial region, including macroscopic voids and disbonds within the epoxy resin, can increase the polymer chain mobility at the interface, degrading the adhesive strength between two materials.[102,103]

The molecular mobility of polymer chains at a polymer-inorganic interface can be measured using NMR relaxation times, T_1 and T_2, which can be related to the surface energy (Eq. 5.1) and correlated with the adhesion strength between two materials.

Therefore, this chapter concerns itself with our development of single-sided NMR as a nondestructive tool for assessing the quality of an adhesive bond between an epoxy resin and a substrate as well as the evaluation of local defects and degradation phenomena in the interfacial region. T_1–T_2 measurements were performed on surface treated epoxy samples and correlated with surface free energy to characterize the strength of an adhesive bond between an epoxy resin and a substrate.

5.1 Sample Preparation

Samples were made using Epon 825 (Hexion; Columbus, OH), a high purity bisphenol A epichlorohydrin liquid epoxy with an equivalent weight of 175-180 g/eq per epoxide. The curing agent used was Jeffamine® D-230 (Huntsman; The Woodlands, TX) which is a polyetheramine, aliphatic diamine curing agent. Jeffamine® D-230 is a primary amine with an average molecular weight of 230 g/mol and an amine hydrogen equivalent weight (AHEW) of 60 g/eq. Alumina plates (11.25 x 11.25 x 0.1 cm; McMaster-Carr) were used as the inorganic substrates.

The surface treated samples used in this thesis were prepared at Metna Corporation in Lansing, Michigan by collaborators Anagi Balachandra and Nastaran Abdol. After cleaning the alumina plates by sonication in a solvent, either ethanol or isopropanol, and allowed to air dry, they were exposed to a source of UV-ozone for one hour. The UV-ozone exposure was to increase the density of hydroxyl groups on the alumina substrate. After substrates were cleaned, some alumina plates were treated with various materials to alter their surface energy. Two different silane surface treatments were used, including a silane-amine, (3-trimethoxysilylpropyl)diethylenetriamine

(Gelest), and a fluoro-silane, tridecafluoro-1,1,2,2-tetrahydrooctyl-1-triethoxysilane (Gelest). Then, the UV-ozone cleaned alumina substrates were immersed in 2 wt.% respective silane solution in either ethanol or isopropanol for 20 minutes. Other surface treatments used in this study included Vydax (DuPont™ Vydax NRT 960 Dry Film Lubricant) and Teflon (DuPont™ Non-Stick Dry Film Lubricant with Teflon), which were prepared in a similar way.

After drying the surface treatments, high temperature vacuum bag sealant tape (Air Products; Allentown, PA) was placed on all four edges of the alumina plates leaving an open area of ~10 × 10 cm for epoxy casting. Edges were further secured with Kapton tape (McMaster-Carr) to prevent leaking of epoxy during casting or curing. Epon 825 and Jeffamine® D-230 were mixed in a 100% resin-to-hardener stoichiometric ratio. The blend of resin and hardener was cast on surface treated and untreated (control) alumina plates and degassed under vacuum for 5-10 minutes. Curing was performed at 80°C for 2 hours and then at 120°C for 3 hours.

5.2 Single-Sided NMR Measurements

Prior to performing simultaneous T_1–T_2 measurements, signal intensity profile experiments were run to determine the location of the epoxy/substrate interface and region of the sample with the greatest signal intensity. To obtain a profile of each surface treated sample, CPMG measurements were collected at 100 μm intervals using a 44 μs echo time, 256 scans, 32 echoes, and a repetition time of 300 ms. One spacer was removed from the PM5 to increase the maximum depth and measure throughout the entire thickness of each sample. Profile data for a fluoro-silane treated sample (Sample

ID 235) can be seen in **Figure 16** with complete parameters located in **Appendix A**. The

plot on the left of **Figure 16** shows the echo decay of the CPMG experiment within the

profile, although in this figure only noise is shown corresponding to the last CPMG

measurement that was collected (which happened to be below the epoxy at 0 μm where

no signal was detected). The plot on the right of **Figure 16** is the profile plot that displays

the signal amplitude at each position (depth) within the sample. The epoxy can be seen in

the region of the greatest signal amplitude, between 1500 and 500 μm depth, with the

epoxy/air interface located at approximately 1500 μm depth and the epoxy/substrate

interface located at approximately 500 μm depth. Note: the depth axis from left-to-right

corresponds to a bottom-to-top orientation of the sample.
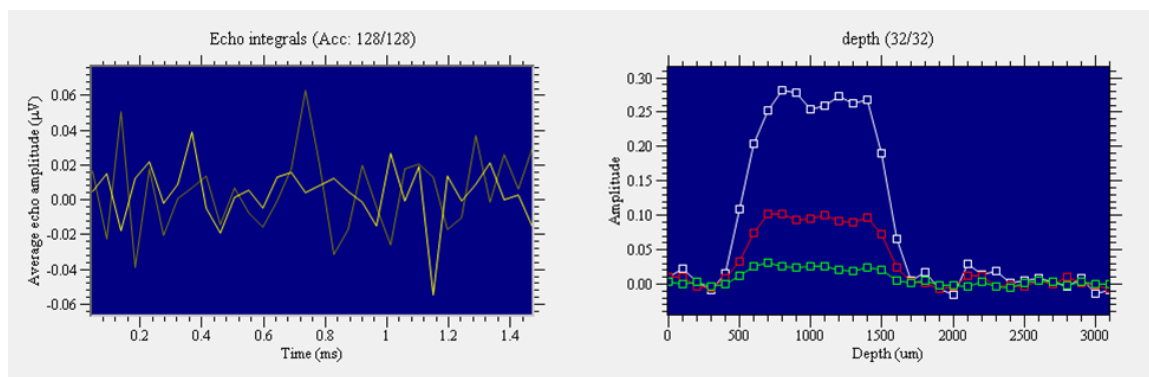
Figure 16: Profile of fluoro-silane treated sample (Sample ID 235) as produced by the
Prospa software (Magritek). The plot on the left shows the echo decay of the CPMG
experiment within the profile (only noise shown here) and the plot on the right is the
profile plot that displays the signal amplitude at each depth within the sample. With only
one spacer on the magnet, the maximum depth the sensitive region can probe is 3100 μm.
The right-most point on the x–axis (3100 μm) is the position of the magnet when it is at
"home", which in this case happens to be located above the sample itself, so no signal is
detected. The profile experiment began at the "home" position and the mechanical lift
moved the magnet down in increments of 100 μm and performed CPMG experiments at
each depth. For this sample, the epoxy is ~1000 μm thick with the air/epoxy interface
located at ~1500 μm and the epoxy/substrate interface located at ~500 μm. Above the
epoxy region (>1700 μm) is noise from the air above the sample. Below the epoxy region
(<400 μm) the signal from the epoxy decreases to zero as the sensitive region of the
magnet moves into the alumina, where there is no measurable ^{1}H NMR signal.

Each sample has a slightly different epoxy thickness, so prior to every T_1–T_2 measurement of a new sample a profile experiment was performed to determine the location of the epoxy/substrate interface. Also, if a sample was moved laterally while on top of the PM5, a profile experiment was re-run to account for micrometer-scale variances of epoxy thickness and surface treatments throughout a sample in the x-y plane.

Once the thickness of the epoxy sample and location of interfaces were determined, the mechanical lift was used to move the sensitive region of the rf coil to the epoxy/substrate interface. A standard CPMG experiment was then performed at the interface with an echo time of 44 μs, 1024 scans, 16 complex points, and a 300 ms repetition time, with complete CPMG experiment parameters for a Epon 825 and Jeffamine® D-230 epoxy sample in **Appendix A**. This was done, using the Prospa software, to ensure that the CPMG parameters used allowed the echo train to decay to zero amplitude to capture the full T_2 relaxation time. Then, a Fourier transformation of the CPMG experiment at the interface would ensure proper positioning of the magnet by producing data in a spatially resolved frequency domain. **Figure 17** shows a Fourier transformation of the first echo from a CPMG experiment at the epoxy/substrate interface of a fluoro-silane treated sample with the signal intensity plotted against spatial position (Sample ID 235).
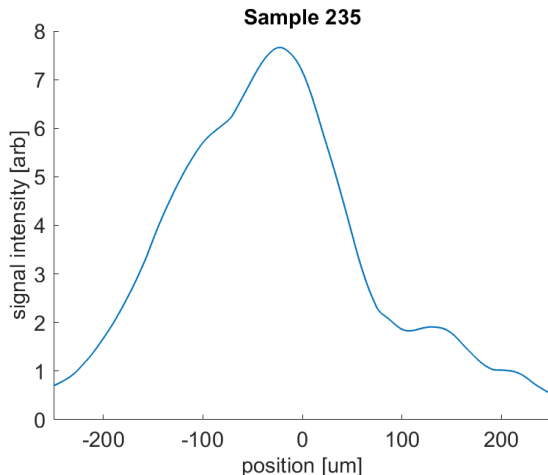
Figure 17: Fourier transformation of the echo train decay from a CPMG experiment at the epoxy/substrate interface of a fluoro-silane treated sample (Sample ID 235). The signal intensity within the sensitive region is plotted against the spatial position. The zero position is located at the center of the sensitive region of the rf coil. The positive positions correspond to moving closer to the magnet whereas the negative positions are farther away from the magnet. The epoxy region is located to the left of the zero position. The decrease in slope between 0 and +100 μm is the interphase? region wherein the signal from the epoxy decreases to zero as the sensitive region of the magnet moves into the alumina (no ^{1}H NMR signal). The decrease in slope on the left side of the plot corresponds to losing NMR signal due to signal extending beyond the range of the sensitive region.

After the spatial position of the epoxy/substrate interface was determined, a saturation recovery experiment was performed. Saturation recovery experiments were run at the epoxy/substrate interface of each sample to determine the estimated T_1 relaxation time in the interfacial region using the Prospa software. The experiment was performed with an echo time of 26 μs, 1024 scans, 11 T_1 points and an initial T_1 estimation of 100 ms with a maximum recovery time of 500 ms ($5{\times}T_1$ estimation). Full parameters can be seen in **Appendix A**. This experiment was repeated until the T_1 estimation equaled the T_1 value of the epoxy/substrate interface at that position, indicated by the decrease in uncertainty values from the Prospa software T_1 fit output.

Once the T_1 relaxation time was determined, spatially resolved T_1–T_2 measurements were performed. The parameters from the individual saturation recovery and CPMG measurements above were used to set up the T_1–T_2 experiment to ensure that the measurement would properly capture the relaxation decays in both dimensions with a high enough SNR for reliable signal acquisition and data processing. A T_1 relaxation time of 115 ms for Epon 825 and Jeffamine® D-230 epoxy samples, determined from the saturation recovery experiment, was used with a maximum recovery time of 375 ms ($5\times T_1$). An echo time of 44 μs and 32 echoes were used to achieve a full baseline decay of epoxy signal (determined from the CPMG measurement). A total of 17 T_1 points and 1024 scans were initially used for each T_1–T_2 measurement to try and maximize SNR without prolonging experiment time. These initial T_1–T_2 experiments took approximately 2 hours for one complete measurement at the epoxy/substrate interface

All the procedures discussed above were repeated for each sample prior to performing T_1–T_2 measurements. T_1–T_2 measurements performed on surface treated samples were adjusted to capture different spatial regions (throughout the entire thickness of the sample, the air/epoxy interface, the epoxy/substrate interface) and to maximize SNR at the epoxy/substrate region ranging from sample measurements of a few hours all the way to 36 hours depending on experiment parameters (noted for each measurement in section 5.4).

5.3 Data Processing

Single-sided NMR T_1–T_2 data were processed using MATLAB scripts (MathWorks Inc.; Natick, MA) developed in our lab by Dr. Tyler Meldrum. Within the

script, these data were first processed via Fourier transformation as described previously. The result of this transformation is a series of data sets, one at each spatial position, that contains simultaneous T_1 and T_2 decay information. The T_1 and T_2 data sets were then individually subjected to a 2D ILT resulting in a distribution of T_1 and T_2 relaxation times at each spatial position. The ratio of relaxation times, T_1/T_2, were extracted at various positions throughout the thickness of the epoxy samples and correlated with surface free energy.

A secondary data processing method, known as the Matrix Pencil (MP),[104,105] was used to extract T_1–T_2 data as an alternative method to the ILT. The MP reduces the size of the data using singular value decomposition then solves the reduced set of matrices as an eigenvalue problem. From that, relaxation times can be obtained as a scalar solution.[104,105] The MP is a novel processing method of NMR data with advantages including a faster processing speed than ILT and no required smoothing constraints. However, MP has not been as widely implemented in analyses of NMR relaxation data like ILT has, therefore its quality is unknown. In the context of this thesis, the MP was only used for some T_1–T_2 data processing of surface treated samples as a supplemental method to test its agreement with the ILT. The MP was implemented in the MATLAB script, along with ILT, created by Dr. Tyler Meldrum.

5.4 Results and Discussion

5.4.1 Preliminary T_1–T_2 measurements at the epoxy/substrate interface

T_1/T_2 data at the epoxy/substrate interface of Epon 825 and Jeffamine® D-230 and alumina surfaces treated with silane-amine, fluoro-silane, Teflon and Vydax were

investigated and compared to T_1/T_2 of an untreated control sample (**Figures 18-22**). The mean-log T_1/T_2 values (the mean-log of each parameter taken separately) and signal intensities were plotted with respect to position. The mean-logT_1/mean-logT_2 values were calculated in the MATLAB script by multiplying the log of the T_1 and T_2 ILT data distributions individually by their respective amplitudes and dividing by the sum of those distribution amplitudes. The mean-log calculations are weighted by the T_1 and T_2 data points with the highest amplitudes and therefore give the maximum value of the individual T_1 and T_2 ILT peaks (center slice of the peaks).

The red line in each figure (**Figures 18-22)** represents the signal intensity and the blue line represents the T_1/T_2, both versus position. In the x-axis of these figures, going towards negative values of z indicates moving away from the alumina/substrate interface (into the epoxy). Negative z implies lower frequency and farther away from the magnet, whereas positive z implies higher frequencies and closer towards the magnet. The actual epoxy/substrate interface is located approximately around +50 μm in these figures. The ratio of T_1/T_2 of bulk Epon 825 and Jeffamine® D-230 was approximately 211 (arb). This was determined from the T_1 relaxation time measured by a saturation recovery experiment and the T_2 relaxation time measured by a CPMG experiment in the bulk epoxy. The horizontal black line in these figures was used to visualize the T_1/T_2 ratio of bulk epoxy. Any data below the horizontal black line positioned at a T_1/T_2 of 1 (arb) is unreliable because the data is fundamentally limited by the fact that $T_1 \geq T_2$.
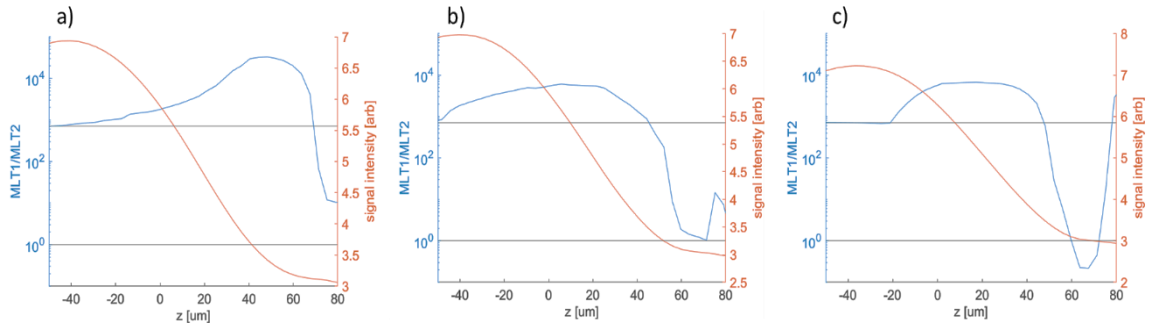
Figure 18: T_1–T_2 data of Sample ID 235, fluoro-silane treated, for replicate measurements (a), (b) and (c).
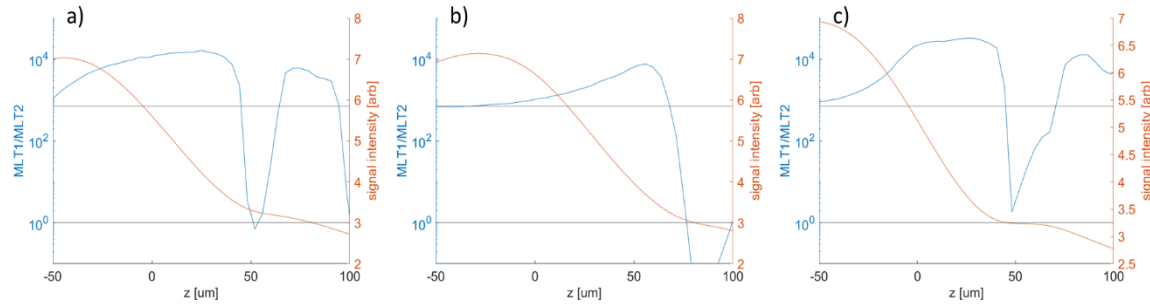
Figure 19: T_1–T_2 data of Sample ID 231, silane-amine treated, for replicate measurements (a), (b) and (c).
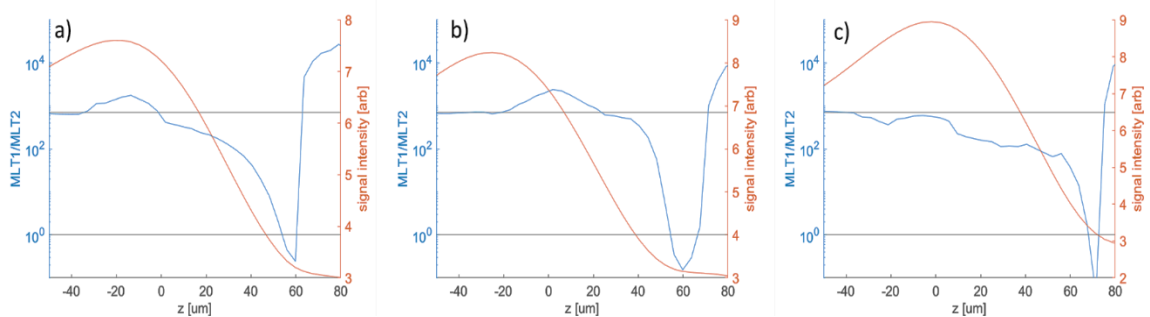
Figure 20: T_1–T_2 data of Sample ID 292, Teflon treated, for replicate measurements (a), (b) and (c).
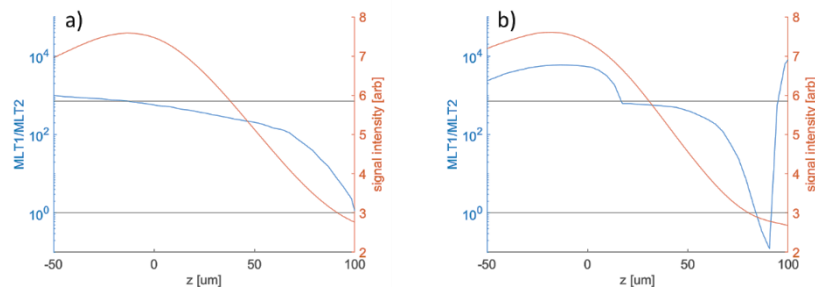
Figure 21: T_1–T_2 data of Sample ID 294, Vydax treated, for replicate measurements (a) and (b).
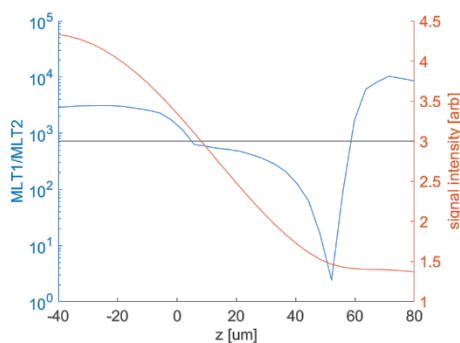
Figure 22: T_1–T_2 data of Sample ID 175, untreated control, for only one measurement.

The left side of **Figures 18-22**, where the signal intensity is the highest, is the epoxy signal located above the interfacial region. Considering that the ratio of T_1/T_2 in bulk epoxy was 211 (arb), we expected that the measured T_1/T_2 ratio above the interface of each surface treated sample (the far left side of **Figures 18-22**) would track consistently around 211 (arb) and eventually decrease where the alumina plate was located. The silane-amine treated sample in **Figure 19** represents this relatively well where the T_1/T_2 ratio starts at around 211 (arb) in the bulk epoxy region and increases closer to the epoxy/substrate interface at around +50 µm.

On the other hand, in **Figure 20**, the T_1/T_2 appears to decrease at the interface of the Teflon treated sample (around +40 µm). An increase in the T_1/T_2 ratio would indicate an increase in the surface energy of the sample, as indicated by Eq 5.1. Therefore, a higher T_1/T_2 ratio at the epoxy/substrate interface indicates a stronger interaction with the substrate surface. The Teflon surface treatment causes the substrate surface to become more hydrophobic and therefore would lower the surface energy. This was tested by mechanical adhesion strength tests (pull of tests) performed by Dr. Anagi Balachandra (Metna Co) where Teflon treated samples showed pull of strengths of 1.6 MPa which were 15 times lower than the pull off strengths of untreated samples (24 MPa). Thus, the decrease in the T_1/T_2 ratio at the epoxy/substrate interface for the Teflon treated sample (**Figure 20**) is in agreement with the lower surface energy of that sample. On the other hand, the silane-amine surface treatment creates a stronger interaction between the epoxy and substrate by acting as a covalent layer between the alumina substrate and the reactive groups of the epoxy resin.[106] The manifestation of a higher T_1/T_2 ratio at the epoxy/substrate interface of the silane-amine treated sample is a result from the stronger interaction between the surface treated substrate and the epoxy due to the higher surface energy (as seen in **Figure 19**).

These trends seemed promising for correlations of T_1/T_2 ratios with surface energies, however, the SNR of these data were too low to draw any definite conclusions. The SNR at the epoxy/substrate interface region reached a maximum of about 7 for the surface treated samples. It was determined in our lab by simulations of T_1-T_2 NMR data with various noise levels, performed by John Cacciatore and Dr. Tyler Meldrum, that an SNR on the order of 20 to 30 is needed to reach 90% of the simulations within 10% of

the actual T_1 and T_2 values. These SNR thresholds are needed for good accuracy of T_1-T_2 data, which is 3 to 4 times larger than the SNR values obtained in the preliminary T_1-T_2 measurements. To acquire data with an SNR that is 3 to 4 times larger would require 10 to 15 times longer acquisition times. Increasing the number of scans by 10 times, though, is not practical. However, multiple replicates could be measured to try to mitigate the smaller SNR values in the epoxy/substrate regions that have low signal magnitudes.

Therefore, further refining of the T_1–T_2 measurements was performed to measure data with higher SNR and more reliable results. It is important to note that the increase in T_1/T_2 ratio below the interface for some of these samples where the signal intensity has gone to zero, greater than +60 μm in **Figure 19** for example, is most likely caused from ILT overfitting the noise in the alumina region.

5.4.2 T_1–T_2 measurements throughout the entire thickness of surface treated samples

In order to further determine changes in surface energy of the surface treated samples, T_1–T_2 lift experiments were performed in which a spatially resolved 2D T_1–T_2 experiment was conducted at each position throughout the entire thickness of the sample, capturing both the air/epoxy and epoxy/substrate interfaces. The entire thickness of each sample was measured using a T_1–T_2 lift experiment to ensure that differences in the T_1/T_2 ratio throughout the thickness of the sample, and at the interfaces, could be differentiated. Measuring the air/epoxy interface for all the samples allowed for comparison of their T_1/T_2 ratios, which theoretically should be the same in that region considering they are made of the same bulk epoxy material.

The T_1–T_2 lift experiments began slightly above the air/epoxy interface. Between measurements, the mechanical lift holding the PM5 magnet was moved down by 250 μm at which point the measurement was repeated. This process was followed until the entire thickness of the sample was measured. The T_1–T_2 lift experiments were repeated for each surface treated sample for a total of two replicate measurements. Parameters for the T_1–T_2 lift experiments were the same as previous T_1–T_2 measurements, except for the added lift movement, which increased the total measurement time to about 36 hours. Representative data for one of the surface treated samples, Sample ID 231 silane-amine treated, can be seen in **Figure 23**. The x-axis of this figure goes (from left to right) from above the air/epoxy interface of the samples to below the epoxy/substrate interface; in other words, reading the x-axis from left-to-right corresponds to moving downwards through the sample. The y-axis shows the T_1/T_2 ratio throughout a sample processed using both the matrix pencil method (MP, black) and by inverse Laplace transformation (ILT, red).
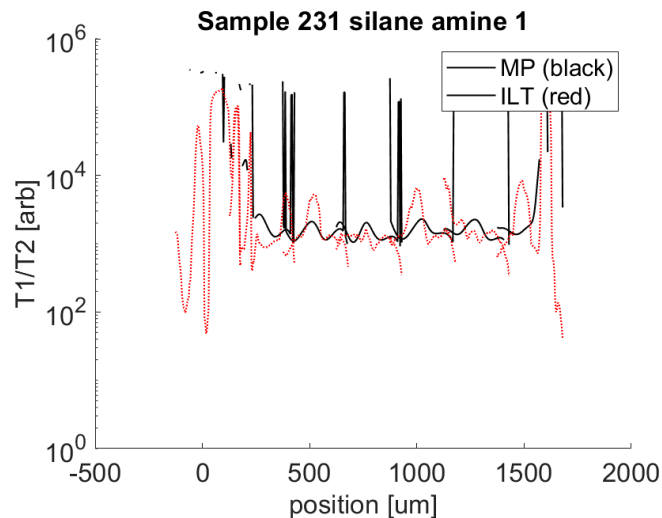
Figure 23: T_1–T_2 of Sample ID 231 (silane amine treated) replicate 1. The experiment started at -1100 μm from "home" and ended at -2850 μm from "home", for a total of 7 measurements.

Although lengthy, about 33–36 hours per replicate measurement for each sample, these data showed that T_1–T_2 distributions could be reliably measured across entire thicknesses of samples. The bulk epoxy in **Figure 23** can be seen from about +250 to +1500 μm, which varied from sample to sample depending on the exact thicknesses of the epoxy at that position of the sample. The sharp vertical spikes in the black (MP) data are related to infinite T_1 or zero T_2 values, which is a property of the processing algorithm that is still under investigation. However, the general agreement between the ILT and MP processing methods suggests that the observed T_1/T_2 ratios from these T_1–T_2 lift experiments are accurate and representative of the data. The "humps" seen throughout the bulk epoxy region are likely caused by the spatial inhomogeneity of the rf fields pulse sequence calibration for the center of the sensitive volume. Spins that are slightly off center will experience rotations that are not exactly 90° or 180° thus resulting in imperfect measurements of T_1 and T_2.

Because the surface treated samples were all made with the same epoxy resin, these T_1–T_2 lift experiments offered standards of reference amongst the samples—such that the T_1/T_2 ratio of both the air/epoxy interface and the bulk epoxy regions of the samples should be consistent with one another. Specifically, the silane-amine treated sample (seen in **Figure 23**) appeared to have a different T_1/T_2 ratio at the epoxy/substrate interface than the air/epoxy interface. The data in the air/epoxy region, located around 250 μm in **Figure 23**, did not reach as high of a T_1/T_2 value as in the epoxy/substrate region, located around 1600 μm, for the silane treated sample. This suggests an increase in surface energy near the alumina substrate, which was expected because of the silane-

amine treatment acts as a covalent layer between the epoxy and substrate. On the other

hand, the other surface treatment samples did not show very clear results and proved the

need for a systematic method of quantifying changes in T_1/T_2 ratios to compare results

between each sample. All in all, the T_1–T_2 lift experiments provided an approach to

measuring thicknesses of epoxy samples, reliable internal controls, and a method to

assess changes in surface energies.

The T_1/T_2 ratios from the T_1–T_2 lift experiments were calculated using the mean-

log T_1 or T_2 values (from an ILT distribution) or by choosing only one component from a

matrix pencil processing method (which would produce a similar result). This method for

calculating the T_1/T_2 distributions was not ideal because it neglected the possibility of

multiple relaxation components in particular spatial regions. In other words, if the spatial

region had more than one relaxation component, the mean-log values would not capture

that. For example, a spatial region in a sample could have multiple relaxation components

if the sensitive region is probing the interfacial region between the alumina substrate and

epoxy resin where epoxy molecules are less mobile and restricted closer to the substrate

as opposed to the bulk epoxy region. Therefore, the bulk region of the epoxy would have

a larger T_2 relaxation time than in the interphase. Because of this, the data processing

method was further refined to show spatially resolved data (an example is shown in

Figure 24 for Sample ID 231). The top row in **Figure 24** displays the full T_2 data, T_1

data, and the T_1/T_2 ratio from left to right. The bottom row displays the signal intensities

of T_1 and T_2 values as well as a T_1–T_2 map at a specific depth in the sample indicated by

the dotted line (in this case a depth of 455 µm). Only one relaxation component was seen

for both T_2 and T_1 data (bottom left and middle panels) throughout the thickness of each

sample. These data verified that, at many randomly selected positions, the initial

processing method used in **Figure 23** was appropriate.
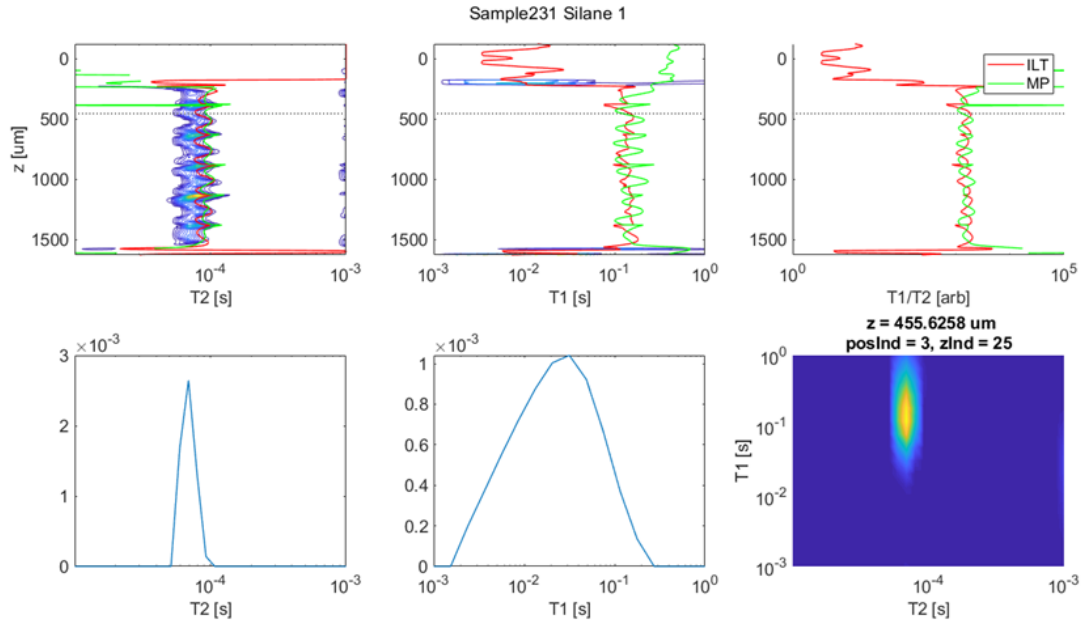
Figure 24: T_1 and T_2 data of Sample 231 (silane amine treated) replicate 1 showing position vs T_2 (s) (top-left), position vs T_1 (s) (top-middle), and position vs T_1–T_2 (top-right). This replicate was measured with a total of 7 lift positions starting slightly above the air/epoxy interface. Epoxy signal can be seen between 300-1500 μm. The signal intensities of the T_1 and T_2 values at a depth of 455 μm (indicated by the black dotted line in the top panels) can be seen in the bottom left and middle panels respectively, as well as a T_1–T_2 map at that position in the bottom-right panel.

5.4.3 Pseudo-statistical approach to quantifying changes in T_1/T_2 data

For the purpose of quantifying changes in surface energies measured from the T_1–T_2 lift experiments, a pseudo-statistical approach was used to identify the interfacial regions of the surface treated samples. A MATLAB script (made by Dr. Tyler Meldrum) was made to use the processed data from the T_1–T_2 lift experiments and extrapolate the slopes of three different regions on the T_1/T_2 vs position (µm) graphs for each surface treated sample (**Figure 25**). We presumed that each measurement throughout the entire thickness of an epoxy sample consists of three segments. The three segments of interest were the air/epoxy interface (Segment 1), bulk epoxy (Segment 2), and the epoxy/alumina interface (Segment 3). Using the MATLAB script, several users independently chose points on each graph to obtain four different x-values. The region between points 1 and 2 represented the air/epoxy interface, between points 2 and 3 represented the bulk epoxy, and between points 3 and 4 represented the epoxy/substrate interface. From these x-values, the spatial extent and slope (T_1/T_2 per µm) of each region was determined for each sample, as well as the T_1/T_2 ratio of their bulk epoxy regions. This process was repeated 10 times to obtain minimum, maximum, median, and average values for each region. The results for all the surface treated samples can be found in **Table 5.5-5.7** of **Appendix B**.
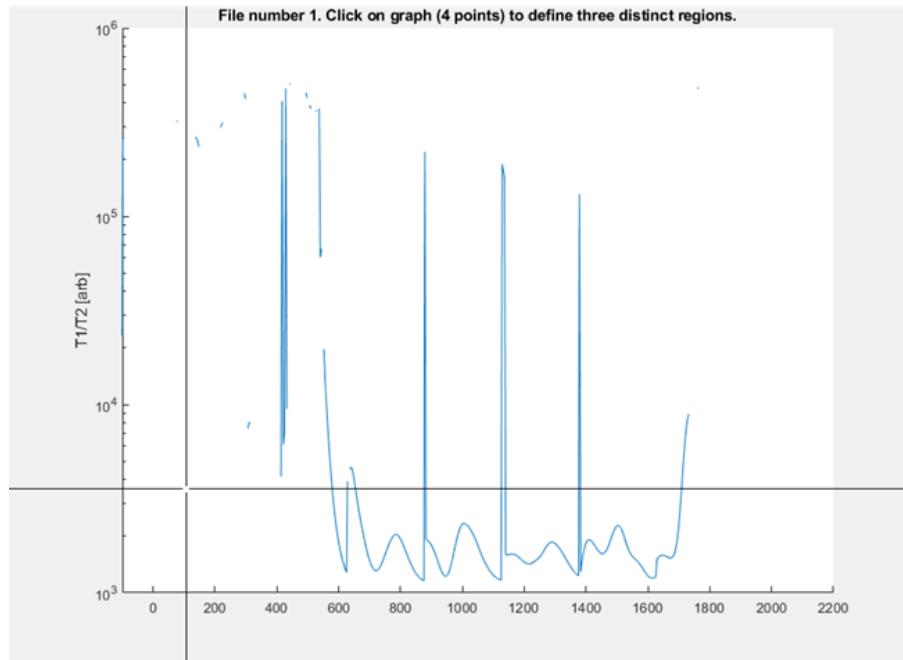
Figure 25: T_1/T_2 vs position (μm) graph for Sample ID 231 (silane amine treated) where the cursor (black cross) was used to select points on the blue T_1/T_2 lines to designate the air/epoxy (~500-600 μm), bulk epoxy (~700-1600 μm), and epoxy/substrate (~1700-1800 μm) regions. The x-ranges for each region were then used to determine the spatial extent and slopes (T_1/T_2 per μm) of each region along with the T_1/T_2 ratio in the bulk epoxy region.

The pseudo-statistical approach to quantifying changes in surface energies suggested that the thicknesses of bulk epoxy regions were similar for the same surface treatment samples, though this is not the most optimized method of characterizing thicknesses of regions within epoxy samples due to the random point-picking on the plots (seen in **Table 5.5** of **Appendix B**). Additionally, the T_1/T_2 ratio for bulk epoxy was consistent across all samples, at approximately 1500 (**Table 5.7** in **Appendix B**). The T_1/T_2 ratio as a function of position in the bulk epoxy was also consistent for all samples indicating a homogenous region of bulk epoxy (**Table 5.6** of **Appendix B**). These results suggested consistent regions of bulk epoxy amongst the samples, which was as expected considering they were made of the same epoxy resin.

61

The change in the T_1/T_2 ratio as a function of position, measured by the slope, in the air/epoxy interphase was not consistent across samples, which could be caused by uneven surfaces at the air interface for each sample or tilted samples with respect to the rf coil. To test this, the uneven surfaces could potentially be measured experimentally by a scanning electron microscope to obtain the surface topography of each sample. An apparatus would be needed to address the tilt of the sample with respect to the rf coil that could monitor the leveling of each epoxy sample on top of the magnet.

The spatial extent of the air/epoxy interphase was more consistent (approximately 90 ± 20 µm) across all the samples than their respective epoxy/substrate interphases. Particularly, the untreated and silane-amine treated samples had a measured epoxy/substrate interphase thickness of around 90 µm $\pm$ 20 µm whereas the Teflon and Vydax treated samples had a lower interphase thickness, approximately 50–60 µm $\pm$ 15–20 µm (see **Table 5.5** of **Appendix B**). The smaller epoxy/substrate interphase thickness seen in the Teflon and Vydax surface treatment samples may indicate fewer molecular interactions in the interphase region as the epoxy has a slower diffusion or penetration into the hydrophobic Teflon and Vydax treatments, leading to a weaker adhesion to the substrate. This is because greater chemical adhesion to a substrate increases the amount of epoxy molecules that interact with the surface of the substrate, as well as the strength of those interactions, thus propagating a more rigid network into the bulk epoxy. Therefore, a thicker interphase region measured in the samples with a higher chemical adhesion (untreated and silane-amine treated samples) was in agreement with our expectations based on the surface treatment effects.

Data for both the interphase thicknesses and interphase slopes indicated that surface treated samples with a decreased chemical adhesion, Teflon and Vydax samples, are distinguishable from surface treated samples that have an increased chemical adhesion, untreated and silane-amine samples. These results are congruent with those measured from preliminary mechanical adhesion tests performed by Dr. Anagi Balachandra (Metna Co.), in which both Teflon and Vydax treated samples, on average, had pull of strengths that were 15 times lower than untreated alumina samples. The pseudo-statistical approach remains imperfect, though, as it was a subjective way of quantifying surface energies. More replicate measurements of the surface treated samples and more users for point-picking data could provide reliable results for a real-statistical approach as opposed to a pseudo-statistical one. Also, the results for the fluoro-silane treated sample were inconsistent which indicated a need for more measurements or more reliable T_1/T_2 data from the T_1–T_2 lift experiments. All in all, the pseudo-statistical approach provided interesting data on interphase thickness and T_1/T_2 slopes that were in agreement with the chemical adhesion of epoxy to substrates with various surface treatments. The T_1/T_2 ratio of bulk epoxy was consistent amongst the surface treated samples and therefore allowed for a focus on only the air/epoxy and epoxy/substrate interfaces in future measurements.

5.4.4 T_1–T_2 measurements at the air/epoxy and epoxy/substrate interfaces of a surface treated sample

Further investigations focused on increasing the SNR of the T_1–T_2 lift measurements at the interfaces for the fluoro-silane treated alumina sample for comparison with an untreated alumina control sample. The fluoro-silane treated sample was of interest because, compared to the silane-amine surface treatment, it has a lower surface energy due to the hydrophobicity of the fluorinated silane treatment. Because of the large difference in surface energy between the fluoro-silane treated sample and untreated alumina sample, we expected to see a noticeable difference in the T_1/T_2 ratio at the epoxy/substrate interfaces.

It is important to note that the Vydax and Teflon surface treated samples were not investigated further, despite that they showed reliable differences in the T_1/T_2 data from the pseudo-statistical quantification of surface energies that indicated a lower chemical adhesion. This is because both epoxy samples had become unadhered from the alumina substrate due to the age of the samples and poor adhesion (as a result of the lower surface energy of the Vydax and Teflon treatments). Therefore, the fluoro-silane treated sample became the focus for investigation of a surface treated sample that is known to have a lower surface energy.

For the T_1–T_2 lift experiments on the fluoro-silane treated alumina sample and control, only the air/epoxy and epoxy/alumina interfaces were measured. Two total lift positions were used to capture both interfaces (one at the air/epoxy interface and one at the epoxy/substrate interface). Eight replicates were considered for both the fluoro-silane treated alumina sample and control sample. The same experiment parameters were used

64

as previous T_1–T_2 experiments (seen in **Appendix A**), however the number of scans and

T_1 points were increased to 1496 and 21, respectively, to increase the SNR of the

measurements.

The rolling averages of the mean and standard deviations of the T_1 /T_2 ratios for

all the replicate measurements of the fluoro-silane treated sample (red) and untreated

alumina sample (blue) can be seen in **Figure 26**. The left column of **Figure 26** represents

the air/epoxy interface and the right column represents the epoxy/substrate interface. The

top rows show the raw T_1/T_2 data with the bottom rows showing the respective rolling

averages (solid lines) and their standard deviation ($\pm$ 1; dotted lines). The fluoro-silane

treated sample appeared to have a T_1/T_2 ratio at the epoxy/substrate interface (right side of

figures) that is lower than that of the untreated control sample (blue). On the other hand,

the control sample had a more consistent range of values for the T_1/T_2 ratio between all

eight replicates.
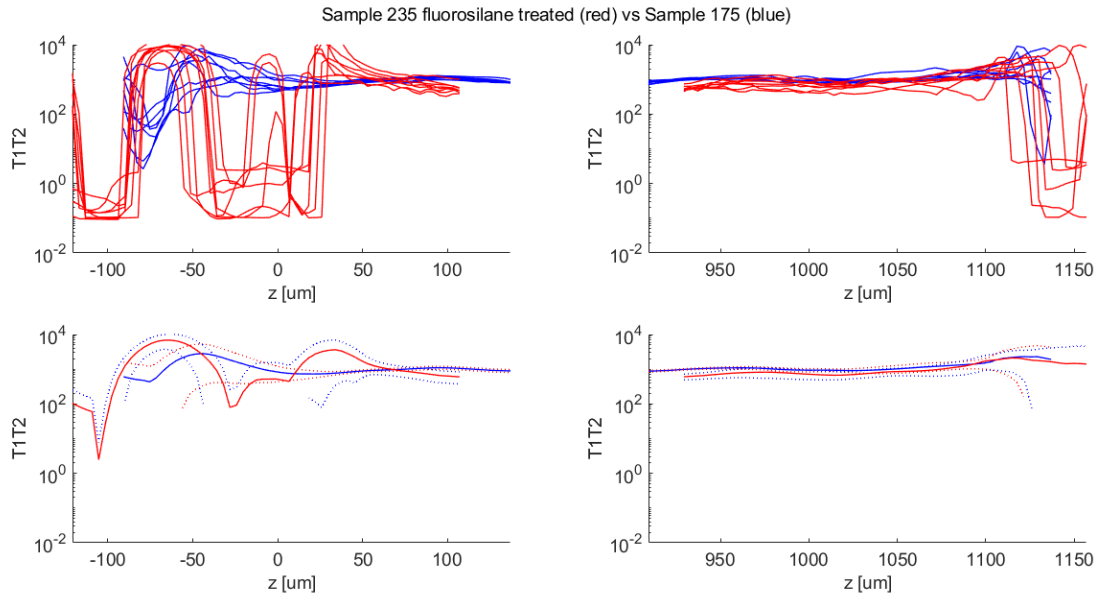
Figure 26: All replicates of T_1–T_2 data of Sample ID 235 (in red) and untreated control Sample ID 175 (in blue) overlaid. The left column is the air/epoxy interface (air to the left), while the right column is the epoxy/substrate interface (substrate to the right). The top row shows the T_1/T_2 ratio for all 8 replicates for each sample type overlaid. The bottom row shows (solid lines) the rolling average (bin size of 7 positions, corresponding to ~27 um) of the mean of the T_1/T_2 ratio across all 8 replicates. The dashed lines indicate +/- one (rolling averaged) standard deviation across the 8 replicates.

The lower T_1/T_2 ratio for the epoxy/substrate interface of the fluoro-silane treated sample indicates a lower surface energy, which is in agreement with the nature of the surface treatment. The T_1–T_2 lift experiments were successful at assessing changes in T_1/T_2 ratios at surface treatment interphases and results proved consistent with expectations of surface energies. However, a need to refine these methods to quantify the differences in T_1/T_2 ratios and better infer differences between surface energies of surface treated samples is prominent.

Drawbacks from the T_1–T_2 lift experiments were noted from the variance in T_1/T_2 data amongst samples as well as the lower SNR from the T_1 measurements. This drawback significantly affected the ability to reliably quantify the differences in T_1/T_2

ratios amongst the surface treated samples. A hypothesis for this arose from the idea that the samples are tilted with respect to the magnet. As discussed in Chapter 4 regarding the spatial resolution of the PM5, samples that are tilted on a micrometer scale can cause large "blurring" effect of the signal, greatly reducing the spatial resolution of measurements. Because of this, the tilt of samples can greatly reduce the ability to reliably quantify changes in T_1/T_2 ratios.

5.4.5 Investigation of a tilted epoxy sample

To investigate the effect of a tilted sample, a layered bulk epoxy sample was made at Metna Corporation (not cast onto a substrate). The top layer consisted of an Epon 825 and Jeffamine® D-2000 epoxy resin and the bottom layer was made of the usual Epon 825 and Jeffamine® D-230 epoxy resin used in the T_1–T_2 experiments. The Jeffamine® D-2000 curing agent is made of a much longer diamine molecule than the Jeffamine® D-230 (see **Figure 27**), which creates a lower crosslink density in the epoxy resin, and thus possesses very different T_1 and T_2 relaxation times. A CPMG profile experiment was measured to determine the location of the interface between the two epoxy resins. As seen in **Figure 28**, the region between 1500 and 3000 μm depth is the top layer, Epon 825 and Jeffamine® D-2000, of the bulk epoxy sample indicated by a higher signal intensity due to its larger T_2 relaxation time. The bottom layer, from 1200 μm depth to 0 μm, is the Epon 825 and Jeffamine® D-230 layer.

H₂N... NH₂ ... CH₃ ... CH₃ ... x ≈ 2.5

H₂N... NH₂ ... CH₃ ... CH₃ ... x ≈ 33.1
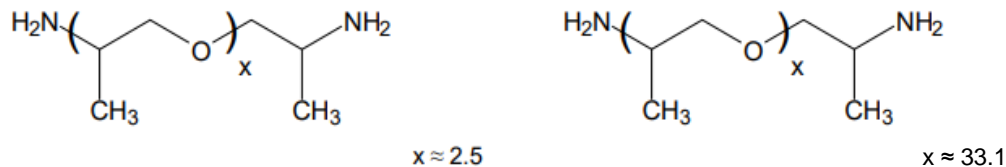
Figure 27: Molecular structure of Jeffamine® D-230 (left) and Jeffamine® D-2000 (right).

The region between the two layers, between 1200 and 1500 μm depth, is the interfacial region. The interface is noticeably tilted with respect to the rf coil in **Figure 28**, as indicated by the slope of the signal amplitude. If the sample was perfectly coplanar with respect to the sensitive volume, then an infinite slope in signal intensity at the interface would be seen, rather than a finite slope. The evidence of tilted samples indicates a limitation on the ability to distinguish small changes in T_1 and T_2 relaxation times of epoxy samples. A T_1–T_2 experiment was performed at the interface of the layered epoxy sample to determine whether or not changes in T_1 and T_2 relaxation times could be distinguished, despite the tilt in the sample (**Figure 28**). The tilt at the interface between 300 and 500 μm is seen in the T_1–T_2 data and although its location is distinguishable, the ability to reliably quantify small changes in T_1–T_2 data to correlate with surface energy is difficult.

An apparatus is currently being engineered in order to eliminate the tilt in the samples on top of the PM5. This apparatus will consist of a triangular plane on a mechanical lift that holds the epoxy samples in place, tilting and lifting them with respect to the magnet. The PM5 will be suspended upside-down above the epoxy samples. In addition to CPMG profiles measuring the depth of the epoxy sample, a tilt profile will also measure the epoxy samples at various tilt angles to find where the sharpest signal is

obtained. A visualization on why this is important was illustrated in **Figure 15** of section 4.1. After the tilt in the samples are mitigated, T_1–T_2 measurements can be repeated on surface treated samples to collect more reliable T_1/T_2 data and better quantify changes in surface energies.
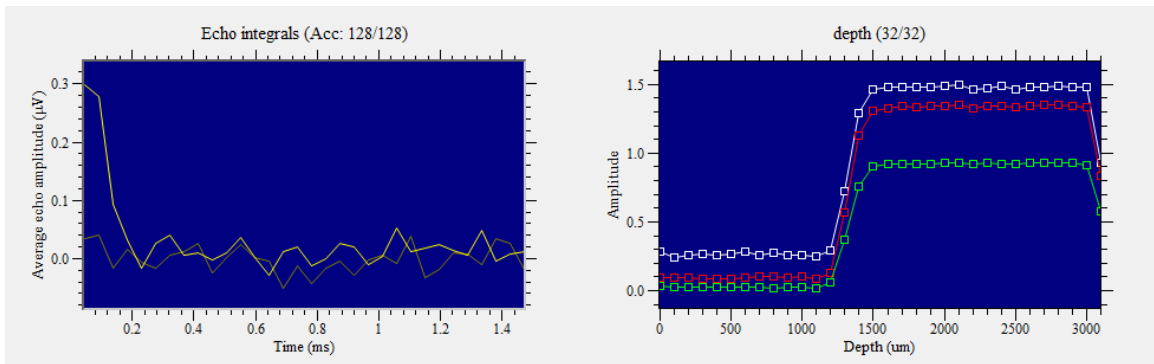
Figure 28: Profile of the Epon 825 and Jeffamine® D-2000 and Epon 825 and Jeffamine® D-230 layered epoxy sample (Sample ID 158) as produced by the Prospa software (Magritek). The top layer of Epon 825 and Jeffamine® D-2000 is located between a depth of 1500 and 3000 μm. The bottom layer of Epon 825 and Jeffamine® D-230 is located between a depth of 1200 and 0 μm. The slope of the interface region, between 1200 and 1500 μm, indicates the sample is tilted with respect to the sensitive volume.
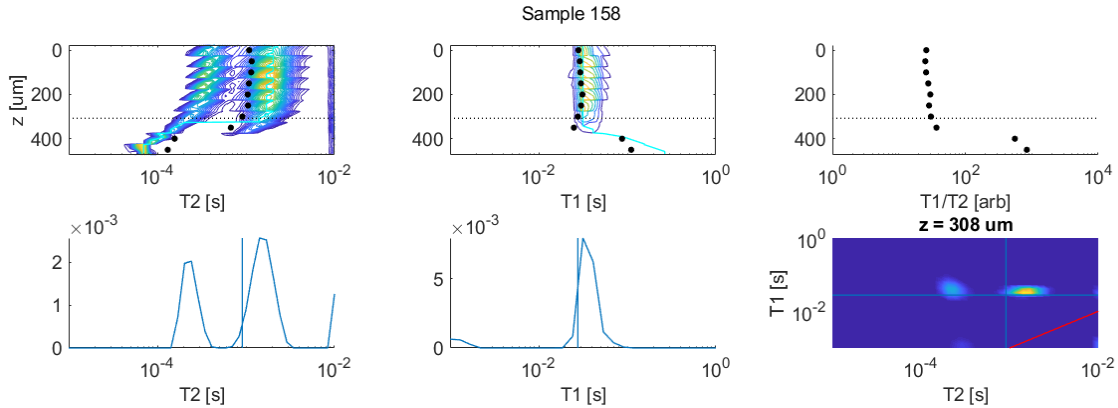
Figure 29: T_1 and T_2 data of the Epon 825 and Jeffamine® D-2000 and Epon 825 and Jeffamine® D-230 layered epoxy sample (Sample ID 158) showing position vs T_2 (s) (top-left), position vs T_1 (s) (top-middle), and position vs T_1–T_2 (top-right). This T_1–T_2 experiment was run with a total of 10 lift positions and a step-size of 50 μm starting in the top layer of the sample and ending in the bottom layer, capturing the interface in-between. The top layer of Epon 825 and Jeffamine® D-2000 is located between a depth of 0 and 300 μm. The bottom layer of Epon 825 and Jeffamine® D-230 is located around a depth of 500 μm. The slanted slope of the interface region, between 300 and 500 μm, indicates the sample is tilted with respect to the sensitive volume. Black dots represent the respective mean T_1 or T_2 value at that position.

5.5 Conclusion and Future Directions

In conclusion, the T_1–T_2 measurements discussed in this chapter provided a reliable and consistent way to measure epoxy thicknesses, interphase thicknesses, T_1/T_2 ratios throughout entire samples, changes in T_1/T_2 slopes, and increased SNR measurements of T_1/T_2 ratios at the interfaces of surface treated epoxy samples. These measurements were able to distinguish samples with surface treatments that increased surface energy, untreated and silane amine, from those with surface treatments that decreased surface energy: fluoro-silane, Teflon, and Vydax. The smaller interphase thicknesses of the Teflon and Vydax treated samples coincided with the lower chemical adhesion of the epoxy due to the hydrophobicity of the surface treatments. A lower T_1/T_2

70

ratio of the fluoro-silane treated sample provided evidence for the lower surface energy, which aligned with our expectations based on chemical properties of fluoro-silane surface treatments.

However, further investigation is needed for mitigating the tilt of the epoxy samples with respect to the sensitive volume. Addressing the tilted samples would allow for more reliable T_1/T_2 data and assessment of changes in T_1/T_2 ratios to quantify surface energies and further characterize the quality of adhesion between epoxy and a substrate. An apparatus is currently being engineered to mitigate this problem. From there, longer experiments could be performed only at the epoxy/substrate interface, like in **Figure 29**, to increase SNR of T_1–T_2 measurements.

Future directions of T_1–T_2 measurements are to focus on correlating chemical adhesion and surface energies of surface treated samples with their respective mechanical strength data from various adhesion tests. Pull of testing and lap shear testing of various samples are currently underway at Metna Corporation. The overall goal is for T_1/T_2 data to be able to infer information about the adhesion and mechanical strength of various samples without having to conduct destructive adhesion tests on them. In order to do so, enough data from both T_1–T_2 measurements and adhesion tests would need to be collected that showed agreeance in their conclusions of chemical and mechanical strength. This would require many replicate NMR measurements with SNR of T_1/T_2 data on the order of 20-30 consistently for all samples. T_1–T_2 measurements and adhesion tests would also need to be repeated on various aged samples to test the quality of the adhesion strength as samples aged or were exposed to various environmental conditions.

From there, T_1–T_2 measurements can be explored for their use in defect detection of epoxy samples. Samples with known defects would need to be made to perform such T_1–T_2 measurements. For example, a defected sample could be made by putting a thin layer of sand onto a substrate before casting the epoxy onto it. The sand has no ^{1}H NMR signal and would act as a void in the epoxy sample. Being able to detect changes in T_1–T_2 measurements where a known defect is present is key in determining the reliability of its use for defect detection. Overall, the future of the T_1–T_2 measurements aims to characterize the adhesion strength of various samples that would reliably detect defects in order to limit the need for destructive adhesion tests on epoxy resins used for broader applications throughout the manufacturing industry.

Chapter 6: Kinetics

Single-sided NMR provides measurements that are capable of non-destructive, *in-situ* monitoring of curing epoxy resins to analyze kinetic parameters for assurance of optimized crosslink formation and final physical properties of the cured epoxy network. Both single-sided NMR relaxometry and DSC measurements were used to evaluate the real-time curing of an epoxy resin with various diamine curing agents. NMR relaxometry was used to measure the change in relaxation time, T_2, throughout the cure process, both at room temperature and elevated temperatures. DSC measurements were used to measure both the heat of reaction and residual enthalpy of the epoxy samples, which are further explained in section 6.3. Together, both methods allowed for the measured extent of cure while comparing the chemical curing and molecular confinement during the cure process. Comparison of cure extent between various diamine curing agents helps to better understand the cure kinetics of epoxy resins on a molecular level.

6.1 Sample Preparation

All reagents in this chapter were used as received by suppliers. Epon 825 (Hexion; Columbus, OH) and Bisphenol A diglycidyl ether (DGEBA, Sigma Aldrich) were the epoxy resins used in this chapter. Epon 825 is a high purity bisphenol A epichlorohydrin liquid epoxy with an equivalent weight of 175-180 g/eq per epoxide. DGEBA has a molecular weight of 340 g/mol and an equivalent weight of 172-176 g/eq per epoxide. The curing agents used in this chapter include Jeffamine® D-230 (Huntsman; The Woodlands, TX), Jeffamine® D-400 (Huntsman; The Woodlands, TX), ethylenediamine (EDA, Sigma Aldrich), 1,2-diaminopropane (1,2DAP, Sigma Aldrich),

1,3-diaminopropane (1,3DAP, Sigma Aldrich), and 1,4-diaminobutane (1,4DAB, Sigma Aldrich). A table containing molecular weights, amine hydrogen equivalent weights (AHEW), distance between each amine group (linker length), and stoichiometric ratio to 10 grams of both Epon825 and DGEBA for all the curing agents can be seen in **Table 6.1 of Appendix B.** The distance between the two amine groups (linker length) for each curing agent was determined using ChemDraw3D (Perkin Elmer).

Epoxy resin and curing agent were mixed in a 100% stoichiometric ratio (resin-to-hardener) for all experiments. The stoichiometric ratio between curing agent and 10 grams of epoxy resin was determined by taking the equivalent weight of Epon 825 or DGEBA, respectively, and dividing it by the equivalent weight of the specific curing agent. The final amount calculated is per 10 grams of epoxy resin. A sample calculation for the stoichiometric ratio of EDA to 10.0 grams of Epon 825 can be seen below:

$$\frac{\left(10.0g \times \frac{eq}{176\ g}\ Epon\ 825\right)}{0.0667\ \frac{eq}{g}\ EDA} = 0.852\ g\ of\ EDA \qquad 6.1$$

Therefore, if 2012.4 mg of Epon 825 were measured, then 171 mg of EDA would be needed for a sample mixture with 100% stoichiometry.

Epoxy mixtures were prepared gravimetrically into weigh boats on a Sartorius Practum 124-1S analytical balance using respective stoichiometric ratios (seen in **Table 6.1** in **Appendix B**). After addition of curing agents, samples were stirred for three minutes to ensure homogeneity (total mass of epoxy samples were approximately 2 g). From that weigh boat, samples were aliquoted (10–20 mg) into Tzero (TA Instruments)

DSC pans using a glass pipette tip. The weigh boat with the bulk epoxy sample was placed on the PM5 for measurement and the DSC pans were used for either DSC ramps or isothermal measurements. Data collection began within 10–15 minutes after initial mixing.

6.2 Single-Sided NMR Methods

Transverse (T_2) NMR relaxation information of epoxy samples was acquired using the Carr-Purcell-Meiboom-Gill (CPMG) sequence as described in Chapter 3.1.1 of this thesis. The pulse duration was 2.75 µs for both 90° and 180° pulses (pulse with powers of 2.14 mT and 4.27 mT, respectively). A 44 µs delay between refocusing pulses was used in all CPMG measurements, and spin echo data were acquired for 16 µs. An explanation of each acquisition parameter term can be found in **Appendix C**.

Initial kinetics studies consisted of measuring the room temperature cure of Epon 825 with EDA, Jeffamine® D-230, and Jeffamine® D-400 to compare T_2 relaxation times throughout the cure process for varying lengths of diamine curing agents. Many independent CPMG measurements were performed to capture changes in T_2 as a function of curing time. To optimize the trade-off between temporal resolution during the curing process and the signal-to-noise ratio of the NMR measurements, NMR parameters were assigned to four "blocks" as detailed in **Table 6.2** in **Appendix A**. In the very beginning of the epoxy cure, the T_2 relaxation time is the longest, due to the molecular mobility of the viscous uncured epoxy resin. As the resin gels and later vitrifies, the T_2 relaxation time decreases due to the reduced molecular mobility (explained in Ch. 3.1.1). Therefore, the beginning blocks of the CPMG experiments have more echoes and fewer scans because

more signal needs to be acquired over a longer period of time to capture the full echo train decay. As the kinetics experiments were expanded to study both Epon 825 and DGEBA cure with various curing agents at elevated temperatures, the CPMG measurements were refined to capture faster cures. These refined parameters can be seen in **Table 6.3** of **Appendix A**. For heat cure NMR measurements, the PM5 was housed in a climate chamber (Memmert HPP10) to maintain constant temperatures throughout epoxy cure.

6.3 Differential Scanning Calorimetry (DSC)

DSC is a thermal analysis technique that is used to measure the amount of heat required to increase the temperature of a sample is measured as a function of temperature.[107] In other words, a sample with a known mass is heated and the changes in its heat capacity are measured as changes in the heat flow. Two parameters measured via DSC are utilized in this thesis: total heat of reaction (ΔH) and residual enthalpy of curing. The total heat of reaction (ΔH) of a sample is measured from a DSC ramp experiment where the epoxy sample is subjected to a heating and cooling procedure. Essentially, the epoxy sample is subjected to an increase in thermal energy that pushes the reaction to completion. As bonds are formed in the crosslinking epoxy sample, a change in heat flow is measured from the exothermic reactions. The resulting thermograms show the measured heat flow from the reacting epoxy network over time and the area underneath the exothermic peak is equivalent to the total heat of reaction in J g^{-1}. The residual enthalpy of a sample can be measured from a DSC isothermal experiment where the sample is held at a specified temperature over a period of time for curing followed by a ramp in temperature. Any residual uncured material remaining in the sample following the isotherm cure is measured from the area under the curve as the residual enthalpy.

In this thesis, DSC measurements were performed on a Q20 differential scanning calorimeter (TA Instruments; New Castle, DE). Nitrogen purge gas (50 mL/min) was used throughout the DSC experiments. Initial experiments only used ramp experiments to measure the total heat of reaction (ΔH) at various time intervals throughout the cure process. Latter experiments performed ramp and isothermal experiments to measure the total heat of reaction (ΔH) and residual enthalpy, respectively. For the ramp experiments, a sample pan was placed in the DSC and subjected to heating (25 °C to 300 °C at 20 °C/min) followed by cooling (to 25 °C at 40 °C/min). This heating and cooling procedure was then immediately repeated to verify the complete cure of the sample during the first heating. Isothermal experiments were performed with simultaneous NMR measurements in which a sample pan was placed in the DSC and subjected to elevated isothermal temperatures (50, 60, 80, or 100 °C) for the entire cure and immediately followed by a cooling (to 0 °C at 40 °C/min) and heating (to 300 °C at 20 °C/min) ramp to measure any remaining reaction in the epoxy sample.

6.4 Data Processing

Both single-sided NMR and DSC data were processed using MATLAB scripts (MathWorks Inc.; Natick, MA) developed in our lab by Dr. Tyler Meldrum. Epoxy cure model fits were formed using the built-in in non-linear fitting module *fitnlm* in MATLAB. The echo train decay data from the CPMG experiments were subjected to an inverse Laplace transformation to obtain a T_2 distribution at each cure time, as previously explained in Ch. 4. These distributions were used to determine the mean-log relaxation time (T_2) value at each cure time. Total heat of reaction and residual enthalpies for each sample were collected from the DSC software as a function of cure time. The extent of

curing (α), also known as degree of conversion, for each technique is separately determined by:

$$\alpha(t) = 1 - \frac{X(t)}{X(0)} \qquad\qquad 6.2$$

where *X* is the observable parameter for each technique and *t* is the time of curing. *X(0)* is the value of measurement at time zero immediately after the sample was mixed and prepared for measurement. The degree of cure (α) ranges from 0 (completely uncured) to 1 (fully cured). For DSC measurements, *X* is the residual enthalpy or total heat of reaction, and for NMR measurements it is the mean-log of the T_2 distribution. The time-dependent extent of curing was initially fit to a four parameter Weibull function of the form:

$$\alpha(t|A, b, w, c) = 1 - Ae^{-(bt)^w} + c \qquad\qquad 6.3$$

where *b* characterizes the rate of curing, *w* (Weibull parameter) characterizes the shape of the curing curve, *A* is the amplitude of the decay curve, *t* is the epoxy cure time, and *c* should be near zero and is the y-offset to account for the non-zero value of fully cured epoxy.

As kinetics experiments were expanded to measure epoxy cure at elevated temperatures, an autocatalytic reaction model, developed by Kamal and Malkin[108] and widely applied to model the cure of epoxy resins via DSC,[109,110] was tested. The autocatalytic Kamal–Malkin model is as follows

$$\frac{d\alpha}{dt} = (k_1 + k_2\alpha^m)(1 - \alpha)^n \qquad\qquad 6.4$$

where k_1 is the rate of initiation where an amine first reacts with an epoxide, k_2 is the autocatalytic rate, and α is the cure rate. The term $k_2\alpha^m$ is the influence of the products on the reaction rate whereas $(1-\alpha)^n$ is the effect of the autocatalytic cure rate as the epoxy systems become vitrified. The larger the value of m, the slower the reaction proceeds in the beginning whereas the larger the value of n, the autocatalytic part of the reaction speeds up and vitrification proceeds.

6.5 Results and Discussion

Initial kinetics experiments were performed at room temperature to compare the curing kinetics of Epon 825 with EDA, Jeffamine® D-230, and Jeffamine® D-400 via simultaneous DSC and NMR measurements. After a sample was prepared, the weigh boat with the bulk epoxy and curing agent mixture was placed on the PM5 for CPMG measurement and the DSC pans were left to cure on the benchtop under ambient conditions. One DSC pan was placed in the calorimeter at every time interval (every hour for the first 8 hours, 10, 12, 14, 16, 18, and 28th hour for Epon 825 with EDA and Jeffamine® D-230; intervals up to 100 hours were needed for Jeffamine® D-400) to measure the heat of reaction (ΔH) at each interval throughout the curing process via ramp procedures (explained in section 6.3 of this chapter).

The samples reached full room-temperature cure after several hours, as depicted by the decrease in their respective total heats of reaction obtained by the DSC. Representative thermograms from the Epon825/Jeffamine® D-230 sample can be seen in

79

Figure 30. Similar cure results are seen with DSC and NMR data overlaid representing

cure rate as a function of time using the Weibull fit (Eq. 6.3) in **Figure 31**. When ranking

the curing rate of Epon 825, EDA cures the resin the fastest, followed by Jeffamine® D-

230 and finally Jeffamine® D-400, as seen in **Figure 31.**
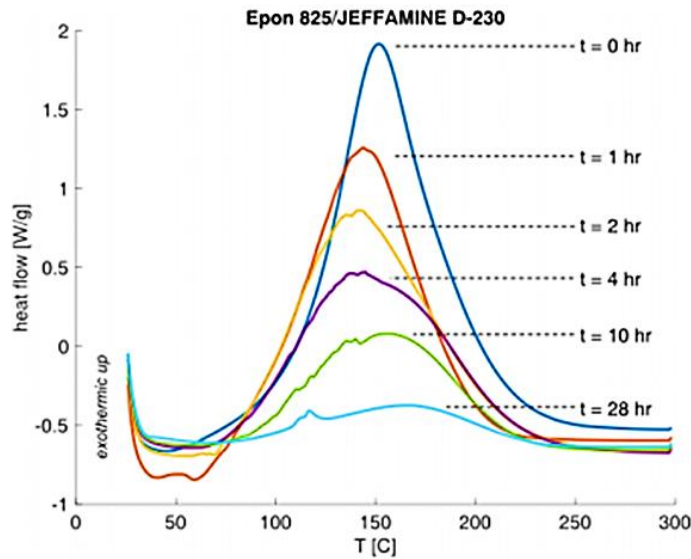
Figure 30: Thermograms showing the heat flow at each time interval of room-temperature curing of a Epon825/Jeffamine® D-230 sample. The area under each curve is integrated to extract the total heat of reaction (ΔH) at that interval. The decreasing peak size at each increasing time interval indicates a lower total heat of reaction representative of the curing epoxy sample (fewer available reaction sites; fewer bonds formed via the DSC heating procedure).
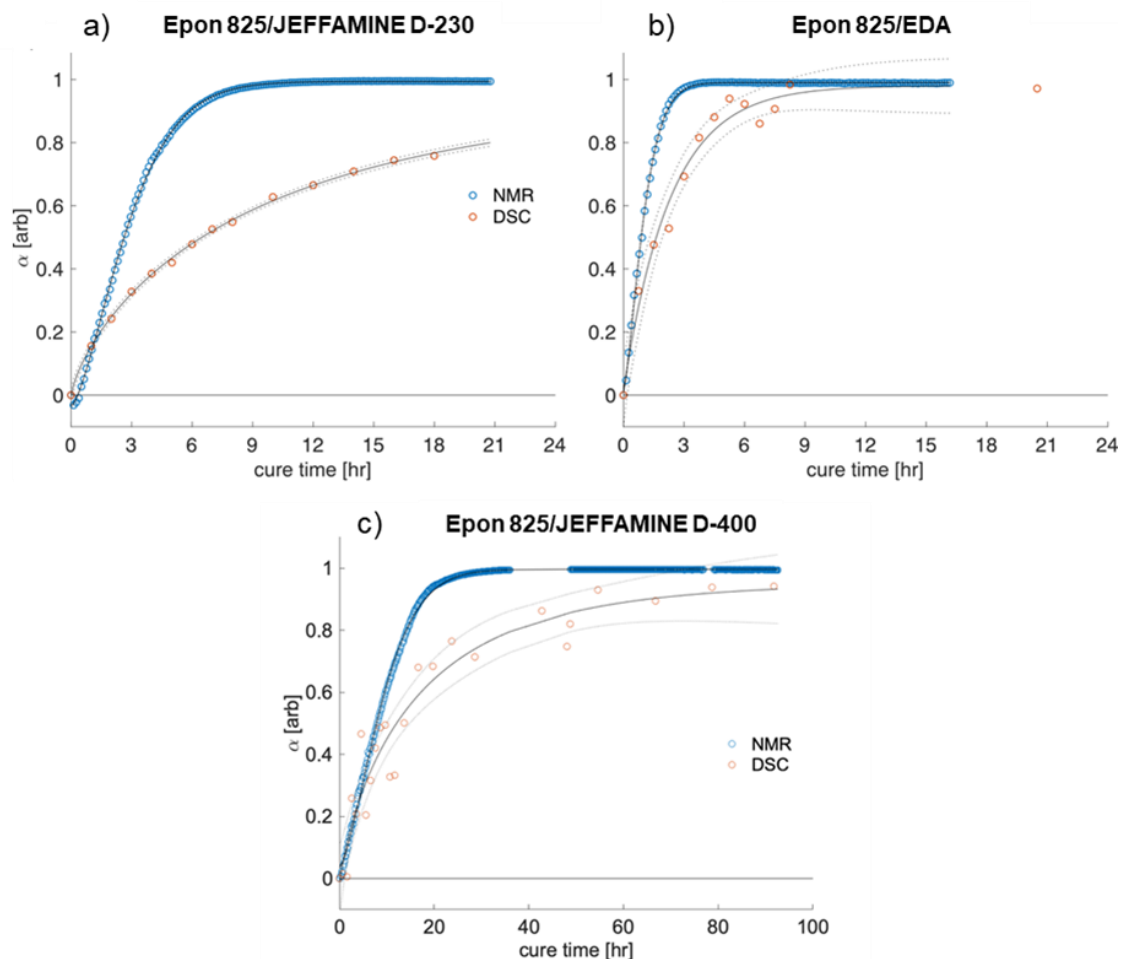
Figure 31: Extent of cure (α) as a function of cure time for Epon825/Jeffamine® D-230 (a), Epon825/EDA (b), and Epon825/Jeffamine® D-400 (c). Blue points come from NMR data; orange points from DSC data. Data modeled to the Weibull fit are seen in the solid black lines with 95% confidence intervals in the dashed black lines. All methods show changes as the system cures at room temperature. Epon825/Jeffamine® D-230 (a) was cured and measured for 24 hours at room temperature, Epon825/EDA (b) for 17 hours at room temperature, and Epon825/Jeffamine® D-400 (c) for 100 hours. The break in the Epon825/Jeffamine D-400 sample around 40 hours is indicative of the CPMG debugger crashing in the middle of the night while acquiring data (another crash happened around 80 hours). The debugger was immediately restarted to continue acquiring data, however data during those cure times were lost.

NMR and DSC data modeled using the Weibull fit (Eq. 6.3) have fit parameters seen in **Table 6.4.** Values for *A* and *c* are approximately one and zero, respectively, given that the epoxy samples reached full cure ($A = 1$) and the extent of cure at time zero, immediately after mixing, is zero ($c = 0$). The small relative uncertainties seen in the NMR and DSC data reflect an advantage of nondestructive methods—single-sided NMR measurements can provide more temporal points to define the extent of cure without destroying the sample thus resulting in smaller uncertainty in the data.

Table 6.4: Fit coefficients for extent-of-cure vs. cure time for room-temperature curing

	Epon 825 JEFFAMINE D-230		Epon 825 JEFFAMINE D-400		Epon 825 EDA	
	DSC	NMR	DSC	NMR	DSC	NMR
A [arb]	0.96 ± 0.01	1.029 ± 0.003	1.0 ± 0.1	0.960 ± 0.002	0.97 ± 0.07	0.981 ± 0.0043
b [hr^{-1}]	0.104 ± 0.003	0.3078 ± 0.0009	0.06 ± 0.02	0.0964 ± 0.0002	0.43 ± 0.05	0.874 ± 0.004
w [arb]	0.76 ± 0.02	1.463 ± 0.008	0.8 ± 0.2	1.493 ± 0.008	1.0 ± 0.1	1.38 ± 0.01
c [arb]	-0.040 ± 0.005	-0.0067 ± 0.0006	-0.05 ± 0.09	-0.0032 ± 0.0004	-0.02 ± 0.04	-0.01 ± 0.0005

The parameters *b* and *w* characterize the rate and shape of curing, respectively. We hypothesize that differences in *w* between NMR and DSC data arise from what each technique probes. The Weibull parameter, *w*, can also be used to describe the chemical nature of the observed curing because different chemistries would reflect different shapes. For example, epoxy resins cured with very molecularly small curing agents (like EDA) would cure very fast and have a shape of curing that looks more like an exponential curve than that of a slowly curing epoxy resin.

NMR measurements via CPMG experiments probe the molecular motion of epoxy resins, specifically rotations of individual molecules and functional groups, as well as translations of those molecules, while DSC probes the enthalpic changes as amines form bonds to epoxides creating a crosslinked network. DSC and NMR measurements of cure extent mirror each other in the early stages of cure as chemical bond formation affects molecular motion. For example, as amines and epoxides react, the total heat of reaction (ΔH) remaining, measured via DSC, will decrease. Similarly, the T_2 relaxation time will decrease because those individual amines and epoxides no longer translate and rotate independently of one another. However, molecular motion is also restricted by molecular confinement. For example, a Jeffamine® D-230 molecule that is trapped within the crosslinked epoxy network but has not yet formed bonds with the surrounding epoxy molecules. Thus, NMR measurements would show relatively small, if not zero, molecular mobility of the trapped, immobile Jeffamine® D-230 molecule. In the NMR data, this would appear as though the epoxy sample is "cured" or, in other words, has reached the stage of gelation due to the reduction in molecular mobility. DSC measurements, on the other hand, would continue to show enthalpic changes as the trapped Jeffamine® D-230 molecules form bonds to the epoxy network. This difference in the nature of NMR and DSC measurements explains why the NMR data reach an apparent "full cure" faster than the DSC data as reflected from the magnitude of the cure rates, *b*, and seen in extent of cure [$\alpha(t)$] plots in **Figure 30.** Because of this, we suspect that NMR more so measures the rate of gelation whereas DSC measures the rate of vitrification of these epoxies.

Data shows that the *w* Weibull parameters for the epoxy samples cured with Jeffamine® D-230 and D-400 are consistent: approximately 0.76 and 0.8 [arb] for DSC,

respectively, and 1.463 and 1.493 [arb] for NMR, respectively (**Table 6.5**). This indicates that the chemical nature of the observed curing between the two curing agents is similar for both. The only difference between Jeffamine® D-230 and D-400 molecularly is that D-400 has a longer ether chain between the amine groups, therefore it is understandable that the nature of the observed curing, represented by *w*, is similar for both.

However, the rate of the observed curing, *b*, between Jeffamine® D-230 and D-400 are inconsistent: *b* for Jeffamine® D-230 is 1.75 times larger than for Jeffamine® D-400 (DSC) and 3.2 times larger for that of NMR. (**Table 6.5**). Due to the length of the larger curing agent, Jeffamine® D-400, it takes a longer time to form a crosslinked network with the Epon 825 epoxy resin compared to the shorter Jeffamine® D-230. As illustrated in Ch. 2, molecules of the curing agents first react with molecules of the epoxy resin, resulting in chain extensions. In a sample of Jeffamine® D-400 and Epon 825, because of their length, the extended chains have a higher probability of chain entanglement and take longer to become oriented in the sample such that crosslinking with other chains can occur, thus having a slower rate of cure.

Comparing the ratio of the measured rate constants, *b*, from both NMR and DSC may provide insight into how the length of the diamine curing agents affect both the molecular mobility and the final structure of the cured epoxy network. When $b_{NMR}/b_{DSC} = 1$, the rate of change of the molecular mobility (NMR) equals the rate of change of the chemical process (DSC). Between Jeffamine® D-230 and D-400, the ratio of *b* for NMR and DSC measurements indicate that the chemical process (DSC) the two curing agents use to become a crosslinked network with Epon 825 is more similar than their mobility process (NMR). For Jeffamine® D-400, the ratio $b_{NMR}/b_{DSC} = 1.61 \pm$

0.30, and for Jeffamine® D-230 that ratio is $b_{NMR}/b_{DSC} = 2.96 \pm 0.03$. The ratio of b_{NMR}/b_{DSC} for Jeffamine® D-230 is 83% larger than that of Jeffamine® D-400. In other words, changes measured due to reduced mobility via NMR at room temperature occur over 0.83 times as fast for the Jeffamine® D-230 compared to Jeffamine® D-400. For EDA, the ratio $b_{NMR}/b_{DSC} = 2.0 \pm 0.1$ is nearly 50% less than Jeffamine® D-230. From these ratios, we determined that changes measured due to reduced mobility (NMR) occur twice as fast as those due to chemical crosslinking (DSC) when using EDA, but three times as fast when using the longer diamine Jeffamine® D-230. This supports the idea of a greater possibility of molecular confinement in the Jeffamine® D-230 sample, in which molecular mobility of the larger curing agent is reduced more quickly, than in the (molecularly) smaller EDA sample. Because of this, we expected that the ratio of b_{NMR}/b_{DSC} for Jeffamine® D-400 would be even larger than that of the Jeffamine® D-230. We hypothesized that there is a greater possibility of molecular confinement in the Jeffamine® D-400 sample, in which molecular mobility of the larger curing agent is reduced more quickly, than in the (molecularly) smaller Jeffamine® D-230 sample.

Room temperature curing is not optimal for full crosslinking of these samples and thus true full curing of these samples, especially the larger curing agents, is not occurring. Industrially, epoxy resins are typically always cured at higher temperatures (often around 80°C and higher) to increase the thermal energy and molecular mobility of these systems thus ensuring optimal crosslink formation. For the Jeffamine® D-400, it is possible that the molecules are so large that the crosslinked formation is kinetically slow at room temperature because the molecular mobility of the molecularly larger curing agents are much lower than the molecularly smaller curing agents, hindering their ability to form

dense 3D networks. This could explain why the cure extent of EDA via NMR and DSC in the $[\alpha(t)]$ plots (**Figure 30**) both approach 1, whereas both Jeffamine® D-230 and Jeffamine® D-400 $[\alpha(t)]$ plots for DSC do not reach 1, indicating that the chemical reaction (bond formation) in those epoxy systems is not complete. Because of this, it is inferred that the ratio of b_{NMR}/b_{DSC} for Jeffamine® D-400 (in **Table 6.4**) was not larger than that of Jeffamine® D-230, as hypothesized, because both of these samples are not optimally curing and crosslinking at room temperature. We hypothesized that future curing of these samples at elevated temperatures would show a ratio of b_{NMR}/b_{DSC} Jeffamine® D-400 that is larger than that of Jeffamine® D-230.

Kinetics experiments were refined to test the above findings with other curing agents of various linker lengths to allow a more thorough analysis of these data. Diamine curing agents 1,2-diaminopropane (1,2DAP), 1,3-diaminopropane (1,3DAP), and 1,4-diaminobutane (1,4DAB) were included in the kinetics study. A DGEBA epoxy resin was also used to compare kinetics results of the curing agents with different epoxy resins. Curing was performed via NMR measurements in a climate chamber (seen in **Figure 11** in Ch. 4) at 25°C, 33°C, and 40°C (subjecting the PM5 to temperatures higher than 40°C runs the risk of damage to the instrument). DSC analyses were expanded to include both isothermal experiments at elevated temperatures, to obtain residual enthalpies after curing, and ramp experiments, to obtain total heats of reaction ($\mathit{\Delta H}$). The Kamal–Malkin model, which is widely applied to DSC kinetics experiments, was used to fit both NMR and DSC data for testing of a more precise fitting procedure.

The samples reached essentially full cure after several hours as manifest by the cure extent of $\alpha(t)$ plots reaching 1 for both NMR and DSC measurements. Representative

NMR data for a 33°C cure of a DGEBA/1,4DAB sample can be seen in **Figure 32**

showing the change in T_2 relaxation time and cure extent as a function of time.

Representative DSC data for isothermal experiments of DGEBA/1,4DAB samples can be

seen in **Figure 33** showing the cure extent as a function of time. Kamal−Malkin fit

parameters and uncertainties for all samples from both NMR and DSC measurements can

be seen in **Tables 6.5-6.6** in **Appendix B**. Any data sets that are missing from the tables

are because those NMR or DSC data sets could not fit to the Kamal−Malkin model and

therefore no fit parameters were obtained.
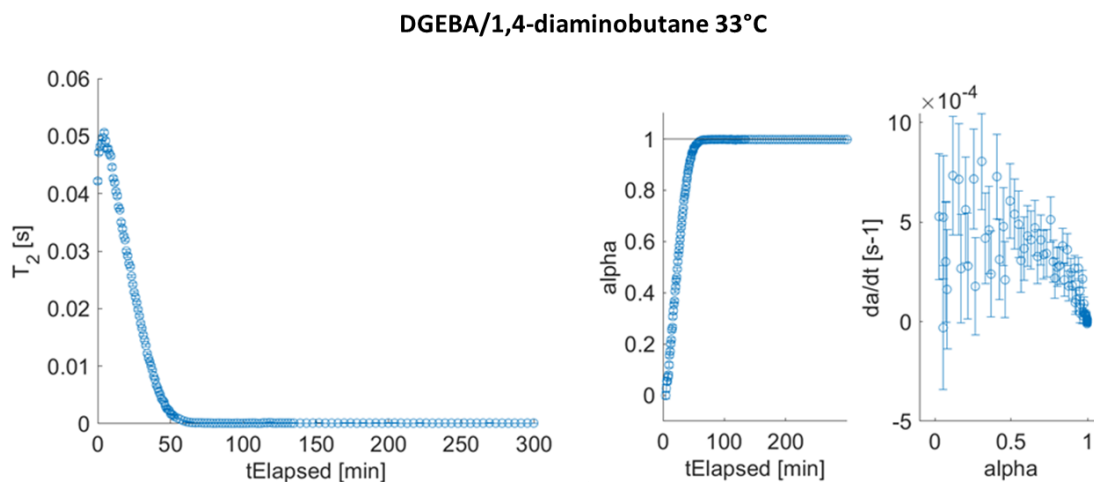
Figure 32: Kamal−Malkin fit for NMR data of the T_2 relaxation time (left) and extent of cure (right) both as a function of cure time for a DGEBA/1,4DAB sample at 33°C. The right plot also includes a plot of the rate of reaction ($d\alpha/dt$ [s^{-1})] as a function of alpha (α) with error bars to display the uncertainties in the measurement as the cure extent proceeds in the 3rd plot on the right.
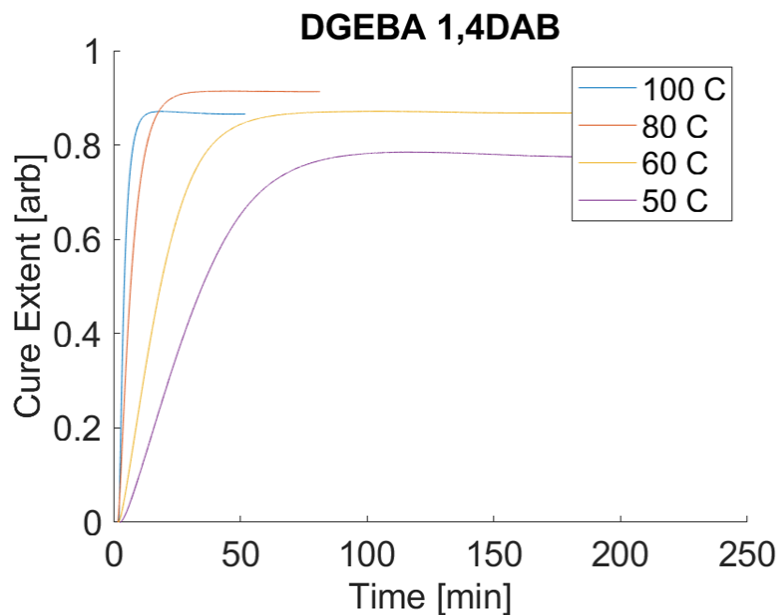
Figure 33: Kamal–Malkin fit for the isothermal DSC data of extent of cure (α) as a function of cure time for a DGEBA/1,4DAB sample at 50°C, 60°C, 80°C, and 100°C.

For both the DSC and NMR measurements on DGEBA and Epon 825 epoxy resins, each Kamal–Malkin parameter, k_1, k_2, m and n, were plotted against molecular weights and distance between amine groups (N-N distance; seen in **Table 6.1** of **Appendix B**) for all cure temperatures. This was done to determine whether or not a pattern between Kamal–Malkin parameters for each sample is seen amongst different curing agents that would provide insight on the cure kinetics of these epoxy systems. No trends in the Kamal–Malkin parameters for both DSC and NMR data of DGEBA and Epon 825 were seen when plotted against molecular weights of the curing agents, as shown in **Figure 34**. However, when the curing agent N-N distance was plotted against each Kamal–Malkin parameter, a trend was seen for the NMR measurements of the DGEBA epoxy resin when plotted against the autocatalytic rate, k_2, for each curing agent

(**Figure 35**). At an N-N distance of 4.836 Å (1,3DAP curing agent) the autocatalytic rate, k_2, is the fastest for the DGEBA epoxy resin at 25°C and 40°C, with 33°C showing slight discrepancies. When the same plot was compared to that for the Epon 825 epoxy resin, a different trend was noted (**Figure 36**). As seen in **Figure 36**, it appears that the autocatalytic rate, k_2, is continually increasing for the Epon 825 epoxy resin and has not yet reached a plateau, like seen in the DGEBA data in **Figure 35**.
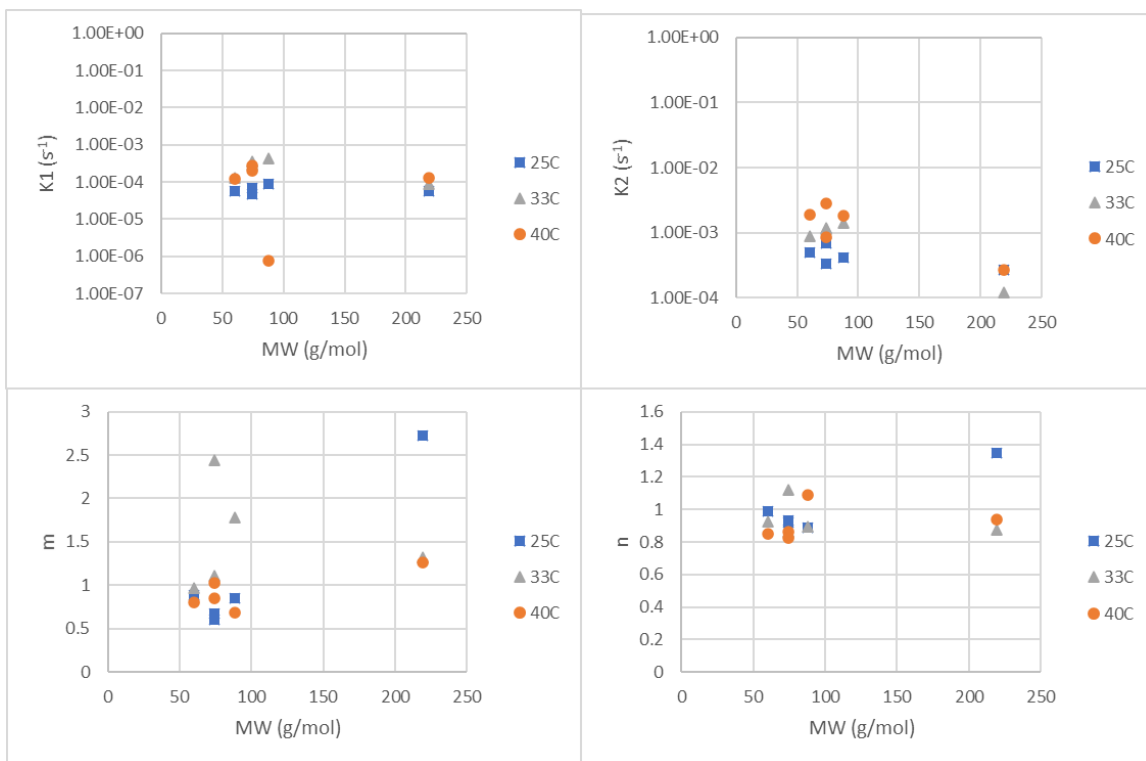
Figure 34: The Kamal−Malkin NMR fit data for k_1 (top-left), k_2 (top-right), m (bottom-left), and n (bottom-right) plotted against the molecular weights of curing agents for the DGEBA epoxy resin cured at 25°C, 33°C, and 40°C with all five curing agents. Similar data (with no obvious trends) of Kamal−Malkin parameters versus molecular weights of curing agents were seen for NMR data of Epon 825 and DSC data for both DGEBA and Epon 825.
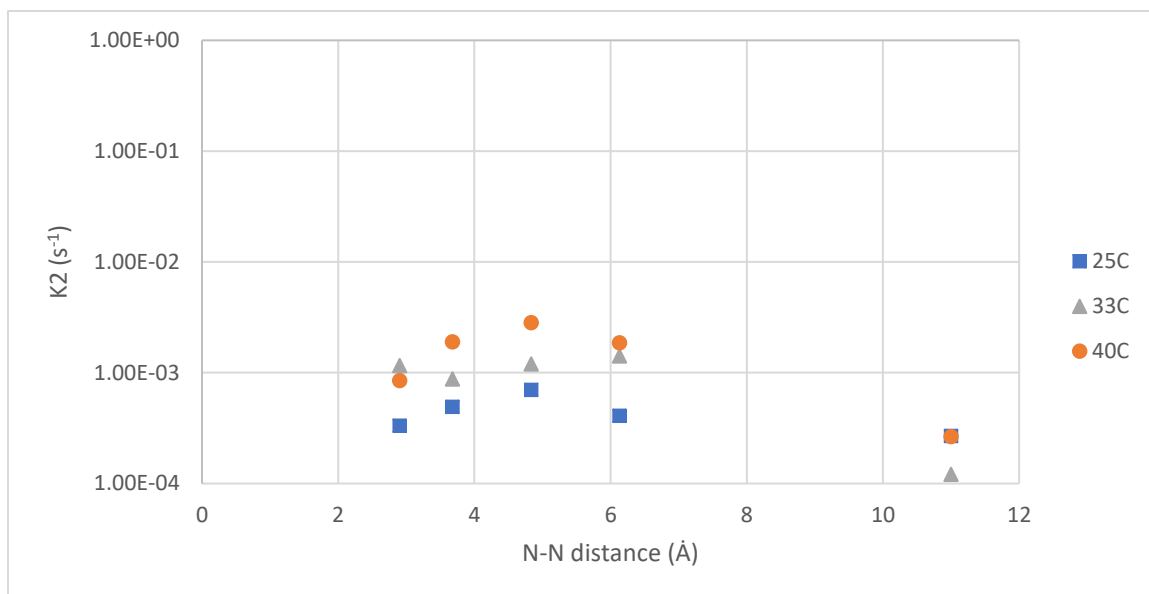
Figure 35: The Kamal–Malkin NMR fit data of the autocatalytic rate parameter, k_2, plotted against the N-N distance (Å) of the curing agents for the DGEBA epoxy resin cured at 25°C, 33°C, and 40°C (the uncertainty values can be found in Table 6.5 of Appendix B).
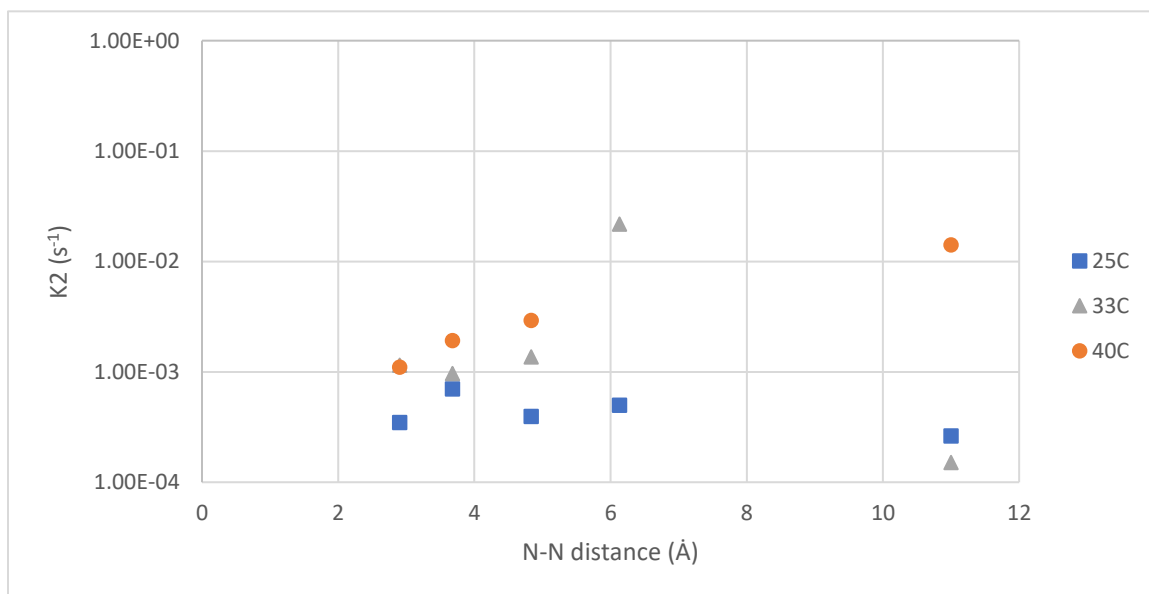
Figure 36: The Kamal–Malkin NMR fit data of the autocatalytic rate parameter, k_2, plotted against the N-N distance (Å) of the curing agents for Epon 825 epoxy resin cured at 25°C, 33°C, and 40°C. A data point is missing for the curing agent 1,4DAB at 33°C because that data set could not fit to the Kamal–Malkin model (the uncertainty values can be found in Table 6.5 of Appendix B).

It is possible that the trend seen in the autocatalytic rate, k_2, for the DGEBA epoxy resin is indicative of a "sweet spot" for the length of curing agent. In other words, a curing agent length around 5 Å between amine groups (1,3DAP) for curing the DGEBA epoxy resin is long enough that extended chains can reach the next epoxy molecule and continue crosslinking, but not so long that it has a hard time orienting itself in the sample to crosslink with other chains. On the other hand, the increasing autocatalytic rate, k_2, for the Epon 825 epoxy resin might indicate that for some reason, whether it is a longer chain or has more steric hindrance than DGEBA, the 11 Å value still hasn't reached that "sweet spot" of curing yet. However, the structure of Epon 825 is proprietary, so this is hard to conclude, but it is a possible answer for why rising values of the autocatalytic kinetic parameter are seen for Epon 825, most notably in 40°C. As discussed in the initial room temperature cure kinetics experiments, the room temperature cures do not display optimal curing, which can also be seen in **Figure 36** for Epon 825 where the autocatalytic rates are relatively consistent at 25°C. DSC measures the total chemical reaction all the way through to vitrification of the epoxy resins whereas NMR more so measures the process of gelation in these epoxy systems (molecular mobility decreases to zero as the system gels). It is possible that room temperature cure of the epoxy systems is just not able to get full gelation, much less vitrification, with the large curing agents like Jeffamine® D-230.

The Kamal–Malkin model provided insight on the amine curing agents' linker lengths (N-N distance) effects on the autocatalytic curing rate, k_2, for DGEBA and Epon 825 epoxy resins. Specifically, it appears as though there is a "sweet spot" length of curing agent for the DGEBA epoxy resin, suggesting how those epoxy systems cure

molecularly. Further experiments would need to be performed to validate these claims and test them with the Epon 825 epoxy resin.

6.6 Conclusion and Future Directions

In this chapter, it was shown how single-sided NMR can be used to probe the curing of epoxies by tracking changes in the (NMR) relaxation parameter T_2 and thus correlations with changes in molecular mobility. Consideration of the effective rates of curing obtained by fitting both the NMR and DSC data to two different models have provided insight on how molecular mobility, cure kinetics, molecular confinement, and chemical reactions can be assessed. Using the Weibull fit for NMR and DSC data, we determined that the nature of the observed curing (w) was similar for both Jeffamine® D-230 and D-400, however the rates (b) of change in molecular mobility and chemically were very different. It also appeared that the molecularly smaller curing agent (EDA) was less likely to become confined in the epoxy network than larger ones (Jeffamine® D-230 and D-400). Refining the kinetics studies to use the Kamal–Malkin model for NMR and DSC data, the distance between amine groups (linker lengths) of the curing agents appeared to have an effect on the autocatalytic curing rate of the epoxy resins, such that the curing of a DGEBA epoxy resin was the fastest when curing with a linker length of around 5 Å. NMR results were comparable with those obtained by DSC and have shown the complementarity between those methods, with advantages for the non-destructive use of single-sided NMR.

The Kamal–Malkin model does not provide the most precise fit for these data considering both NMR and DSC are large ranges of data that were each fit to a four-

parameter model in which some data sets even had difficulty fitting to. In order to validate the claims in this chapter, NMR kinetics experiments would need to be performed at higher temperatures than 40°C. Longer curing agents, like Jeffamine® D-400, need to be included in future experiments to determine whether or not Epon 825 has a "sweet spot" curing agent length like that of DGEBA. It would also be good to de-gas samples in future kinetics experiments, to allow for more homogenous crosslinking of samples and prevent gas bubbles from being trapped in the samples during heat cure. Because some of the data were not fitting to the Kamal–Malkin model, a Weibull fit could be used for the elevated temperature kinetics, like in the preliminary room temperature studies, to provide better fits for both DSC and NMR data.

Appendix A: Experiment Parameters

Table 5.1: Profile experiment parameters

90/180 amplitude (dB)	–8/–2
pulse length (µs)	4.0
resolution (µm)	200
number of echoes	32
number of complex points	16
number of scans	256
repetition time (ms)	300
initial depth (µm)	3100
final depth (µm)	0
step size (µm)	100

Table 5.2: CPMG experimental parameters

90°/180° amplitude (dB)	–8/–2
pulse length (µs)	4.0
dwell time (µs)	1.0
acquisition time (µs)	16
echo time (µs)	44
number of echoes	32
number of complex points	16
number of scans	1024
repetition time (ms)	300

Table 5.3: Saturation recovery experiment parameters

90°/180° amplitude (dB)	–8/–2
pulse length (μs)	4.0
dwell time (μs)	0.5
acquisition time (μs)	8
echo time (μs)	26
number of echoes	32
number of complex points	16
number of scans	1024
repetition time (ms)	300
estimate of T_1	variable based on material
number of T_1 points	11
maximum recovery time (ms)	5xT_1 estimate

Table 5.4: T_1-T_2 experiment parameters

90°/180° amplitude (dB)	–8/–2 dB
pulse length (μs)	4.0 μs
dwell time (μs)	1.0
echo time (μs)	44 μs
number of echoes	32
number of complex points	16
number of scans	1024
repetition time (ms)	375
estimate of T_1 (ms)	115
number of T_1 points	17
maximum recovery time (ms)	375
lift step size (μm)	250
number of lift positions	2

Table 6.2: NMR Acquisition Parameters for Long-Term Cure Monitoring at RT

Common NMR Parameters	
B1 frequency	19.44 MHz
Bandwidth	1000
Pulse length	2.75 μs
Pulse power (90°/180° pulses)	-10/-4 dB
Dwell time	1 μs
Complex points	16
Acquisition time	16 μs
Group 1 Cure time 0-4 hours	
Number of echoes	8192
Repetition time	15000 ms
Number of scans	32
Number of measurements	20
Group 2 Cure time 4-6 hours	
Number of echoes	4096
Repetition time	7500 ms
Number of scans	64
Number of measurements	20
Group 3 Cure time 6-8 hours	
Number of echoes	1024
Repetition time	1875 ms
Number of scans	256
Number of measurements	20
Group 4 Cure time 8-36 hours	
Number of echoes	512
Repetition time	900 ms
Number of scans	512
Number of measurements	20-200

Table 6.3: NMR Acquisition Parameters for Long-Term Fast-Cure Monitoring at RT and Elevated Temperatures

Common NMR Parameters	
B1 frequency	19.44 MHz
Bandwidth	1000
Pulse length	3.0 μs
Pulse power (90°/180° pulses)	-10/-4 dB
Dwell time	1 μs
Complex points	16
Acquisition time	16 μs
Group 1 Cure time 0-2 hours	
Number of echoes	8192
Repetition time	15400 ms
Number of scans	4
Number of measurements	120
Group 2 Cure time 2-6 hours	
Number of echoes	4096
Repetition time	7800 ms
Number of scans	16
Number of measurements	120
Group 3 Cure time 6-20 hours	
Number of echoes	512
Repetition time	1000 ms
Number of scans	256
Number of measurements	50-200

Table 5.5: Spatial extent of three regions from multiple user observations.

SAMPLE		Air/Epoxy Interface (Segment 1) spatial extent (μm)			Bulk Epoxy (Segment 2) spatial extent (μm)			Epoxy/Surface Interface (Segment 3) spatial extent (μm)		
		min	max	median	minimum	maximum	median	minimum	maximum	median
Untreated A		62	73	71	1000	1096	1034	35	104	84
Untreated B		42	154	93	865	1015	954	89	112	98
Untreated ALL	U			73			1005			98
Silane amine A		54	127	71	1004	1235	1179	35	196	79
Silane amine B		69	104	91	1150	1215	1190	73	116	91
Silane amine ALL	S			83			1182			81
Fluorosilane A		35	142	90	912	969	932	66	103	93
Fluorosilane B		42	69	54	1012	1058	1035	27	53	39
Fluorosilane ALL	F			54			990			59
Teflon A		50	96	68	961	1015	1008	46	62	50
Teflon B		42	150	103	862	992	931	45	80	76
Teflon ALL	T			71			977			56
Vydax A		15	120	93	758	889	791	26	84	40
Vydax B		35	127	104	738	796	742	23	69	50
Vydax ALL	V			98			767			50
AVERAGE		45	116	84	926	1028	980			
MEDIAN		42	123	90	937	1015	981			
ST DEV		15	30	17	125	134	145			

Averages for Segment 3 are omitted because we expect the spatial extent of the interphase for differently treated substrates to vary.

Table 5.6: Slope (|T1/T2| per μm) of three regions from multiple user observations.

SAMPLE	Air/Epoxy Interface (Segment 1) slope (|T1/T2|/μm)			Bulk Epoxy (Segment 2) slope (|T1/T2|/μm)			Epoxy/Surface Interface (Segment 3) slope (|T1/T2|/μm)		
	minimum	maximum	median	minimum	maximum	median	minimum	maximum	median
Untreated A	-0.0312	-0.0194	-0.0237	-8.04E-05	-7.33E-05	-7.67E-05	0.0044	0.0203	0.0099
Untreated B	-0.0270	-0.0030	-0.0057	2.47E-05	5.36E-05	4.26E-05	0.0060	0.0105	0.0068
Untreated ALL			-0.0194			-2.43E-05			0.0070
Silane amine A	-0.0108	-0.0017	-0.0040	5.79E-06	3.08E-05	8.95E-06	0.0008	0.0241	0.0181
Silane amine B	-0.0153	-0.0102	-0.0118	-2.11E-05	-1.20E-05	-1.79E-05	0.0037	0.0048	0.0045
Silane amine ALL			-0.0105			-3.10E-06			0.0047
Fluorosilane A	-0.0465	-0.0055	-0.0237	-1.00E-04	-5.97E-05	-9.03E-05	0.0017	0.0081	0.0032
Fluorosilane B	-0.0186	-0.0169	-0.0182	-4.10E-05	-3.42E-05	-3.62E-05	0.0127	0.0168	0.0146
Fluorosilane ALL			-0.0182			-5.03E-05			0.0104
Teflon A	-0.0084	-0.0063	-0.0080	-2.88E-05	-1.64E-05	-1.98E-05	0.0116	0.0263	0.0128
Teflon B	-0.0138	-0.0035	-0.0047	-5.06E-05	3.53E-05	2.90E-05	0.0135	0.0229	0.0168
Teflon ALL			-0.0080			-1.98E-05			0.0138
Vydax A	-0.1151	-0.0088	-0.0117	-3.82E-05	7.47E-05	1.19E-05	0.0062	0.0137	0.0109
Vydax B	-0.0290	-0.0091	-0.0120	6.09E-05	1.06E-04	6.64E-05	0.0119	0.0198	0.0186
Vydax ALL			-0.0117			6.16E-05			0.0133
AVERAGE	-0.0316	-0.0084	-0.0123	-2.7E-05	1.0E-05	-8.2E-06			
MEDIAN	-0.0228	-0.0075	-0.0118	-3.4E-05	9.4E-06	-4.5E-06			
ST DEV	0.0315	0.0059	0.0073	4.8E-05	5.9E-05	5.0E-05			

Averages for Segment 3 are omitted because we expect the slope of the T1/T2 ratio in the interphase for differently treated substrates to vary.

99

Table 5.7: T1/T2 ratio of segment 2 from multiple user observations.

SAMPLE		Air/Epoxy Interface (Segment 1) T1/T2			Bulk Epoxy (Segment 2) T1/T2			Epoxy/Surface Interface (Segment 3) T1/T2		
		minimum	maximum	median	minimum	maximum	median	minimum	maximum	median
Untreated A					1784	1807	1795			
Untreated B					1526	1545	1531			
Untreated ALL	U						1665			
Silane amine A					1546	1566	1550			
Silane amine B					1491	1497	1493			
Silane amine ALL	S						1521			
Fluorosilane A					1615	1631	1618			
Fluorosilane B					1502	1511	1503			
Fluorosilane ALL	F						1563			
Teflon A					1557	1564	1558			
Teflon B					1441	1487	1462			
Teflon ALL	T						1522			
Wydax A					1451	1478	1472			
Wydax B					1518	1536	1526			
Wydax ALL	V						1498			
AVERAGE					1543	1562	1551			
MEDIAN					1522	1540	1529			
ST DEV					99	97	97			

Averages for Segments 1 and 3 are omitted. These regions are where the T1/T2 ratio is clearly varying and a blunt characterization of a middle value of T1/T2 seems inappropriate. The slope in this region is more appropriate (see Table 3).

Table 6.1: Curing Agent Stoichiometry and Information

Curing Agent	MW (g/mol)	AHEW (g/eq)	meq/g	N-N distance (Å)	10 g Epon: X g linker	10 g DGEBA: X g linker
Ethylenediamine (EDA)	60	15	66.7	3.676	0.852	0.881
1,2-diaminopropane (1,2DAP)	74	18.5	54.0	3.417	1.053	1.089
1,3-diaminopropane (1,3DAP)	74	18.5	54.1	4.836	1.051	1.087
1,4-diaminobutane (1,4DAB)	88	22	45.5	6.130	1.250	1.293
Jeffamine® D230	230	59.5	16.8	11.001	3.381	3.496
Jeffamine® D400	400	113.5	8.8	17.277	6.449	6.668

Table 6.5: Kamal–Malkin fit parameters for NMR cure data at 25°C, 33°C, and 40°C.

Epon825|JefD230	Epon825|1,4DAB	Epon825|1,3DAP	Epon825|EDA	Epon825|1,2DAP	DGEBA|JefD230	DGEBA|1,4DAB	DGEBA|1,3DAP	DGEBA|EDA	DGEBA|1,2DAP		
-2.51E-05	-1.30E-04	1.41E-05	1.16E-04	1.60E-05	3.14E-05	8.65E-05	4.77E-05	5.88E-05	6.94E-05	K1	
1.45E-05	6.20E-05	9.31E-06	6.30E-06	2.30E-05	2.37E-06	4.20E-06	1.91E-05	0.02	6.94E-05	±	
1.39E-04	4.97E-04	3.95E-04	6.99E-04	3.48E-04	1.14E-04	4.08E-04	7.00E-04	4.93E-04	3.33E-04	K2	
1.22E-05	5.20E-05	9.97E-06	3.70E-05	1.50E-05	2.51E-06	1.40E-05	1.91E-05	2.30E-05	1.01E-05	±	NMR DATA @ 25C
0.257	0.227	0.518	1.074	0.375	0.622	0.853	0.607	0.88	0.675	m	
0.044	0.05	0.040	0.06	0.06	0.041	0.04	0.06	0.05	0.04	±	
0.888	0.789	0.927	1.007	0.895	0.924	0.888	0.931	0.99	0.922	n	
0.01	0.02	0.02	0.02	0.02	0.01	0.02	0.02	0.02	0.02	±	
1.08E-04	-2.09E-02	4.51E-04	1.77E-04	3.19E-04	8.96E-05	4.39E-04	3.47E-04	1.26E-04	3.00E-04	K1	
8.22E-07	0.20	7.39E-06	1.47E-05	2.54E-06	1.03E-06	1.01E-05	7.38E-06	0.03	2.71E-06	±	
1.51E-04	2.17E-02	1.36E-03	9.65E-04	1.15E-03	1.21E-04	1.42E-03	1.20E-03	8.77E-04	1.16E-03	K2	
9.08E-06	0.201	7.81E-05	2.73E-05	7.83E-05	6.63E-06	1.09E-04	4.40E-05	3.15E-05	7.23E-05	±	NMR DATA @ 33C
1.716	0.008	1.616	0.765	2.807	1.318	1.775	1.111	0.964	2.44	m	
0.063	0.074	0.065	0.045	0.067	0.062	0.095	0.041	0.04	0.06	±	
0.952	0.681	0.935	0.781	1.148	0.877	0.895	0.861	0.926	1.12	n	
0.01	-0.02	0.00	0.01	0.02	0.00	0.02	0.01	0.02	0.02	±	
-1.38E-02		1.38E-04	4.47E-05	-1.10E-04	1.28E-04	7.56E-07	2.77E-04	1.22E-04	1.97E-04	K1	
2.00E-01		2.80E-05	3.10E-05	4.20E-05	1.40E-06	1.28E-05	2.00E-05	1.50E-05	6.60E-06	±	
1.41E-02		2.92E-03	1.92E-03	1.10E-03	2.66E-04	1.86E-03	2.83E-03	1.90E-03	8.51E-04	K2	
2.00E-01		0.0001	5.90E-05	2.70E-05	1.01E-05	3.01E-05	1.00E-04	6.30E-05	2.20E-05	±	NMR DATA @ 40C
0.005		0.877	0.649	0.384	1.266	0.682	1.028	0.8	0.853	m	
0.08		0.05	0.04	0.04	0.04	0.02	0.06	0.03	0.03	±	
0.848		0.837	0.770	0.786	0.938	1.09	0.827	0.85	0.8657	n	
0.02		0.02	0.02	0.02	0.01	0.01	0.02	0.03	0.01	±	

Table 6.6: Kamal–Malkin fit parameters for DSC isotherm data at 50°C, 60°C, 80°C, and 100°C.

Epon825|JefD230	Epon825|1,4DAB	Epon825|1,3DAP	Epon825|EDA	Epon825|1,2DAP	DGEBA|JefD230	DGEBA|1,4DAB	DGEBA|1,3DAP	DGEBA|EDA	DGEBA|1,2DAP		
8.73E-06	8.84E-06	5.12E-05	4.33E-05	1.40E-05		8.45E-05	6.05E-05	7.57E-06	5.10E-06	K1	DSC DATA @ 50C
4.34E-07	3.50E-06	3.99E-06	3.89E-06	1.20E-06		2.10E-06	2.80E-06	1.81E-06	8.57E-07	±	
1.09E-04	6.36E-04	6.50E-04	8.65E-04	2.89E-04		7.15E-04	6.34E-04	5.22E-04	2.82E-04	K2	
4.63E-07	2.40E-04	2.82E-06	3.07E-06	8.60E-07		2.10E-06	2.20E-06	1.34E-06	7.02E-07	±	
0.41	0.28	0.3019	0.3436	0.25		0.275	0.339	0.33	0.352	m	
5.00E-03	4.00E-03	5.00E-03	4.20E-03	2.00E-03		7.00E-03	3.00E-03	3.00E-03	3.00E-03	±	
0.87	0.81	0.903	0.9198	0.87		0.895	0.868	0.86	0.933	n	
4.20E-03	3.00E-03	4.00E-03	3.80E-03	2.00E-03		5.00E-03	4.00E-03	2.60E-03	3.00E-03	±	
1.73E-05	1.99E-04	2.55E-05	1.68E-04	4.40E-06	2.05E-05	4.61E-06	1.63E-05	2.37E-05		K1	DSC DATA @ 60C
6.70E-07	5.80E-06	3.60E-06	4.83E-06	8.90E-07	5.70E-07	5.90E-06	4.60E-06	1.50E-06		±	
2.50E-04	1.20E-03	1.10E-03	1.40E-03	5.24E-04	2.19E-04	1.30E-03	9.81E-04	7.30E-04		K2	
9.98E-07	4.10E-06	2.70E-06	5.20E-06	6.30E-07	9.30E-07	4.30E-06	3.20E-06	1.20E-06		±	
0.44	0.258	0.215	0.3897	0.278	0.4522	0.2468	0.273	0.33		m	
0.004	0.003	0.001	0.0041	0.001	0.004	0.002	0.003	0.002		±	
1.12	0.925	1.019	1.036	0.841	1.109	0.9102	0.989	1.16		n	
4.00E-03	2.00E-03	1.00E-03	3.80E-03	9.50E-04	4.00E-03	2.00E-03	3.00E-03	2.00E-03		±	
1.18E-04	3.66E-05	3.29E-05	3.27E-04	3.87E-05	1.79E-05	2.04E-05	2.93E-04	0.0017	1.32E-06	K1	DSC DATA @ 80C
1.40E-06	6.20E-06	5.60E-06	5.10E-06	6.10E-06	9.90E-07	2.10E-06	3.70E-06	7.42E-06	2.50E-06	±	
7.11E-04	3.00E-03	2.40E-03	1.90E-03	1.40E-03	3.89E-04	2.30E-03	0.0015	0.0013	1.13E-03	K2	
4.70E-06	4.40E-06	4.10E-06	5.30E-06	4.60E-06	7.60E-07	1.50E-06	3.60E-06	6.62E-05	1.70E-06	±	
0.57	0.25	0.215	0.38	0.204	0.327	0.2514	0.365	0.76	0.263	m	
5.40E-03	1.00E-03	1.00E-03	3.00E-03	2.00E-03	2.00E-03	5.10E-04	3.00E-03	1.33E-02	1.00E-03	±	
1.24	0.96	1.27	1.13	1.21	1.122	1.0656	1.1704	1.45	1.198	n	
5.30E-03	1.00E-03	1.00E-03	3.00E-03	2.00E-03	2.00E-03	5.20E-04	3.00E-03	1.08E-02	2.00E-03	±	
1.81E-04	1.96E-04	3.41E-05	3.40E-03	4.14E-04	2.64E-04	1.50E-03	1.54E-05		3.27E-04	K1	DSC DATA @ 100C
2.15E-06	1.50E-05	1.74E-05	7.04E-06	9.40E-06	2.70E-06	1.40E-05	7.40E-06		1.02E-05	±	
9.94E-04	7.00E-03	4.20E-03	-2.10E-03	2.50E-03	1.50E-03	3.30E-03	0.0041		1.31E-03	K2	
7.25E-06	1.06E-05	1.38E-05	3.01E-04	6.40E-06	1.30E-05	2.60E-05	4.99E-06		7.28E-06	±	
0.54	0.245	0.1889	1.482	0.279	0.615	0.456	0.268		0.23	m	
0.006	0.001	0.002	0.0762	0.003	0.006	0.008	0.001		0.004	±	
1.44	1.05	1.29	0.758	1.48	1.493	1.19	1.304		1.28	n	
0.0063	0.001	0.002	0.0782	0.003	0.007	0.006	0.001		0.004	±	

Appendix C: Acquisition Parameters

90° and 180° Amplitude (dB): The power of the applied 90° on-resonance excitation and 180° refocusing pulse of the transmitting radio-frequency coil.

Pulse Length (µs): The time duration of the 90° and 180° pulses; this varies according to the number of spacers on the magnet with a value on the order of microseconds.

Echo time (µs): The time between two consecutive refocusing pulses. The echo time multiplied by the number of echoes is approximately equal to the length of one scan.

Number of Echoes: The number of echoes acquired in a single scan. Samples with long T_2 relaxation times require more echoes to capture the full signal decay.

Number of Scans: The number of times the experiment is repeated. Data acquired in each scan are added together to improve the SNR, therefore a larger amount of scans generate more signal, but increase the experiment time.

Repetition Time (ms): The time between two consecutive scans. The repetition time is the length of an entire scan and can be used to estimate the length of a full CPMG or T_1 saturation recovery experiment.

Number of Complex Points: The number of points collected to construct each echo. The acquisition time for an echo can be calculated by multiplying the number of complex points by the dwell time.

Dwell Time (µs): The length of time needed to collect each complex point of an echo.

Acquisition time: The length of time needed to collect one echo.

Maximum recovery time (ms): The maximum amount of time needed for the longest T_1

value of a sample to recover to equilibrium (5x T_1)

Bibliography

(1) Rajak, D. K.; Pagar, D. D.; Menezes, P. L.; Linul, E. Fiber-Reinforced Polymer Composites: Manufacturing, Properties, and Applications. *Polymers (Basel).* **2019**, *11* (10), 1667. https://doi.org/10.3390/polym11101667.

(2) Banea, M. D.; da Silva, L. F. M. Adhesively Bonded Joints in Composite Materials: An Overview. *Proc. Inst. Mech. Eng. Part L J. Mater. Des. Appl.* **2009**, *223* (1), 1–18. https://doi.org/10.1243/14644207JMDA219.

(3) Budhe, S.; Banea, M. D.; de Barros, S.; da Silva, L. F. M. An Updated Review of Adhesively Bonded Joints in Composite Materials. *Int. J. Adhes. Adhes.* **2017**, *72*, 30–42. https://doi.org/10.1016/j.ijadhadh.2016.10.010.

(4) Mohan, P. A Critical Review: The Modification, Properties, and Applications of Epoxy Resins. *Polymer - Plastics Technology and Engineering*. January 2013, pp 107–125. https://doi.org/10.1080/03602559.2012.727057.

(5) May, C. *Epoxy Resins: Chemistry and Technology*, 2nd ed.; Routledge, 1988.

(6) Pilato, L. A.; Michno, M. J.; Pilato, L. A.; Michno, M. J. Matrix Resins. In *Advanced Composite Materials*; Springer Berlin Heidelberg, 1994; pp 9–74. https://doi.org/10.1007/978-3-662-35356-1_2.

(7) Ellis, B. *Chemistry and Technology of Epoxy Resins*; Springer Netherlands, 1993. https://doi.org/10.1007/978-94-011-2932-9.

(8) Guadagno, L.; Raimondo, M.; Vittoria, V.; Vertuccio, L.; Naddeo, C.; Russo, S.; De Vivo, B.; Lamberti, P.; Spinelli, G.; Tucci, V. Development of Epoxy Mixtures for Application in Aeronautics and Aerospace. *RSC Adv.* **2014**, *4* (30), 15474–15488. https://doi.org/10.1039/C3RA48031C.

(9) Azeez, A. A.; Rhee, K. Y.; Park, S. J.; Hui, D. Epoxy Clay Nanocomposites - Processing, Properties and Applications: A Review. *Compos. Part B Eng.* **2013**, *45* (1), 308–320. https://doi.org/10.1016/j.compositesb.2012.04.012.

(10) Fry, C. G.; Lind, A. C. Determination of Crosslink Density in Thermoset Polymers by Use of Solid-State Proton NMR Techniques. *Macromolecules* **1988**, *21* (5), 1292–1297. https://doi.org/10.1021/ma00183a019.

(11) Hale, A.; Macosko, C. W.; Bair, H. E. Glass Transition Temperature as a Function of Conversion in Thermosetting Polymers. *Macromolecules* **1991**, *24* (9), 2610–2621. https://doi.org/10.1021/ma00009a072.

(12) Shefer, A.; Gottlieb, M. Effect of Cross-Links on the Glass Transition Temperature of End-Linked Elastomers. *Macromolecules* **1992**, *25* (15), 4036–4042. https://doi.org/10.1021/ma00041a028.

(13) Cai, H.; Li, P.; Sui, G.; Yu, Y.; Li, G.; Yang, X.; Ryu, S. Curing Kinetics Study of Epoxy Resin/Flexible Amine Toughness Systems by Dynamic and Isothermal DSC. *Thermochimica Acta*. 2008, pp 101–105.

https://doi.org/https://doi.org/10.1016/j.tca.2008.04.012.

(14) Froimowicz, P.; Gandini, A.; Strumia, M. New Polyfunctional Dendritic Linear Hybrids from Terminal Amine Polyether Oligomers (Jeffamine®): Synthesis and Characterization. *Tetrahedron Letters*. 2005, pp 2653–2657. https://doi.org/https://doi.org/10.1016/j.tetlet.2005.02.086.

(15) Fu, J.; Shi, L.; Zhang, D.; Zhong, Q.; Chen, Y. Effect of Nanoparticles on the Performance of Thermally Conductive Epoxy Adhesives. *Polym. Eng. Sci.* **2010**, *50* (9), 1809–1819. https://doi.org/10.1002/pen.21705.

(16) Montserrat, S.; Málek, J. A Kinetic Analysis of the Curing Reaction of an Epoxy Resin. *Thermochimica Acta*. 1993, pp 47–60. https://doi.org/https://doi.org/10.1016/0040-6031(93)80273-D.

(17) Roşu, D.; Mustǎţǎ, F.; Caşcaval, C. N. Investigation of the Curing Reactions of Some Multifunctional Epoxy Resins Using Differential Scanning Calorimetry. *Thermochimica Acta*. 2001, pp 105–110. https://doi.org/https://doi.org/10.1016/S0040-6031(00)00787-5.

(18) LeMay, J. D. Structure and Ultimate Properties of Epoxy Resins. *Adv. Polym. Sci.* **1986**, 115–148. https://doi.org/10.1007/bfb0035359.

(19) Vyazovkin, S.; Sbirrazzuoli, N. Kinetic Methods to Study Isothermal and Nonisothermal Epoxy-Anhydride Cure. *Macromol. Chem. Phys.* **1999**, *200* (10), 2294–2303. https://doi.org/10.1002/(SICI)1521-3935(19991001)200:10<2294::AID-MACP2294>3.0.CO;2-V.

(20) Blanco, M.; Corcuera, M. A.; Riccardi, C. C.; Mondragon, I. Mechanistic Kinetic Model of an Epoxy Resin Cured with a Mixture of Amines of Different Functionalities. *Polymer (Guildf)*. **2005**, *46* (19), 7989–8000. https://doi.org/10.1016/j.polymer.2005.06.117.

(21) Paz-Abuin, S.; Lopez-Quintela, A.; Pellin, M. P.; Varela, M.; Prendes, P. Autoacceleration and Inhibition: Free Volume. Epoxy-Amine Kinetics. *J. Polym. Sci. Part A Polym. Chem.* **1998**, *36* (6), 1001–1016. https://doi.org/10.1002/(SICI)1099-0518(19980430)36:6<1001::AID-POLA15>3.0.CO;2-9.

(22) Achilias, D.; Karabela, M.; Varkopoulou, E.; Sideridou, I. Cure Kinetics Study of Two Epoxy Systems with Fourier Tranform Infrared Spectroscopy (FTIR) and Differential Scanning Calorimetry (DSC). *J. Macromol. Sci. Part A* **2012**, *49*, 630–638. https://doi.org/10.1080/10601325.2012.696995.

(23) Fava, R. A. Differential Scanning Calorimetry of Epoxy Resins. *Polymer (Guildf)*. **1968**, *9* (C), 137–151. https://doi.org/10.1016/0032-3861(68)90024-4.

(24) Vyazovkin, S.; Sbirrazzuoli, N. Mechanism and Kinetics of Epoxy-Amine Cure Studied by Differential Scanning Calorimetry. *Macromolecules* **1996**, *29* (6), 1867–1873. https://doi.org/10.1021/ma951162w.

(25) Gonzalez, M.; Cabanelas, J.; Baselga, J. *Applications of FTIR on Epoxy Resins-*

Identification, Monitoring the Curing Process, Phase Separation and Water Uptake; InTech, 2012.

(26)   Adams, A. Trends in Analytical Chemistry. *Trends Anal. Chem.* **1982**, *83*, 107–119.

(27)   Choi, S.; Douglas, E. P. Complex Hygrothermal Effects on the Glass Transition of an Epoxy-Amine Thermoset. *ACS Appl. Mater. Interfaces* **2010**, *2* (3), 934–941. https://doi.org/10.1021/am9009346.

(28)   Spiess, H. W. 50th Anniversary Perspective: The Importance of NMR Spectroscopy to Macromolecular Science. *Macromolecules* **2017**, *50* (5), 1761–1777. https://doi.org/10.1021/acs.macromol.6b02736.

(29)   Chae, Y. K.; Kang, W. Y.; Jang, J. H.; Choi, S. S. A Simple NMR Method to Measure Crosslink Density of Natural Rubber Composite. *Polym. Test.* **2010**, *29* (8), 953–957. https://doi.org/10.1016/j.polymertesting.2010.08.003.

(30)   Fujimoto, K.; Nishi, T.; Kado, R. Multiple-Pulse Nuclear Magnetic Resonance Experiments on Some Crystalline Polymers. *Polym. J.* **1971**, *3* (4), 448–462. https://doi.org/10.1295/polymj.3.448.

(31)   Casanova, F.; Perlo, J.; Blumich, B. *Single-Sided NMR*; Casanova, F., Perlo, J., Blümich, B., Eds.; Springer-Verlag: Berlin Heidelberg, 2011.

(32)   Eidmann, G.; Savelsberg, R.; Blümler, P.; Blümich, B. The NMR MOUSE, a Mobile Universal Surface Explorer. *Journal of Magnetic Resonance, Series A*. 1996, pp 104–109. https://doi.org/https://doi.org/10.1006/jmra.1996.0185 ".

(33)   Possart, W. *Adhesion: Current Research and Applications*; John Wiley & Sons, 2006.

(34)   Hernández-Sánchez, N.; Hills, B. P.; Barreiro, P.; Marigheto, N. An NMR Study on Internal Browning in Pears. *Postharvest Biol. Technol.* **2007**, *44* (3), 260–270. https://doi.org/10.1016/j.postharvbio.2007.01.002.

(35)   Marigheto, N.; Venturi, L.; Hills, B. Two-Dimensional NMR Relaxation Studies of Apple Quality. *Postharvest Biol. Technol.* **2008**, *48* (3), 331–340. https://doi.org/10.1016/j.postharvbio.2007.11.002.

(36)   Marigheto, N.; Duarte, S.; Hills, B. P. NMR Relaxation Study of Avocado Quality. *Appl. Magn. Reson.* **2005**, *29* (4), 687–701. https://doi.org/10.1007/BF03166344.

(37)   Callaghan, P. T. *Translational Dynamics and Magnetic Resonance*; Oxford University Press, 2013. https://doi.org/10.1093/acprof:oso/9780199556984.001.0001.

(38)   Capitani, D.; Sobolev, A. P.; Di Tullio, V.; Mannina, L.; Proietti, N. Portable NMR in Food Analysis. *Chemical and Biological Technologies in Agriculture*. Springer International Publishing July 17, 2017, pp 1–14. https://doi.org/10.1186/s40538-017-0100-1.

(39)   Blumich, B.; Casanova, F.; Perlo, J.; Presciutti, F.; Anselmi, C.; Doherty, B. Noninvasive Testing of Art and Cultural Heritage by Mobile NMR. *Acc. Chem. Res.* **2010**, *43* (6), 761–770. https://doi.org/10.1021/ar900277h.

(40)   Del Federico, E.; Centeno, S. A.; Kehlet, C.; Currier, P.; Stockman, D.; Jerschow, A. Unilateral NMR Applied to the Conservation of Works of Art. *Anal. Bioanal. Chem.* **2010**, *396* (1), 213–220. https://doi.org/10.1007/s00216-009-3128-7.

(41)   Blümich, B.; Haber, A.; Casanova, F.; Del Federico, E.; Boardman, V.; Wahl, G.; Stilliano, A.; Isolani, L. Noninvasive Depth Profiling of Walls by Portable Nuclear Magnetic Resonance. In *Analytical and Bioanalytical Chemistry*; Anal Bioanal Chem, 2010; Vol. 397, pp 3117–3125. https://doi.org/10.1007/s00216-010-3880-8.

(42)   Haber, A.; Blümich, B.; Souvorova, D.; Del Federico, E. Ancient Roman Wall Paintings Mapped Nondestructively by Portable NMR. *Anal. Bioanal. Chem.* **2011**, *401* (4), 1441–1452. https://doi.org/10.1007/s00216-011-5180-3.

(43)   Blümich, B.; Anferova, S.; Sharma, S.; Segre, A. L.; Federici, C. Degradation of Historical Paper: Nondestructive Analysis by the NMR-MOUSE. *J. Magn. Reson.* **2003**, *161* (2), 204–209. https://doi.org/10.1016/S1090-7807(03)00034-X.

(44)   Proietti, N.; Capitani, D.; Pedemonte, E.; Blümich, B.; Segre, A. L. Monitoring Degradation in Paper: Non-Invasive Analysis by Unilateral NMR. Part II. *J. Magn. Reson.* **2004**, *170* (1), 113–120. https://doi.org/10.1016/j.jmr.2004.06.006.

(45)   Terenzi, C.; Casieri, C.; Felici, A. C.; Piacentini, M.; Vendittelli, M.; De Luca, F. Characterization of Elemental and Firing-Dependent Properties of Phlegrean Ceramics by Non-Destructive ED-XRF and NMR Techniques. *J. Archaeol. Sci.* **2010**, *37* (7), 1403–1412. https://doi.org/10.1016/j.jas.2009.12.044.

(46)   Casieri, C.; Terenzi, C.; De Luca, F. Two-Dimensional Longitudinal and Transverse Relaxation Time Correlation as a Low-Resolution Nuclear Magnetic Resonance Characterization of Ancient Ceramics. *J. Appl. Phys.* **2009**, *105* (3). https://doi.org/10.1063/1.3072685.

(47)   Van Landeghem, M.; D'Espinose De Lacaillerie, J. B.; Blümich, B.; Korb, J. P.; Bresson, B. The Roles of Hydration and Evaporation during the Drying of a Cement Paste by Localized NMR. *Cem. Concr. Res.* **2013**, *48*, 86–96. https://doi.org/10.1016/j.cemconres.2013.01.012.

(48)   McDonald, P. J.; Mitchell, J.; Mulheron, M.; Aptaker, P. S.; Korb, J. P.; Monteilhet, L. Two-Dimensional Correlation Relaxometry Studies of Cement Pastes Performed Using a New One-Sided NMR Magnet. *Cem. Concr. Res.* **2007**, *37* (3), 303–309. https://doi.org/10.1016/j.cemconres.2006.01.013.

(49)   Sharma, S.; Casanova, F.; Wache, W.; Segre, A.; Blümich, B. Analysis of Historical Porous Building Materials by the NMR-MOUSE®. In *Magnetic Resonance Imaging*; Elsevier Inc., 2003; Vol. 21, pp 249–255. https://doi.org/10.1016/S0730-725X(03)00132-2.

(50)   Rühli, F. J.; Böni, T.; Perlo, J.; Casanova, F.; Baias, M.; Egarter, E.; Blümich, B.

Non-Invasive Spatial Tissue Discrimination in Ancient Mummies and Bones in Situ by Portable Nuclear Magnetic Resonance. *J. Cult. Herit.* **2007**, *8* (3), 257–263. https://doi.org/10.1016/j.culher.2007.03.002.

(51)   Dias, M.; Hadgraft, J.; Glover, P. M.; McDonald, P. J. Stray Field Magnetic Resonance Imaging: A Preliminary Study of Skin Hydration. *J. Phys. D. Appl. Phys.* **2003**, *36* (4), 364–368. https://doi.org/10.1088/0022-3727/36/4/306.

(52)   Haken, R.; Blü;mich, B. Anisotropy in Tendon Investigated in Vivo by a Portable NMR Scanner, the NMR-MOUSE. *J. Magn. Reson.* **2000**, *144* (2), 195–199. https://doi.org/10.1006/jmre.2000.2040.

(53)   Kelley, M.; Abdol, N.; Soroushian, P.; Keating, K.; Balachandra, A. M.; Meldrum, T. Monitoring Real-Time Curing of Epoxies in Situ Using Single-Sided NMR. *J. Polym. Sci.* **2020**, *58* (4), 616–623. https://doi.org/10.1002/pol.20190117.

(54)   Gannon, J. A. History and Development of Epoxy Resins; Elsevier, 1986; pp 299–307. https://doi.org/10.1007/978-94-011-7073-4_29.

(55)   Goosey, M. T. *Epoxide Resins and Their Formulation*; Elsevier Applied Science Publ, 1985. https://doi.org/10.1007/978-94-017-2700-6_4.

(56)   Billmeyer, F. *Textbook of Polymer Science*, 3rd ed.; John Wiley & Sons, 1984.

(57)   Parry, G. W. Thermosetting Plastics. In *Plastics Forming*; Macmillan Education UK, 1971; pp 29–38. https://doi.org/10.1007/978-1-349-01194-0_3.

(58)   Critchley, J. P.; Knight, G. J.; Wright, W. W.; Critchley, J. P.; Knight, G. J.; Wright, W. W. Thermosetting Polymers. In *Heat-Resistant Polymers*; Springer US, 1983; pp 21–85. https://doi.org/10.1007/978-1-4899-0396-9_2.

(59)   Skeist, I. *Epoxy Resins*; Reinhold Publishing Corp.: New York, 1958.

(60)   Shokuhfar, A.; Arab, B. The Effect of Cross Linking Density on the Mechanical Properties and Structure of the Epoxy Polymers: Molecular Dynamics Simulation. *J. Mol. Model.* **2013**, *19* (9), 3719–3731. https://doi.org/10.1007/s00894-013-1906-9.

(61)   Montserrat, S.; Flaqué, C.; Pagès, P.; Málek, J. Effect of the Crosslinking Degree on Curing Kinetics of an Epoxy–Anhydride System. *J. Appl. Polym. Sci.* **1995**, *56* (11), 1413–1421. https://doi.org/10.1002/app.1995.070561104.

(62)   Ogata, M.; Kinjo, N.; Kawata, T. Effects of Crosslinking on Physical Properties of Phenol–Formaldehyde Novolac Cured Epoxy Resins. *J. Appl. Polym. Sci.* **1993**, *48* (4), 583–601. https://doi.org/10.1002/app.1993.070480403.

(63)   Xie, Q.; Fu, K.; Liang, S.; Liu, B.; Lu, L.; Yang, X.; Huang, Z.; Lü, F. Micro-Structure and Thermomechanical Properties of Crosslinked Epoxy Composite Modified by Nano-SiO2: A Molecular Dynamics Simulation. *Polymers (Basel).* **2018**, *10* (7). https://doi.org/10.3390/polym10070801.

(64)   Muc, A.; Romanowicz, P.; Chwał, M. Description of the Resin Curing Process—

Formulation and Optimization. *Polymers (Basel).* **2019**, *11* (1). https://doi.org/10.3390/polym11010127.

(65) Blackburn, B. P.; Tatar, J.; Douglas, E. P.; Hamilton, H. R. Effects of Hygrothermal Conditioning on Epoxy Adhesives Used in FRP Composites. *Constr. Build. Mater.* **2015**, *96*, 679–689. https://doi.org/10.1016/j.conbuildmat.2015.08.056.

(66) Raff, L. *Principles of Physical Chemistry*; Prentice Hall: New Jersey, 2001.

(67) Pople, J. A.; Schneider, W. G.; Bernstein, H. J. *High-Resolution Nuclear Magnetic Resonance*; McGraw-Hill, 1959.

(68) Hentschel, K. Zeeman Effect. In *Compendium of Quantum Physics*; Springer Berlin Heidelberg, 2009; pp 862–864. https://doi.org/10.1007/978-3-540-70626-7_241.

(69) Silverstein, R. M.; Webster, F. X.; Kiemle, D. J.; Bryce, D. L. *Spectrometric Identification of Organic Compounds Eighth Edition*; 2015.

(70) Bhacca, N. S.; Williams, D. H. Applications of NMR Spectroscopy in Organic Chemistry ; Illustrations from the Steroid Field. **1964**.

(71) Ionin, B. I.; Ershov, B. A.; Ionin, B. I.; Ershov, B. A. The Fundamentals of NMR Spectroscopy. In *NMR Spectroscopy in Organic Chemistry*; Springer US, 1970; pp 1–59. https://doi.org/10.1007/978-1-4684-1785-2_1.

(72) Dietrich, M. W.; Keller, R. E. Hydrogen Nuclear Magnetic Resonance Chemical Shift Correlation Charts for Organic Compounds. *Anal. Chem.* **1964**, *36* (2), 258–259. https://doi.org/10.1021/ac60208a004.

(73) Blümich, B.; Blümler, P.; Eidmann, G.; Guthausen, A.; Haken, R.; Schmitz, U.; Saito, K.; Zimmer, G. The NMR-Mouse: Construction, Excitation, and Applications. *Magnetic Resonance Imaging*. 1998, pp 479–484. https://doi.org/https://doi.org/10.1016/S0730-725X(98)00069-1.

(74) Perlo, J.; Casanova, F.; Blümich, B. Profiles with Microscopic Resolution by Single-Sided NMR. *J. Magn. Reson.* **2005**, *176* (1), 64–70. https://doi.org/10.1016/j.jmr.2005.05.017.

(75) Kolz, J. Applications in Material Science and Cultural Heritage. In *Single-Sided NMR*; Springer Berlin Heidelberg, 2011; pp 203–220. https://doi.org/10.1007/978-3-642-16307-4_9.

(76) Carr, H. Y.; Purcell, E. M. Effects of Diffusion on Free Precession in Nuclear Magnetic Resonance Experiments. *Phys. Rev.* **1954**, *94* (3), 630–638. https://doi.org/10.1103/PhysRev.94.630.

(77) Meiboom, S.; Gill, D. Modified Spin-Echo Method for Measuring Nuclear Relaxation Times. *Rev. Sci. Instrum.* **1958**, *29* (8), 688–691. https://doi.org/10.1063/1.1716296.

(78) Hahn, E. L. Spin Echoes. *Phys. Rev.* **1950**, *80* (4), 580–594. https://doi.org/10.1103/PhysRev.80.580.

(79) Levitt, M. H. *Spin Dynamics: Basics of Nuclear Magnetic Resonance*; Wiley, 2013.

(80) Hürlimann, M. D.; Venkataramanan, L. Quantitative Measurement of Two-Dimensional Distribution Functions of Diffusion and Relaxation in Grossly Inhomogeneous Fields. *J. Magn. Reson.* **2002**, *157* (1), 31–42. https://doi.org/10.1006/jmre.2002.2567.

(81) Kimmich, R. *NMR: Tomography, Diffusometry, Relaxometry*; Springer-Verlag: Berlin Heidelberg, 1997.

(82) Marshall, A. G.; Verdun, F. R. Fourier Transform Nuclear Magnetic Resonance Spectroscopy. In *Fourier Transforms in NMR, Optical, and Mass Spectrometry*; Elsevier, 1990; pp 279–330. https://doi.org/10.1016/b978-0-444-87360-6.50013-3.

(83) Venkataramanan, L.; Song, Y.-Q.; Hurlimann, M. D. Solving Fredholm Integrals of the First Kind with Tensor Product Structure in 2 and 2.5 Dimensions. *IEEE Trans. Signal Process.* **2002**, *50* (5), 1017–1026. https://doi.org/10.1109/78.995059.

(84) Song, Y. Q.; Venkataramanan, L.; Burcaw, L. Determining the Resolution of Laplace Inversion Spectrum. *J. Chem. Phys.* **2005**, *122* (10). https://doi.org/10.1063/1.1858436.

(85) Higgins, A. Adhesive Bonding of Aircraft Structures. *Int. J. Adhes. Adhes.* **2000**, *20* (5), 367–376. https://doi.org/10.1016/S0143-7496(00)00006-3.

(86) Prolongo, S. G.; Del Rosario, G.; Ureña, A. Comparative Study on the Adhesive Properties of Different Epoxy Resins. *Int. J. Adhes. Adhes.* **2006**, *26* (3), 125–132. https://doi.org/10.1016/j.ijadhadh.2005.02.004.

(87) Park, J. K.; Kim, M. O. The Effect of Different Exposure Conditions on the Pull-off Strength of Various Epoxy Resins. *J. Build. Eng.* **2021**, *38*, 102223. https://doi.org/10.1016/j.jobe.2021.102223.

(88) Désarmot, G.; Favre, J. P. Advances in Pull-out Testing and Data Analysis. *Compos. Sci. Technol.* **1991**, *42* (1–3), 151–187. https://doi.org/10.1016/0266-3538(91)90016-I.

(89) Krzywiński, K.; Sadowski, Ł. The Effect of Texturing of the Surface of Concrete Substrate on the Pull-Off Strength of Epoxy Resin Coating. *Coatings* **2019**, *9* (2), 143. https://doi.org/10.3390/coatings9020143.

(90) Ezquerro, C. S.; Laspalas, M.; Chiminelli, A.; Serrano, F.; Valero, C. Interface Characterization of Epoxy Resin Nanocomposites: A Molecular Dynamics Approach. *Fibers* **2018**, *6* (3). https://doi.org/10.3390/fib6030054.

(91) Zhang, C.; Hankett, J.; Chen, Z. Molecular Level Understanding of Adhesion Mechanisms at the Epoxy/Polymer Interfaces. **2012**.

https://doi.org/10.1021/am300854g.

(92) Sharpe, L. H. Interfaces, Interphases and "Adhesion": A Perspective. In *The Interfacial Interactions in Polymeric Composites*; Springer Netherlands, 1993; pp 1–20. https://doi.org/10.1007/978-94-011-1642-8_1.

(93) Jesson, D. A.; Watts, J. F. The Interface and Interphase in Polymer Matrix Composites: Effect on Mechanical Properties and Methods for Identification. *Polymer Reviews*. July 1, 2012, pp 321–354. https://doi.org/10.1080/15583724.2012.710288.

(94) Pilato, L. A.; Michno, M. J.; Pilato, L. A.; Michno, M. J. Composite Interphase. In *Advanced Composite Materials*; Springer Berlin Heidelberg, 1994; pp 108–113. https://doi.org/10.1007/978-3-662-35356-1_5.

(95) Miller, J. D.; Ishida, H. Adhesive—Adherend Interface and Interphase. In *Fundamentals of Adhesion*; Springer US, 1991; pp 291–324. https://doi.org/10.1007/978-1-4899-2073-7_10.

(96) Good, R. J. Contact Angle, Wetting, and Adhesion: A Critical Review. *J. Adhes. Sci. Technol.* **1992**, *6* (12), 1269–1302. https://doi.org/10.1163/156856192X00629.

(97) Baldan, A. Adhesion Phenomena in Bonded Joints. *Int. J. Adhes. Adhes.* **2012**, *38*, 95–116. https://doi.org/10.1016/j.ijadhadh.2012.04.007.

(98) Clint, J. H. Adhesion and Components of Solid Surface Energies. *Current Opinion in Colloid and Interface Science*. Elsevier February 1, 2001, pp 28–33. https://doi.org/10.1016/S1359-0294(00)00084-4.

(99) Bao, L.; Fan, H.; Chen, Y.; Yan, J.; Yang, T.; Guo, Y. Effect of Surface Free Energy and Wettability on the Adhesion Property of Waterborne Polyurethane Adhesive. *RSC Adv.* **2016**, *6* (101), 99346–99352. https://doi.org/10.1039/c6ra15899d.

(100) Robinson, N.; Robertson, C.; Gladden, L. F.; Jenkins, S. J.; D'Agostino, C. Direct Correlation between Adsorption Energetics and Nuclear Spin Relaxation in a Liquid-Saturated Catalyst Material. *ChemPhysChem* **2018**, *19* (19), 2472–2479. https://doi.org/10.1002/cphc.201800513.

(101) D'Agostino, C.; Mitchell, J.; Mantle, M. D.; Gladden, L. F. Interpretation of NMR Relaxation as a Tool for Characterising the Adsorption Strength of Liquids inside Porous Materials. *Chem. – A Eur. J.* **2014**, *20* (40), 13009–13015. https://doi.org/10.1002/chem.201403139.

(102) Molitor, P.; Barron, V.; Young, T. Surface Treatment of Titanium for Adhesive Bonding to Polymer Composites: A Review. *Int. J. Adhes. Adhes.* **2001**, *21* (2), 129–136. https://doi.org/10.1016/S0143-7496(00)00044-0.

(103) Jeenjitkaew, C.; Guild, F. J. The Analysis of Kissing Bonds in Adhesive Joints. *Int. J. Adhes. Adhes.* **2017**, *75*, 101–107. https://doi.org/10.1016/j.ijadhadh.2017.02.019.

(104) Fricke, S. N.; Seymour, J. D.; Battistel, M. D.; Freedberg, D. I.; Eads, C. D.; Augustine, M. P. Data Processing in NMR Relaxometry Using the Matrix Pencil. *J. Magn. Reson.* **2020**, *313*. https://doi.org/10.1016/j.jmr.2020.106704.

(105) Lin, Y.-Y.; Hodgkinson, P.; Ernst, M.; Pines, A. *A Novel Detection-Estimation Scheme for Noisy NMR Signals: Applications to Delayed Acquisition Data*; 1997; Vol. 128.

(106) Fiore, V.; Orlando, V.; Sanfilippo, C.; Badagliacco, D.; Valenza, A. Effect of Silane Coupling Treatment on the Adhesion between Polyamide and Epoxy Based Composites Reinforced with Carbon Fibers. *Fibers* **2020**, *8* (8), 48. https://doi.org/10.3390/fib8080048.

(107) Horie, K.; Hiura, H.; Sawada, M.; Mita, I.; Kambe, H. Calorimetric Investigation of Polymerization Reactions. III. Curing Reaction of Epoxides with Amines. *J. Polym. Sci. Part A-1 Polym. Chem.* **1970**, *8* (6), 1357–1372. https://doi.org/10.1002/pol.1970.150080605.

(108) Kamal, M. R.; Sourour, S.; Ryan, M. E. Integrated Thermo-Rheological Analysis of the Cure of Thermosets. *SPE Tech. Pap.* **1973**, *19*, 187.

(109) Macan, J.; Brnardić, I.; Ivanković, M.; Mencer, H. J. DSC Study of Cure Kinetics of DGEBA-Based Epoxy Resin with Poly(Oxypropylene) Diamine. *J. Therm. Anal. Calorim.* **2005**, *81* (2), 369–373. https://doi.org/10.1007/s10973-005-0794-3.

(110) Bernath, A.; Kärger, L.; Henning, F. Accurate Cure Modeling for Isothermal Processing of Fast Curing Epoxy Resins. *Polymers (Basel).* **2016**, *8* (11), 390. https://doi.org/10.3390/polym8110390.